UNIVERSITY OF READING

Department of Meteorology

Mathematical modelling of under-ice melt ponds and their impact on the thermohaline interaction between sea ice and the oceanic mixed layer

Naomi Smith

A thesis submitted for the degree of Doctor of Philosophy

2018

Declaration

I confirm that this is my own work and the use of all material from other sources has been properly and fully acknowledged.

Naomi E. Smith

Abstract

Melt water from the surface of Arctic sea ice fills hollows in the topography of the ice, forming pools of sea water that can cover up to 50% of the surface of the ice in the summer months. Since ice is a porous medium, water can percolate down from these melt ponds to the base of the sea ice, where it gathers in pools between the relatively cold, saline ocean water and the sea ice. These ponds are known as under-ice melt ponds. Freezing can occur at the interface between the under-ice melt pond and the oceanic mixed-layer, forming a sheet of ice called a false bottom. False bottoms insulate the true base of the sea ice from the ocean and their formation is a significant mechanism of Arctic sea ice summer growth. By changing the rate of basal ablation, under-ice melt ponds alter the fresh water and salt fluxes from the sea ice into the ocean.

Here, we evaluate the impact of under-ice melt ponds and false bottoms on the mass balance of the sea ice and its thermohaline interaction with the oceanic mixed layer below. We present a one-dimensional thermodynamic model of the evolution of under-ice melt ponds and false bottoms, with which we found that their development insulates the sea ice above them, increasing ice thickness. We couple this to a simplified ocean mixed layer model and found that the ablation of false bottoms rapidly transfers stored fresh water to the mixed layer. Our model indicates that under-ice melt ponds could lead to sea ice several tens of centimetres thicker if they form annually, and that false bottom ablation could lead to a sudden Arctic ocean mixed layer freshening and a resulting shallowing of the order of ten metres in areas of high under-ice melt pond fraction.

Acknowledgements

Contents

Chapter 1

Sea ice, melt ponds, and under-ice melt ponds

The Arctic is one of the most rapidly warming regions of the planet [Manabe and Wetherald, 1975; Hansen et al., 2010] and has become a symbol of climate change in the media. Due largely to ice-albedo and cloud feedback mechanisms, the surface temperatures in the Arctic are expected to rise two to three times faster than the mean global surface temperature [Taylor et al., 2013]. Transport of heat away from the equator through the atmosphere and ocean is also responsible for amplification of high latitude surface warming, for example through poleward-propogating Rossby waves [Lee, 2014], and polar amplification seen by forcing an aquaplanet model suggests that this enhanced warming occurs even without the presence of sea ice and thus the ice-albedo effect [Alexeev et al., 2005]. This rapid change of conditions in the Arctic, along with its impacts in turn on the rest of the planet's systems, makes it a region of importance to several areas of research within climate science.

In this thesis, we investigate under-ice melt ponds, which form beneath the Arctic sea ice after melt water from the surface drains through the porous ice matrix, macroscopic flaws in the ice, or lateral run-off [Notz et al., 2003]. This melt water is relatively warm and fresh compared with the ocean water, and so more buoyant, and therefore floats between the ice and the ocean. The growth of ice sheets, called false bottoms, has been observed at the interface between the under-ice melt pond and the ocean [Hanson, 1965]. Surface melt ponds have already proven important to the mass balance of the sea ice, and it has been hypothesised that under-ice melt ponds could similarly have an impact on the rate of basal ablation of the sea ice [Flocco et al., 2015]. It could, therefore, be desirable to include their effects in sea ice models.

In Section 1.1, we will start this chapter by motivating the improvement of sea ice models. We describe how the amount of sea ice is in rapid decline due to a warming

Arctic, that sea ice is a vital component of the climate system due to its role in the well-being of local communities and its influence on economic and political ventures, and that the loss of sea ice due to anthropogenic climate change will have secondary effects in various geophysical systems and processes.

In order to model under-ice melt ponds and assess their impact on the sea ice's mass balance and thermohaline interaction with the ocean below, we will need to simulate the sea ice as well, so we next discuss some notable advances in the modelling of sea ice, namely the classic thermodynamic sea ice model of Maykut and Untersteiner [1971], as well as the more recently developed mushy-layer sea ice model of Feltham et al. [2006], in Section 1.2.

We will then look at two of the most complete surface melt pond refreezing models in Section 1.3: those of Taylor and Feltham [2004] and Flocco et al. [2015]. The mechanisms of under-ice melt pond freezing are the same as those taking place within trapped surface ponds and these surface pond models have been used to quantify the effects that melt ponds have on the mass balance of sea ice. Later in the thesis, we show how we can adapt existing surface melt pond models to our purpose.

After this, we will summarise some observational studies of under-ice melt ponds, outline a laboratory experiment in which a false bottom was created and studied, and describe existing models of false bottom evolution in Section 1.4. We identify gaps in the knowledge that we have on these phenomena and motivate further investigation of under-ice melt ponds, which we will undertake in the chapters that follow.

Finally, having motivated the study of under-ice melt ponds and false bottoms and having introduced some models that have been used for similar purposes, we summarise this chapter in Section 1.5. We outline in more detail the aims of the thesis and briefly explain how we intend to use the existing sea ice and surface melt pond models described here to meet these aims.

1.1 Why is it important to accurately model sea ice?

1.1.1 The response of sea ice to climate change

Changes to the sea ice cover, frozen ocean water, are of particular interest to many as an indicator of climate change. When will the Arctic become 'ice free?' What effect will the melting of the sea ice have on the rest of the world? While ice loss serves as an iconic mark of a warming trend, the ice also plays an active role in the climate system. Although the melting of sea ice will not cause a significant change in global sea levels, unlike that of the Antarctic ice shelves and the Greenland ice sheet [Alley et al., 2005], it will significantly lower the region's albedo [Eicken et al., 2004; Holland et al., 2006]; freshen the surface waters of the Arctic Ocean, increasing stability and reducing deep water formation [Serreze et al., 2007]; and herald a great decline of vital habitat for local fauna [Tynan and DeMaster, 1997], including the iconic polar bear [Stirling and Parkinson, 2006]. For a few species, the loss of Arctic sea ice will improve conditions; for small phytoplankton, the freshening of water, upwelling of nutrient-rich bottom waters in areas freshly exposed to the wind, and the increased solar radiation reaching the ocean, makes for a more hospitable Arctic [Li et al., 2009].

Sea ice extent is the total area that contains at least some sea ice often as a fraction of the given area. The threshold for a given area to be said to contain sea ice is usually taken to be when at least 15% of the area is ice. There is a strong seasonal cycle in the Arctic sea ice extent, with areal coverage of around 14 to 16 million km^2 in the winter and around 7 million km^2 in the summer, and regularly lower in recent years [NSIDC]. The minimum extent values, which occur in September each year, are often used to compare between years. This inter-annual variablity sits on top a dramatic downward trend in the average extent, which decreased by roughly 3% per year in the period 1979 - 2005 according to an analysis of passive microwave satellite retrievals in Meier et al. [2007]. The extent has continued to decrease at an accelerating rate [Stroeve et al., 2012], as shown in Figure 1.1, taken from the National Snow and Ice Data Center (NSIDC) website [NSIDC].

Analysing ice volume records would yield the most complete picture of any trend in the amount of ice present in the Arctic. This requires an accurate, pan-Arctic collection of ice thickness measurements, which is impractical to obtain from ground measurements. Thicknesses gauges are difficult to use during the melt season due to the dangers of
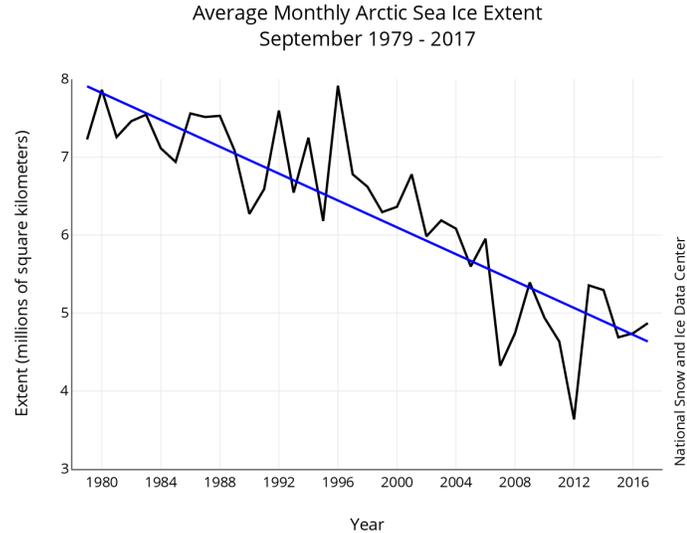
Figure 1.1: September average ice extent for 1979 to 2017, with line of best fit. A clear decline in extent is seen, with particularly low values in 2007 and 2012 and a negative trend in the line of best fit. Figure from the NSIDC website [NSIDC].

traversing the thin summer ice, and can alter processes affecting the mass balance of the ice due to the destructive nature of these measurements, for example by enhancing the drainage of fresh water.

Several satellite altimetry missions, such as Envisat, ICESat, and Cryosat 2, have recorded sea ice freeboard, which is the difference in height between the sea ice and sea water surfaces [Ricker et al., 2014]. This can be used to calculate the ice thickness, but the time series are relatively short and may contain inaccuracies due to a variety of features, such as cloud cover and local snow cover properties. Alternatively, model outputs, such as from PIOMAS, are often used [Schweiger et al., 2011]. PIOMAS is an ice-ocean model that uses assimilation of observed sea ice concentration to optimise volume estimates [Zhang and Rothrock, 2003]. PIOMAS thickness is typically taken by the community to be the best long term thickness product. The merit of this approach depends on accurate and relatively complete model physics, as well as reliable forcing data [Wang et al., 2016]. The available data suggest that the Arctic sea ice is thinning as well as decreasing in extent [Kwok and Rothrock, 2009; Laxon et al., 2013].

This is backed-up by measurements taken from underneath the ice in submarines. [Rothrock et al., 2008] used recently-declassified military submarine sonar data to inves-

tigate trends in the sea ice thickness over the period 1958-2000. Their work showed a strong decline in ice thickness, which was extended to 2008 in a subsequent paper that added ICESat data to the sonar time series Kwok and Rothrock [2009].

1.1.2 Human impact

Inuit communities rely heavily on the presence of sea ice for survival, particularly for food. Several Inuit peoples maintain records on the state of the sea ice, as well as any accompanying changes to species that they hunt. Berkes and Jolly [2002] describe changes that one such community in Sachs Harbor, Canada has made to to practices such as hunting, trading, and travel within the region in order to adapt to the local effects of Arctic climate change. The threats to two Inuit communities in Nunavut, Canada, primarily through changes to usual hunting strategies, are outlined by Ford et al. [2006].

Several countries and companies have interest in the opportunities provided by an 'ice-free' Arctic. The retreat of the sea ice could open shipping routes across the Arctic for significant periods of time each year, saving days to weeks off transit trips that would otherwise have to use the Suez and Panama canals [Melia et al., 2016]. Similarly, more open ocean could allow for the extraction of some of the region's large oil and gas reservoirs [Gautier et al., 2009].

1.1.3 Geophysical impact

Changes to the sea ice cover due to Arctic warming may cause further changes to the Earth's oceans and atmosphere, sometimes magnifying the effects of climate change. Since white sea ice is much lighter in colour than the dark blue ocean waters beneath it, sea ice reflects significantly more incoming solar radiation than the ocean; the higher the sea ice area, the higher the albedo of the Arctic region [Perovich et al., 2002]. As the Arctic warms and the average sea ice area reduces, less incoming solar radiation will be reflected out of the Earth's system and so further warming will take place. This is an important positive feedback mechanism [Dickinson et al., 1987]. As well as the change in areal cover, the changes in ice thickness, lead density, the duration of the snow cover, melt ponds, and ice distribution can all vary as the Arctic warms and can subsequently affect the region's albedo [Perovich et al., 2002].

The world's oceans are a large carbon sink, taking up almost 50% of anthropogenic carbon dioxide from the atmosphere [Sabine et al., 2004]. Sea ice physically blocks the exchange of carbon between the atmosphere and the ocean during winter, reducing uptake. Carbon dioxide is also rejected from sea ice during sea ice formation in a similar fashion to salt. [Rysgaard et al., 2011] However, the loss of sea ice will not necessarily lead to a large uptake of carbon; Cai et al. [2010] predict that low levels of biological activity drawing carbon down into the deeper ocean and reducing the partial pressure of carbon at the surface will mean that lower amounts of carbon will be absorbed in the absence of sea ice than previously expected. It also alters the exchange of pollutants between the two fluids [Pfirman et al., 1995] and reduces the amount of radiation reaching the ocean below, which is important to local biota [Arrigo et al., 2012].

Importantly, it also alters the momentum of the atmosphere and the ocean, and the exchange of momentum between them [Steele et al., 1989; Castellani et al., 2014]. The Arctic Ocean is historically a comparatively quiet ocean with strong stratification in the upper layers, but a reduction in the sea ice cover might be changing this. The movement and deformation of sea ice reduces the energy entering the ocean from winds at its surface [Rainville and Woodgate, 2009]. As the sea ice melts and a larger fraction of the ocean is exposed to the atmosphere, we therefore expect to see enhanced transfer of turbulent kinetic energy and a resulting deepening of the mixed layer. Topographical features such as leads, keels, ridges, and top and bottom surface roughness all affect the transfer of momentum to the ocean. Conversely, we are seeing a shift to a higher proportion of smoother first year ice as the Arctic warms, which is accompanied by a local decrease in the annual mean ocean surface stress [Martin et al., 2016]. The spin-up of the Beaufort gyre, for example, has been hypothesised to be due to an increase in momentum transfer from wind to the ocean due to a change in the sea ice cover [Giles et al., 2012].

As a result of these interactions between the sea ice, the atmosphere, and the ocean, it is important to model sea ice accurately in order to study climate change and its impacts. Global Climate Models (GCMs) tend to couple their primary atmosphere and ocean circulation models to a separately developed sea ice model. An example of such a model is CICE, produced by the Los Alamos National Laboratory [Hunke et al., 2010a]. As well as modelling key parameters of the sea ice, such as ice thickness and extent, sea ice

models include parameterisations of sub-grid scale processes that have been developed using independent modelling or observational studies. One such parameterisation has been made to account for the presence and evolution of surface melt ponds and trapped brine pockets [Hunke et al., 2010c].

Parameterisations often vary in complexity between models depending on the priorities of each model and practical concerns of computational efficiency. CCSM3, for example, and LIM3 use a parameterisation of melt ponds in which the surface albedo of the sea ice is reduced under conditions that would lead to melt pond formation, but there is no hydrological impact of ponds on the ice. CICE contains an estimate of melt pond area and volume for each thickness category of sea ice. The melt water not only affects the radiation scheme but also runs off into the ocean. More focussed models, which are designed to represent physics as fully as necessary to investigate the impact of certain processes rather than to simulate key properties of large areas of sea ice, typically include more complete descriptions of melt ponds [Hunke et al., 2010b]. [Ebert and Curry, 1993], as well as the models of [Taylor and Feltham, 2004] and [Flocco et al., 2015] discussed later in this chapter, make use of much more complex melt pond schemes, which include the melting and refreezing of melt ponds, melt water run off and retention in ponds, and the radiative effects of albedo changes.

1.2   Modelling sea ice

1.2.1   A thermodynamic model of sea ice

Maykut and Untersteiner [1971] developed one of the earliest, most widely-used thermodynamic models of sea ice. The model is one-dimensional, assuming that the sea ice is homogenous in the horizontal plane and extends infinitely, so that no laterally-acting processes affect it. The model consists of a snow layer (which may vanish) above a slab of sea ice. The base of the sea ice is allowed to grow or ablate, and the upper interface (either snow or ice) may melt. Snowfall is also able to accumulate at the top, thickening the snow layer.

Inside the snow layer, the standard heat equation is used to describe the evolution of its internal temperature over time. A more complex form of the heat equation is used to describe the evolution of temperature inside the sea ice, taking into account the presence

of brine pockets within the ice. Untersteiner [1961] proposed adaptions of the coefficients used in the heat equation to include an approximation of the brine's influence on density, specific heat capacity, and thermal conductivity. The specific heat capacity, for example, is derived from combining the specific heat capacity of pure ice with the additional heat required to melt a volume of ice and lower the brine's salinity. Beer's law is used to calculate the radiative heat flux reaching the specified depth.

At the snow-atmosphere (or ice-atmosphere) interface, the heat fluxes into and out of the boundary are balanced. This includes the incoming and outgoing longwave radiation, incoming shortwave, the latent and sensible heat fluxes, and the conductive heat flux through the snow (ice) layer. The shortwave heat flux also encompasses any reflected or absorbed shortwave radiation, and any melting at the surface is also taken into account. The conductive heat fluxes at either side of the snow-ice boundary are balanced, and a Stefan condition describes the growth or ablation of the base of the sea ice. The Stefan condition compares the conductive heat flux through the ice with any incoming heat flux from the ocean to find the remaining heat gain or deficit that will either melt or grow the ice.

Using the model, Maykut and Untersteiner [1971] were able to accurately estimate surface ablation and to predict ocean-ice heat fluxes. Semtner Jr [1976] successfully implemented a computationally efficient numerical method to adapt Maykut and Untersteiner [1971]'s model for use with a gridded climate model. This implementation has been extensively used in the sea ice component of climate models [Delworth et al., 2006; Johns et al., 1997; Randall et al., 2007].

1.2.2   Treating sea ice as a mushy layer

Maykut and Untersteiner [1971] assumed that the sea ice in their model is a block of low temperature ice, choosing values for relevant thermodynamic properties, such as thermal conductivity and heat capacity, that take into account the presence of brine pockets, accordingly. In reality it is comprised of both solid ice and its saline melt water, a combination commonly referred to as a 'mushy layer.' Worster [Worster, 1991, 1997] and Wettlaufer [Wettlaufer et al., 1997] laid out mathematical theory to describe convection within mushy layers and the accompanying transfer of heat and solutes. They note that sea ice bathed in brine constitutes a mushy layer.

The mushy layer formation for sea was then formalised by Feltham et al. [2006], thereby taking into account the brine portion of the sea ice. They use the mushy layer equations, frequently used to describe such two-phase media in materials science, to model the evolution of heat and salt in the sea ice. First of all, the local heat balance is given by the advection-diffusion equation

$$c_m \frac{\partial T}{\partial t} = \nabla \cdot (k_m \nabla T) + \mathcal{L} \frac{\partial \phi}{\partial t} - c_b \boldsymbol{u} \cdot \nabla T + A_R, \tag{1.1}$$

where c_m is the specific heat capacity, T is the temperature, t is the time, k_m is the thermal conductivity, $\mathcal{L}$ is the latent heat of fusion, ϕ is the solid fraction of the medium, c_b is the specific heat capacity of the brine phase, and A_R is the change in heat due to the absorption of radiation. $\boldsymbol{u}$ is the Darcy velocity of the liquid phase, i.e. the (vertical) flow of water per unit cross-sectional area of the sea ice. This says that the change in temperature over time is given by the change in heat content due to heat diffusion plus any change due to phase change minus any advection of heat out of the region, plus any heating due to absorption of radiation. The local salt balance is equivalently given by

$$(1 - \phi) \frac{\partial C}{\partial t} = \nabla \cdot (D_m \nabla C) + \frac{\rho_i}{\rho_b}(C - C_i) \frac{\partial \phi}{\partial t} - \boldsymbol{u} \cdot \nabla C, \tag{1.2}$$

where C is the brine salinity, D_m is the diffusion coefficient of salt, ρ_i is the density of the ice phase, ρ_b is the density of the brine phase, and C_i is the salinity of the solid ice phase. The temperature and salinity are linked by a linear approximation to the liquidus relation,

$$T = T_L(C) = T_L(0) - \Gamma C, \tag{1.3}$$

where Γ is a positive constant.

Feltham et al. [2006] show that the mushy layer equations are equivalent to the approach used in models such as Maykut and Untersteiner [1971] under the same standard, simplifying assumptions. They set the density of the ice and brine fractions to be equal, neglect any salt rejected from the ice during freezing, neglect brine flow, and replace the separate ice and brine salinities by a bulk salinity equal to a linear combination of the two. By substituting Equations 1.2 and 1.3 into Equation 1.1, they eliminate the solid

fraction ϕ and reduce the mushy layer equations to the nonlinear, mushy heat equation,

$$\left(c_m + \mathcal{L}\frac{T_L(C_i) - T_L(C_{\text{bulk}})}{(T_L(C_i) - T)^2} \right)\frac{\partial T}{\partial t} = \nabla \cdot (k_m \nabla T) - \left(c_b + \frac{\mathcal{L}}{T_L(C_i) - T} \right) \boldsymbol{u} \cdot \nabla T + A_R.$$

(1.4)

This description of how temperature and salinity evolve within sea ice has subsequently been incorporated into a number of sea ice models. CICE version 5.1 includes a mushy layer treatment of sea ice [Hunke et al., 2010c], which Turner and Hunke [2015] showed produced bulk salinities that closely match those obtained from ice core analysis, including their seasonal cycle affected by gravity drainage, snow-ice formation and the drainage of melt water. The mushy layer treatment of sea ice has also been used in several process models, such as Flocco et al. [2015]'s study of the impact of surface melt ponds on basal freezing.

1.3 Surface melt ponds

In the summer months, melt water from the surface layers collects in hollows, creating pools of fresh water. These melt ponds vary in size between tens of centimeters to hundreds of meters across and centimeters to meters deep [Fetterer and Untersteiner, 1998]. They can cover up to 50% of the surface area of the sea ice in the summer months, and attain a higher fraction still when considering certain regions [Rösel et al., 2012], see Figure 1.2.

Surface melt ponds significantly lower the amount of incoming solar radiation reflected by the region, with deeper ponds having a lower albedo [Rösel et al., 2012]. This contributes to the albedo feedback mechanism because more incoming solar radiation is absorbed as a result of a higher pond fraction, melting more water and increasing the depth and prevalence of surface melt ponds.

1.3.1 Modelling melt pond formation and evolution

The first notable use of a surface melt pond scheme in a process model, and furthermore one of the first to treat the pond and sea ice as separate thermodynamic phases, was that of Ebert and Curry [1993] in their investigation of sea ice-atmosphere interactions. They allowed a portion of melt water and precipitation to accrue on the surface in melt ponds

Figure 1.2: Scientists on sea ice bearing surface melt ponds on 12th July 2011 during the ICESCAPE mission. Photo taken by Kathryn Hansen [NASA].

with variable depth and areal fraction, while the rest of the water runs off the ice into the ocean, for the surface pond to refreeze at the end of the melt season, and for the presence of melt ponds to lower the albedo of the sea ice surface. The refreezing of the ponds acted as a source of latent heat in the ice. This was by far the most advanced treatment of surface melt ponds at the time, with models such as that of Kantha and Mellor [1989] allowing a layer of melt water on the surface but not varying the ice albedo accordingly. However, a number of simplifying assumptions were made, such as the prescription of a refreezing start date and refreezing rate based on observations rather than calculation.

The first melt pond model to include a mushy-layer treatment of sea ice was a one-dimensional model developed by Taylor and Feltham [2004]. Their model is able to capture the formation of melt ponds on sea ice, the formation of a lid of ice on top of the pond, and a snow layer above either the sea ice or the pond's lid. The mushy layer equations are used to describe heat transport within the sea ice layer, while the heat transport in the pond is given by either a turbulent or non-turbulent version of the heat equation depending on the pond's Rayleigh number. The diffusion equation describes the temperature evolution within the snow layer.

An energy balance equivalent to that used by Maykut and Untersteiner [1971] acts at the upper interface with the atmosphere but, instead of using Beer's law, a two-stream radiation model is used to describe the attenuation of radiation through the domain. This

accounts for the presence of multiple layers of different optical properties and allows the albedo to be determined at each time step. At the internal boundaries and at the base of the sea ice, Stefan conditions give the change in position by calculating the difference between conductive heat fluxes either side or, at the lowest boundary, the heat flux into the ice from the ocean. When a melt pond is present, they assume a constant rate of drainage of melt water through the ice and assume the pond has a constant salinity.

Using this model, they were able to reproduce the life-cycle of a surface melt pond over the course of a year, and the surface albedo along with it. Their work using the model suggested that melt ponds have a larger effect on the mass balance of the sea ice than had been previously anticipated.

1.3.2   A more complex treatment of melt pond salinity

Flocco et al. [2015] went beyond previous studies of the evolution of surface melt ponds and their impact on the albedo of the region to investigate their effect on the basal freezing of sea ice in winter. It had previously been noted that a lid of ice forms upon the surface of these ponds at the start of their refreezing process. While the refreezing of surface melt ponds had been modelled before by Taylor and Feltham [2004], Flocco et al. [2015]'s study was the first study to take a detailed look at the role that salinity plays in the process, and their model is arguably the most physically complete model of the refreezing of melt ponds to date. Models including the areal coverage of the ponds had been previously developed, such as those of Skyllingstad et al. [2009] and Lüthje et al. [2006], but these primarily served to look at the growth of ponds in the summer, not autumnal refreezing.

By using a technique developed by Bailey et al. [2010], Flocco et al. [2015] took into account the salt rejected by ice as it forms on the pond's salinity. The rejected salt increases the salinity of the remaining water, subsequently lowering the liquidus temperature of the water and reducing the rate of freezing. While the interior of the pond is assumed to be turbulent, there is constant injection of salt at the pond-ice interfaces during refreezing, so[Flocco et al., 2015] also included boundary layers of thickness

$$L = \frac{D}{\frac{\mathrm{d}h}{\mathrm{d}t}}$$

in the salinity field at the edges of the pond where the water meets the ice. These solutal boundary layers are less than millimetres thick, occurring due to the low molecular diffusivity of salt.

Flocco et al. [2015] used the same two-stream radiation scheme of Taylor and Feltham [2004] for the the attenuation of radiation through the pond, the sea ice, and any lid of ice that forms on top of the pond. Since the problem involves multiple strata of different transmissive properties, using Beer's Law for a semi-infinite layer would incur a significant error from scattering at the various interfaces.

ERA-Interim data was used to force the model at the surface, namely through shortwave and longwave radiation fluxes, and 2-m air temperature. Flocco et al. [2015] prescribed a constant heat flux from the ocean into the ice, a constant wind speed, and a constant atmospheric pressure, and they assumed that there was no precipitation. These assumptions were justified by the relatively short periods in time that the simulations are run for, although the heat flux from the ocean could have a large effect on the rate of basal growth, which is studied using the model.

This relatively physics-rich model of melt pond refreezing was used to calculate the length of time that the ponds persisted for and, importantly, how long it subsequently took for the temperature profile within the resulting block of sea ice to return to a balance, via the diffusion and transport of heat, that allows freezing. The pond is warmer than the sea ice and acts as a source of latent heat during refreezing. The resulting temperature gradient within the ice means that heat is conducted towards the base of the sea ice. In order for basal freezing to occur, the gradient of the temperature profile at the base needs to reverse so that heat is conducted away, which requires some time after the refreezing of the pond. Typical profile shapes are illustrated in Figure 1.3.

A reference case simulation was carried out by Flocco et al. [2015] at the location 80N, 210E, followed by a number of sensitivity studies. The duration of each simulation was 60 days. In the reference run, they saw that the pond was frozen after 33 days, but that it took another 18 days for the temperature gradient within the ice to straighten out and become close to linear, allowing growth at the base of the sea ice. There was 0.22 m more ice growth at the base of a slab of sea ice with no surface melt pond compared to the reference case with a pond of initial depth 0.4 m due to the delayed onset of ice growth while the temperature profile adjusted.
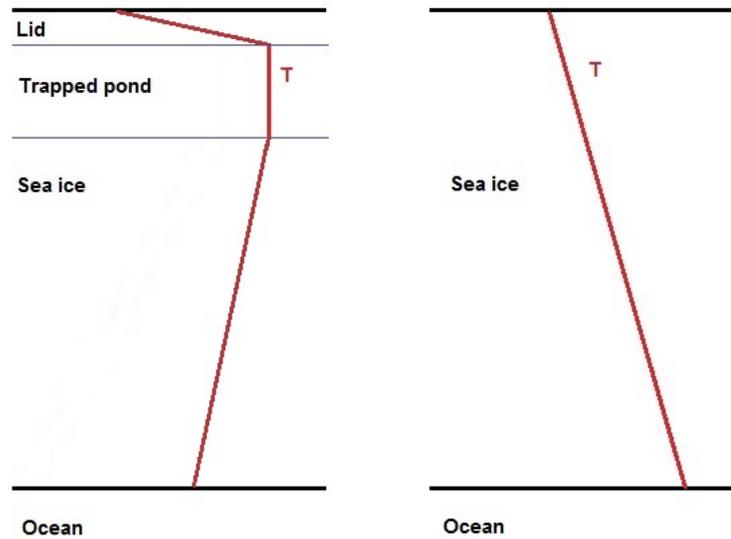
Figure 1.3: A schematic showing typical temperature profile shapes (left) during the refreezing of a trapped melt pond, where no basal growth occurs due to the positive gradient at the base, and (right) after the pond has refrozen, when the temperature profile has been corrected through diffusion and basal growth is able to occur.

Flocco et al. [2015] notes that the rate of freezing of the pond interfaces slows over time as salt is rejected into the pond from the growing ice, raising the water's salinity and decreasing its freezing point. The base of the pond ablates due to dissolution of ice into the high-salinity water, but this is a relatively small effect compared to the rate of freezing for most of the simulation.

In their reference simulation, the permeability of the ice below the pond decreases by a factor of 100 during the refreezing period, allowing very little drainage from the pond into the ocean. This might indicate that, in order for under-ice melt ponds to form beneath surface melt ponds, either melt water drainage must occur primarily before the refreezing period of the surface pond or the under-ice melt pond must form beneath macroscopic flaws in the sea ice.

Towards the end of the simulation, the pond becomes too saline from brine rejection during ice growth to allow more vertical freezing. Rather than say that the pond is frozen when the remaining depth of pond water is close to zero, they chose to use a criterion by which the pond is considered to be frozen when the solutal boundary layer was of

greater salinity than the maximum brine salinity of the ice above it, since no further refreezing will take place in the model once this occurs.

Flocco et al. [2015] carry out a comparison between using a uniform salinity in the trapped pond and using their solutal boundary layer model. They find that including the solutal boundary layers decreases the freezing rate and so increases the amount of time that pond persists for. The salinity in the interior of the pond, away from the boundaries, is also higher in the solutal boundary layer model simulations.

Sensitivity studies show the impact of forcings, which were varied by changing the location; the initial sea ice thickness; the initial pond depth; ocean salinity, which affects the ocean temperature at the interface via the liquidus relation; and the oceanic heat flux on the model outputs. For colder locations, the pond takes less time to freeze and more basal ice growth is seen. Ponds typically have a fresher interior, too. Thicker sea ice sees less basal ice growth due to the reduced heat transfer through the thick slab of ice, and the pond, correspondingly, requires more time to freeze. A thick pond of 60 cm was unable to freeze before the simulation ended, and so no basal growth was seen. In comparison, a thin 20 cm pond froze after just 7 days and 7 cm of basal ice growth subsequently took place. Increasing the ocean salinity, and thus decreasing the ice temperature at the interface according to the liquidus curve, does not affect the length of time that the pond persists for but does increase the amount of basal ice growth seen afterward. A small increase in freezing time was seen when increasing the ocean heat flux, and the onset of basal ice growth was delayed.

This study shows that surface melt ponds are important to the mass balance of the Arctic sea ice, reducing basal ice growth by 22 cm under standard assumptions. It also reinforces the importance of an accurate treatment of salinity in refreezing models, and emphasises the impact that a number of different parameters can have on the refreezing process and subsequent ice growth. With respect to sea ice modelling, the model developed by Flocco et al. [2015] is the most advanced model of melt pond refreezing, following on from the model of Taylor and Feltham [2004].

1.4   Under-ice melt ponds

The melt water present on the Arctic sea ice in surface melt ponds does not just evaporate or refreeze. Fractions of the melt water have been observed to drain to the base of the sea ice during several field experiments, such as that of Hanson [1965] and the SHEBA mass-balance experiment [Perovich et al., 2003]. This can take place via various mechanisms [Eicken et al., 2002]. First of all, melt water can run off an ice floe laterally and be swept underneath the ice by ocean currents. Secondly, macroscopic flaws in the ice, such as seal holes and cracks beneath surface melt ponds can allow the melt water to trickle down through the ice. Finally, since the ice is porous and can contain macroscopic cracks, water on the surface that is above hydrostatic equilibrium is often able to drain down through the ice. Polashenski et al. [2017] note that this can lead to a strong reduction in permeability through the ice, so may not be a prominent avenue of melt water drainage later on in the pond season. This water is relatively warm and fresh compared to the ocean below, and so more buoyant. When it reaches the base of the ice, it is therefore able to float between the ice and the ocean provided there are reasonably calm conditions.

Since surface melt ponds have a lower albedo allowing more incoming radiation to penetrate through the ice, there is often more melting at the base of the sea ice beneath surface melt ponds. This leads to 'mirror image' hollows in the base of the sea ice [Taylor and Feltham, 2004]. These hollows beneath surface melt ponds could potentially shelter drained melt water bodies from ocean currents and thus prevent mixing to form pools of fresh water beneath the ice, known as under-ice melt ponds.

Observations of under-ice melt ponds have been made, often beneath surface melt ponds, during ice thickness measurements, from ice cores, and from explorations by divers in the water [Hanson, 1965; Eicken, 1994; Martin and Kauffman, 1974]. Observations frequently note the formation of an additional ice sheet between the pond and the ocean, known as a false bottom.

Here, I will summarise some notable observations that have been made of under-ice melt ponds, what we have learnt from them, and modelling attempts to date.

1.4.1   Early field observations of under-ice melt ponds

Hanson [1965] provided some of the first detailed sets of observations of under-ice melt

ponds including thickness. Hanson [1965] analysed data taken at the U.S.-owned drift station 'Charlie,' including evaporation, precipitation, melting/ablation, freezing, and condensation, to compute the mass balance of the Arctic pack ice there. The station was operational for 19 months between April 1959 and January 1960, and drifted with the pack ice between latitudes of 76 to 78.2°N and longitudes of 159.5 to 174.4°W. The data from 'Charlie' was compared with that of a previous drift station, 'Alpha,' and a later drift station 'ARLIS II.'

Measurements were taken of cross-sections of the ice at several different locations. To survey changes to the mass balance at the base of the ice, holes were drilled vertically downwards from the surface to the base to allow thickness measurements to be made. Three such gauges were placed through under-ice melt ponds and false bottoms, allowing the thicknesses of these layers to also be recorded. In one instance, multiple false bottoms were present, suggesting that there were two drainage periods before the measurements were taken.

The thicknesses plotted in Figure 2 of Hanson [1965] indicate that one under-ice melt pond was initially around 81 cm deep. The under-ice melt pond closest to the sea ice in the multiple-pond formation was about 28 cm deep, and the one beneath it was of roughly the same thickness.

At the first of the two sites, the false bottom was observed to migrate upwards, freezing through the under-ice melt pond, while at the location containing stacked ponds both false bottoms migrated upwards but thinned and eventually were ablated from below over the course of around a month. It could be important to note that a surface melt pond was present at the stacked-pond location, which would mean more incoming solar radiation absorbed at this site and so higher basal ablation rates. One under-ice melt pond below ice covered with a surface melt pond persisted for multiple months, from late July to at least mid September.

The area fraction of the base of the sea ice that these under-ice melt ponds cover is pivotal in determining the effect of under-ice melt ponds on the mass balance of the sea ice of the region as a whole. Hanson noted that around half of the floe was underlain by these pools. However, as Notz et al. [2003] later suggested, such a high fraction could have been due to enhanced drainage from human activity. Weight on the ice could have created more cracks or propagated existing ones, and enhancing the heat at the surface

of the ice could raise the internal temperature and thus the permeability. Boring holes through which to take measurements would also allow for extra drainage to the base of the sea ice.

1.4.1.1   Under-ice melt ponds in ice core analysis

Almost thirty years later, Eicken [1994] took an ice core from a patch of ice under-lain by an under-ice melt pond. They were taking ice cores for the ARCTIC 91 campaign at sites along a transect of the Arctic from Svalbard, to the North Pole, then to Fram Strait from late August to September of 1991. A core taken from multi-year ice located at 85°58′N, 0°10′E turned out to contain an under-ice melt pond.

Eicken [1994] noticed that the false bottom's crystalline structure differed drastically from that of the ice above the pond. Whereas the parent sea ice directly above the pond was columnar in structure (with a layer of granular ice towards the surface), the ice above the false bottom was comprised of a mixture of columnar and granular ice. This structural difference in the types of ice was then used by Eicken [1994] to identify that 8 out of their 52 cores (taken at 46 different sites) contained false bottom ice, and he concluded that a significant proportion of the sea ice is underlain by fresh water ponds.

Eicken [1994] also found important differences in the salinity and δ^{18}O profiles between those cores containing under-ice melt pond and those without. While sea ice is typically more saline towards the bottom, sea ice above an under-ice melt pond is instead fairly fresh towards the pond-interface. There was, similarly, a decrease in the δ^{18}O concentration in the sea ice directly above the under-ice melt pond.

The δ^{18}O values within the cores containing under-ice melt ponds were relatively low, suggesting that there was a large contribution of meteoric water to the fresh water pond. Given that other observations of authors such as Hanson [1965] and Untersteiner [1961] are clear that the fresh water comes from surface melt, this could indicate that snowmelt could be an important source of the under-ice melt pond water. Eicken [1994] posits that the linear salinity and δ^{18}O profiles in the ice above the under-ice melt pond pond section are inconsistent with those typically found following ice growth, suggesting an interaction occurred between the fresh water layer and the sea ice's brine beyond the original drainage. They suggest that molecular and perhaps turbulent diffusion between the two layers could be responsible for this alteration of the salinity and δ^{18}O

profiles.

Eicken [1994] found that the fresh water of the under-ice melt pond freezes in winter to produce false bottom ice of very low permeability due to the low brine volume fraction. This means that pollutants entering the under-ice melt pond via the flushing of meteoric water will most likely be trapped within the system until the false bottom ice melts. This might result in the large outflux of pollutants in a certain region of ice with high under-ice melt pond fraction is advected towards the same place, such as the Fram Strait, where warmer or saltier conditions cause the false bottom ice to ablate.

Freezing of the fresh water layer into this low salinity, low brine volume fraction ice leads to a stronger ice cover at the base than would be typical with no under-ice melt pond. Optical transmissivity would also be affected by this, altering the amount of light reaching the base of the ice. This is of importance for the biota that lives in the lower centimeters of the ice and the upper layer of the ocean, greatly affecting rates of photosynthesis. Eicken [1994] notes that the replacement of nutrient-rich water with low-nutrient meteoric water could also increase the osmotic pressure exerted on the biota of this region.

In summary, Eicken [1994] provided valuable information on the salinity of the under-ice melt ponds and their effects on key properties of the ice above them, particularly regarding permeability, porosity, and strength. They also identified typical ice core strata for sites containing under-ice melt ponds, allowing the possibility of future cores to be correctly categorised. Given enough measurements, this could be used to estimate the under-ice melt pond fraction. Eicken [1994] concluded that at least 5% of the sea ice is underlain by these ponds, assuming a summer surface melt pond fraction of around 25% and that 25% of these surface ponds are underlain by under-ice melt ponds.

1.4.1.2   Remote sensing of the base of sea ice

Data collected in the field by Eicken [1994] and Hanson [1965] has been hugely helpful in determining the properties of under-ice melt ponds and their typical life cycle. However, to understand the processes involved in their formation and evolution, as well as to determine their impact on their surroundings, we need more comprehensive data or accurate models of their behaviour. Given the difficulty of taking measurements from them in person from the top of fragile summer ice, remote sensing is probably necessary

to get a large data set on under-ice melt ponds.

After previously successfully using upwards looking sonar to obtain linear profiles of the base of the ice, Wadhams [1988] used sidescan sonar to develop a three-dimensional view of the topography of the base from a submarine below. From these images, they were able to distinguish between first year and multiyear ice, the prior being smooth with the exception of cracks and the latter being rougher, littered with 'blisters and bulges.'

Importantly, this allowed them to validate airborne passive microwave data, but the observation of characteristic bulges beneath the ice lead Wadhams [1988] to question whether they could be refrozen under-ice melt ponds. They saw distinct bulges of roughly circular shape on the base of the sea ice, observing diameters of between 14 and 80 m on one multi-year floe and 28 to 63 m on another. He suggested that these could be left over from the freezing of under-ice melt ponds. However, Eicken [1994] notes that the idea was never confirmed due to a lack of any further field observations. Were the theory to be proved correct, then a regional under-ice melt pond fraction could be calculated.

Current estimates of the under-ice melt pond area fraction vary between 5 and 40% [Eicken, 1994; Notz et al., 2003], with perhaps half or more of the ice underlain by these ponds in areas of enhanced drainage due to human activity or very high surface melt pond fraction, such as the marginal ice zone [Hanson, 1965].

1.4.2 Modelling under-ice melt ponds

1.4.2.1 A cold room experiment

In order to model the evolution of under-ice melt ponds, we need to understand the physics driving the formation of false bottoms, and then the growth or ablation at the three ice-water interfaces. Many of the hypothesised mechanisms and time scales of false bottom formation and evolution come from research carried out by Martin and Kauffman [1974]. They designed and executed a cold room experiment aimed to simulate the phenomena observed beneath the Ward Hunt ice shelf off the coast of Canada and the pack ice above the Arctic Ocean during the summer.

They filled the upper half of an insulated Plexiglas tank with a mixture of fresh wa-

ter slightly above the freezing temperature and granular ice and the lower half with colder salt water, representing an under-ice melt pond above Arctic ocean water. The experimental under-ice melt pond layer had an initial depth of 40 cm and the salt water beneath was maintained at its freezing temperature.

A thermocouple array was used to measure the temperature throughout the tank, and water samples were taken through sealed holes in the tank to measure the salinity. The tank was illuminated and photographs were taken to record any ice growth, with straight tape on the back of the tank used to illustrate in photographs the change in refractive index with the water's salinity.

Martin and Kauffman [1974] observed the nucleation of ice crystals on the granular ice at the top of the tank two to three days after the start of the experiment and their subsequent growth roughly vertically downwards through the fresh water layer. They note that there was convective instability in the fresh water layer and supercooling at its interface with the salt water.

Ice crystals grew on the walls of the tank and also the thermocouple mount, and then the vertical growth slowed and lateral growth occurred at the interface with the salt water. The lateral projections eventually met and froze together to form a false bottom type ice sheet on around day 14 of the experiment. They then saw the false bottom thicken and migrate upwards, with its base becoming "'smooth and glassy.'"

From these observations, Martin and Kauffman [1974] distilled three phases in the formation of false bottoms:

1. convection and vertical growth of crystals through the fresh water pond;

2. lateral growth at the interface with the ocean;

3. and finally, migration upwards and thickening.

Martin and Kauffman [1974] also proposed mathematical models for each stage. When modelling the convection characteristic of the initial stage, they noted that double diffusion occurred between the fresh and salt waters, transferring heat out of the under-ice melt pond 5 to 10 times more efficiently than through standard diffusion.

Convection due to double diffusion occurs when two components, with different gradients and coefficients of diffusion, diffuse within a fluid. In oceanography, it can

occur with salt and heat as the two components, the prior of which diffuses around 100 times faster than the latter in water. This is what drives the creation of 'salt fingers' in the ocean, for example: when warm, salty water lies above cold, fresh water, perturbations at the interface lead to sections of warm, salty water descending into the lower portion of water. Salt diffuses into the surrounding cooler, fresher water more slowly than heat, creating fingers of cool, salty water that further invade the lower portion of the water due to their increased density. [Schmitt, 1994] In the case of under-ice melt ponds, warm, fresh water sits above cooler, saltier water, and heat diffuses out of the under-ice melt pond and into the ocean below. The resulting cooler, fresher water rises up and drives convection within the pond and nucleation of ice crystals on the base of the sea ice.

For the lateral growth, Martin and Kauffman [1974] developed a model of crystal thickness as it grows outwards at the interface, arriving at a nonlinear diffusion equation involving crystal width and dimensionless salinity. They linearised this equation and used a similarity solution to solve for crystal width analytically, roughly reproducing the shape of a crystal found in their tank. However, using numerical methods one could approximate a solution to the full nonlinear problem, and we do this in Chapter 2.

Martin and Kauffman [1974]'s model of false bottom position and thickness proved useful for a description of the processes at work in their experiment, however it is not a complete and accurate description of the evolution of a false bottom native to the Arctic. They assumed that the temperature is linear throughout the false bottom ice and that the false bottom contains only ice, while in reality it is a two-phase medium containing both ice and brine [Taylor and Feltham, 2004], and can have a nonlinear temperature profile if the boundary temperatures or ice thickness change more rapidly than the profile can adjust through diffusion and advection.

Martin and Kauffman [1974] neglected any radiative forcing and they also neglected any salinity effects within the under-ice melt pond. In their experiment, the 'pond' water may be close to completely fresh, but including a brine fraction within the ice and taking into account salt rejection from the ice matrix during freezing can raise the pond's salinity. As seen in Flocco et al. [2015], salinity can also be much higher at the boundaries due to this rejection of salt during freezing and the low rate of diffusion compared to temperature. This can have a significant impact on freezing and ablation rates. It is also assumed that the domain is infinite above the pond, and so there is no upper limit on

how far the false bottom can grow at the upper interface.

Martin and Kauffman [1974] were unable to carry out any meaningful additional analysis with the model due to lack of measurements of the ocean properties beneath the sea ice at the time. This could be rectified today using observations of the Arctic waters or a mixed-layer model for the far field temperature and salinity.

1.4.2.2   A model of false bottom evolution

Notz et al. [2003] made one of the few notable attempts at modelling false bottom evolution since Martin and Kauffman [1974], some thirty years later. They propose two versions of a thermodynamic model of the false bottom boundary positions' growth and ablation over time, according to whether the ocean beneath the false bottom is turbulent or not.

For a simple, non-turbulent version of their model, they were able to provide an analytical solution using similarity solutions, which indicates the importance of salt transport on false bottom thickness. This model is essentially equivalent to that proposed by Martin and Kauffman [1974]. As such, they compared the non-turbulent case with the experimental data of Martin and Kauffman [1974], finding that the model's predicted boundary positions closely resemble those observed in the cold tank, especially later on in the experiment when the ice sheet was more uniform in thickness.

Notz et al. [2003] then adapted this model to include turbulent, rather than diffusive, heat and salt fluxes, more typical to false bottoms in the field. Their analytical solution no longer applied and they investigated it numerically. In this turbulent case, they compared basal boundary positions with data collected during the AIDJEX field experiment. They found that, again, their model is in close agreement with the data, particularly so when they choose a ratio of exchange coefficients typical for rough surfaces. This runs slightly contrary to the observations of false bottoms made by the diver Campbell and recounted in the introduction of Martin and Kauffman [1974], which suggest that false bottoms are smooth on the lower surface and rougher on the upper surface. However, the estimate of [Notz et al., 2003] that uses a ratio of exchange coefficients of heat and salt for a smooth surface also provides a reasonable match to the experimental data relative to the bare ice's basal ablation rate.

Notz et al. [2003] saw that the false bottom ablated from below much more quickly

than the exposed sea ice, and was accompanied by a heat flux of around 8 to 15 W m^{-2} from the ice into the ocean water. The phase change was driven by dissolution rather than melting.

Finally, using a friction velocity derived from the SHEBA experiment data, Notz et al. [2003] used their model to gain some insight into the effects of a storm on the sea ice in 1998. In a period of 20 days starting in mid-July, the friction velocity starts out fairly low then significantly increases in the latter half of the period when a storm came through the camp. In the quiet period, the false bottom grew in thickness at a decreasing rate, before rapidly ablating during the stormy period. Their model did not, however, predict that the false bottom completely ablated. The heat flux between the false bottom ice and the ocean was also observed to reverse in this period; during the storm, the heat flux is directed from the ocean into the ice, rather than vice versa as seen in the quiet period. Notz et al. [2003] suggest that enhanced salt flux during the storm could have allowed the ocean heat to help ablate the ice, and conclude that the mechanical break up of false bottoms could have been enhanced by the sudden basal ablation caused by the storm, releasing the under-ice melt pond water into the ocean.

The paper suggests that further understanding of under-ice melt ponds is desirable, since the thickening of false bottoms in their model directed a significant heat flux into the ocean and their ablation during quiet periods and break-up during storms inputs a steady and a rapid fresh water flux into the ocean respectively. Their presence could insulate the ice from the ocean, reducing basal ablation and leading to thicker sea ice, as well as affecting salt and fresh water fluxes into the ocean, potentially changing mixed layer depth, salinity and temperature.

1.4.2.3   A mushy layer model of false bottoms

Later, in 2008, Alexandrov and Nizovtseva [2008] published a similar model of false bottom evolution to Notz et al. [2003], which they solved analytically and compared with field data from the AIDJEX and SHEBA experiments. They choose the same time period as Notz et al. [2003] for both experiments, also analysing false bottom evolution during the same storm.

Alexandrov and Nizovtseva [2008] assume that a thin false bottom ice sheet has already formed, citing Notz et al. [2003]'s observation that they seem to form much more

rapidly in the field than in Martin and Kauffman [1974]'s experiment. They assume that the temperature within the false bottom ice has a linear profile and is at equilibrium, with a linear salinity profile with depth as well. They use Stefan conditions at the water-ice boundaries, with a heat flux upwards from the ocean calculated using far-field properties and neglected from the pond, and diffusion equal to the rate of salt expulsion from the freezing ice. They solved their model analytically to find expressions for the upper and lower false bottom boundary positions and then compared their model's outputs to data obtained during field experiments.

The model of Alexandrov and Nizovtseva [2008] shows the false bottom thickening over the first 8 days, then ablating from below and thinning as friction velocity increased during the storm. The Stanton numbers predicted by their model using AIDJEX and SHEBA data over time matches that used by Notz et al. [2003] well.

The model's outputs indicate a heat flux of the order of $10 \, \mathrm{Wm}^{-2}$ into the ocean from the false bottom as it freezes, thickening upwards from through the under-ice melt pond. This heat flux also falls well within the range of Notz et al. [2003]'s model prediction of 8 to $15 \, \mathrm{Wm}^{-2}$.

Alexandrov and Nizovtseva [2008]'s study is very similar to that of Notz et al. [2003], as they used a very similar model and identical data to force the model and compare their results to. The results of their study match Notz et al. [2003] closely, lending further support to the conclusion that the false bottom insulates the sea ice from the ocean.

It is worth noting that Alexandrov and Nizovtseva [2008]'s model, that of Notz et al. [2003], and that of Martin and Kauffman [1974] purely simulate the boundary positions of the false bottom with time and the fluxes into the surrounding waters arising from their growth. In this sense, they are essentially assuming that the water fields, namely the under-ice melt pond and the ocean, extend to infinity either side of the false bottom. They do not calculate properties of the sea ice above the under-ice melt pond, such as thickness or temperature, with time, and so do not calculate a new under-ice melt pond depth. Their false bottom is therefore allowed to evolve indefinitely, as long as it does not completely ablate away; it cannot freeze all the way through the under-ice melt pond. These authors also do not take into account the salinity of the under-ice melt pond, assuming that it is completely fresh. While the ponds do have a very low salinity of a few psu, as the false bottom migrates upwards, freezing through the pond, and the

base of the sea ice grows down into it, salt will be rejected from the ice during the phase change into an increasingly smaller pond, raising its salinity significantly as occurred in the, initially very fresh, trapped melt pond of Flocco et al. [2015].

1.5   Summary and thesis outline

In this chapter, we have seen that sea ice is a critical component of Earth's climate, and as such it is important to model it accurately in GCMs. The state of the sea ice is also of high relevance to local populations, fauna, and several industries of high economic impact, and so modelling for short-term forecasts is also important.

Sub-grid scale processes can affect the sea ice in significant ways. These processes are often parameterised for use in the sea ice components of climate models. One such example is the formation and evolution of surface melt ponds, which have been shown to have a strong impact on both the sea ice's albedo and basal growth.

Observations have shown that surface melt water can also drain through the ice and pool in hollows in the topography of the base of the sea ice, creating under-ice melt ponds. Sheets of ice called false bottoms can form between the fresh water-ocean interface, completely isolating the under-ice melt ponds from the ocean below. These occurences have been observed in the field through ice thickness measurements and ice cores [Hanson, 1965; Eicken, 1994], and have been replicated in a laboratory experiment [Martin and Kauffman, 1974]. They could be important to the mass balance of the sea ice, as well as potentially having some smaller-scale impacts, such as affecting the transport of pollutants in the Arctic.

We see that relatively little work has been done on under-ice melt ponds and their impacts on their surroundings. Several one-dimensional false bottom models have been developed [Martin and Kauffman, 1974; Notz et al., 2003; Alexandrov and Nizovtseva, 2008], but they all assume a semi-infinite domain above them, i.e. they do not allow for the under-ice melt pond to completely freeze, and they all neglect salinity within the under-ice melt pond, which has been shown by Flocco et al. [2015] to be important to surface melt pond refreezing. The studies have investigated the evolution of false bottoms and key processes involved, as well as looked at the heat flux between the ice and the ocean during this time. However, there is no comprehensive study on the effect

of under-ice melt ponds on the mass balance of the ice above them, and similarly no study has gone beyond looking at the magnitude and direction of the ice-ocean heat flux to investigate the mutual interaction of under-ice melt ponds and the oceanic mixed layer.

There has also been no notable attempt to link up the stages of under-ice melt pond development. Martin and Kauffman [1974] proposed mathematical models for each stage of under-ice melt pond evolution, and Notz et al. [2003] and Alexandrov and Nizovtseva [2008] developed models of the boundary positions of pre-formed false bottoms over time, but there is no comprehensive model linking all stages of the life cycle of these ponds and ice sheets.

Sea ice modelling has been shown to be vital to our understanding of the changing global climate and predictions of future conditions, as well as to those with vested interests in the state of the Arctic. It is therefore desirable to properly understand the effect of under-ice melt ponds on the mass balance of the sea ice and key properties of the oceanic mixed layer, so that we can either improve the sea ice components of climate models by including these effects or continue to neglect them with proper justification. As such, we aim to

1. investigate the impact of under-ice melt ponds and false bottoms on the mass balance of the sea ice;

2. investigate the impact of under-ice melt ponds and false bottoms on the thermohaline interaction between the sea ice and the mixed layer; and

3. assess whether these phenomena warrant including in sea ice models, such as the sea ice components of climate models.

In the second chapter of this thesis, we solve the model of Martin and Kauffman [1974] for the lateral growth of crystals into a false bottom ice sheet numerically and compare the solution with their own analytical solutions. This model is incorporated into a multi-year model later on in the thesis.

We will then describe the model of the evolution of an established under-ice melt pond and false bottom sitting beneath a slab of sea ice in the third chapter. We look at two case studies of typical under-ice melt pond evolution and then validate the model against Hanson [1965]'s field observations. We present the results of a reference simulation run

with this model and the conclusions that we draw regarding the effect of under-ice melt ponds on the mass-balance of the sea ice above them, as well as the studies used to test the model's sensitivity to various key parameters.

Heat transfer from the ocean to the false bottom and vice versa during the thickening of the false bottom during calm periods affects both false bottom and ocean mixed layer properties. The presence of the insulating under-ice melt pond and false bottom also affects the rate of basal ablation of the ice above, and so any salt fluxes into the mixed layer, as well as delaying or reducing any fresh water flux that would otherwise go straight into the mixed layer. As such, it is likely important to model the interaction between the ice and the ocean when investigating this phenomenon.

In the fourth chapter, we present a coupling of the under-ice melt pond model to a model of the oceanic mixed layer beneath the false bottom adapted from the work of Petty et al. [2013]. From this, we are able to analyse the impact that the presence of under-ice melt ponds has on key properties of the mixed layer, i.e. depth, temperature, and salinity. We also link all three chapter's modelling efforts together to produce a comprehensive, multi-year model in which under-ice melt ponds form from drainage through the ice, false bottoms form and subsequently evolve, with impacts on the ice mass balance and the oceanic mixed layer properties.

In our final chapter, we summarise the findings of the thesis and their importance to sea ice modelling, along with a discussion of the limitations of our models, and required measurements for future work.

Chapter 2

False bottom formation

2.1 Introduction

Most of the field observations of under-ice melt ponds in the field have seen false bottoms already formed [Hanson, 1965; Eicken, 1994; Martin and Kauffman, 1974]. This could simply be because the ponds have generally been discovered through ice thickness measurements, which would not detect an under-ice melt pond exposed to the ocean, rather than salinity measurements beneath the ice. In order to develop a deeper understanding of an under-ice melt pond's evolution and its impact on the sea ice and ocean around it, it would be useful to know more about the formation of false bottoms and to be able to model this formation process. The time scale of the development of these sheets of ice and properties such as their solid fraction could have knock-on effects on the longevity and behaviour of the pond and the false bottom in its subsequent development.

A diver's first-hand account of some of the properties of an under-ice melt pond has been published [Martin and Kauffman, 1974]. Of particular relevance to this project, we are told that a false-bottom was present; that it was about 5 cm thick; that its lower surface was fairly flat; and that its upper surface met numerous ice crystals reaching vertically from the bottom of the sea ice. It is noted that several researchers have observed a migration of false bottoms upwards over time, one suggesting a rate of approximately 1 cm day^{-1}. There are discrepancies between the accounts as to whether the ice thickens as it migrates or remains roughly the same thickness, but Untersteiner and Badgley [1958] and Hanson [1965] both report the false bottom migrating upwards through the pond at a rate of the order of 1 cm day^{-1}. It should be noted that- in one of Hanson [1965] observed sites- the two false bottoms there completely ablated.

Martin and Kauffman [1974] carried out a cold room experiment to investigate the phenomenon, identifying three phases in the evolution of the false bottom. The water

of the under-ice melt pond is relatively cool and fresh compared to the ocean below, so there is both a temperature and a salt gradient in the system. The under-ice melt pond water closest to the interface loses heat to the ocean water below it faster than it gains salt, because the rate of salt diffusion is about 100 times greater than the rate of diffusion of heat [Stern, 1960]. This creates supercooled water that is low salinity. At low salinities, supercooling of water decreases the density [Holten et al., 2012]. The supercooled water has low salinity, so is buoyant and rises through the convectively unstable pond to the top of the fresh water layer. Ice crystals then nucleate at the base of the sea ice. These ice crystals grow roughly vertically downwards through the under-ice melt pond from their nucleation sites. Eventually, after 3 days in their experiment, these ice crystals reached the interface of the pond with the oceanic mixed layer. Sometimes they grew at an angle of up to 45 degrees, intersecting one another and forming a lattice within the pond.

Secondly, the ice crystals reach the interface and form on the sides of the pool at the interface. At this point, their vertical growth rate drastically reduces and lateral freezing occurs at the interface. The horizontal projections eventually meet each other and freeze together, forming a false-bottom. This sheet of ice is typically 2 to 10 cm thick and took a total of 14 days to form in the cold room experiment.

Thirdly, the false bottom in the plexiglass tank was observed to migrate upwards at around 0.2 cm per day and thicken, freezing into the fresh water layer and ablating less rapidly at its lower interface, in the final stage of its evolution.

In this section, we explain the mathematical model that we will use to describe the lateral growth stage of false bottom development, which was originally proposed by Martin and Kauffman [1974], and present a numerical solution for the nonlinear form of this model. We also apply the same analytical solution for the linear form of the model and compare the two approaches. Finally, we will explain how the results from the lateral growth model will be used in our own simulations of the under-ice melt pond evolution in Chapters 3 and 4.

2.2   An analytical model of lateral growth

We assume that an under-ice melt pond contains thin, vertically-oriented ice crystals of separation $2a$, and set $z = 0$ as the pond-ocean interface with z increasing upwards

through the pond to (effectively) infinity. The temperature, T (K), and salinity, s, of the water that the ice crystals are growing laterally into can be described with the diffusion equations (2.1) and (2.2), together with the liquidus relation (2.3),

$$\frac{\partial T}{\partial t} = \kappa \frac{\partial^2 T}{\partial z^2} + \frac{L\rho_i}{a\rho c_p} \frac{\partial \eta}{\partial t}, \tag{2.1}$$

$$\frac{\partial s}{\partial t} = D \frac{\partial^2 s}{\partial z^2} + \frac{s}{a} \frac{\partial \eta}{\partial t}, \tag{2.2}$$

$$T = T_L(s), \tag{2.3}$$

where κ and D are the thermal and salt diffusivities respectively; L is the latent heat of the ice; ρ_i is the density of the ice; ρ is the density of the water; c_p is the specific heat of the water; a is half the separation of the vertical crystal boundaries; $\eta(z,t)$ (m) is the width of the crystal; and $T_L(s)$ is the liquidus temperature of water at salinity s [Martin and Kauffman, 1974]. This says that the change in temperature and salinity in the water between the ice crystals is affected by the diffusion of heat/salt and the release/rejection of heat/salt due to the growth of the ice crystal laterally outwards. The system of equations neglects horizontal diffusion of salt; as [Martin and Kauffman, 1974] argued, the assumption that the temperature and salinity profiles are horizontally homogeneous holds provided that the crystal separation is significantly smaller than the depth of the pond. This is the case for almost all observed under-ice melt ponds. The crystals take up a small fraction of the pond volume, so we assume that their heat capacity is negligible compared to the water phase. Since the cold room experiment suggests that their horizontal growth is slow, too, we assume there is no convection due to the growth of the crystals, and shear-driven mixing is ignored with the justification that under-ice melt ponds tend to form in hollows beneath the sea ice where they are relatively sheltered from the ocean currents below. Note that a is constant throughout the model's time frame: it refers to the initial/overall separation of the crystals, and is not limited to the (most rapidly changing) separation at the lower end of the crystals.

Equation 2.1 states that the rate of change of temperature of the water is given by the net sensible heat entering the point via conduction together with any latent heat released into the point by the lateral freezing. Equation 2.2 similarly states that the rate of change of the salinity of the water is given by the increase in salinity from salt diffusing into the domain and any increase in salinity from salt rejected by the ice matrix during freezing.

The liquidus equation, Equation 2.3, states that, if phase change is occuring, then the temperature must be equal to the liquidus point of water at the given salinity. They use a linear approximation to the liquidus curve, $T_L(s) = -ms$ with constant $m = 5.3 \times 10^{-2}$ Celsius.

Substituting (2.2) and the liquidus relation into (2.1) yields

$$\frac{\partial s}{\partial t} = \frac{DL\rho_i + s\rho c_p m\kappa}{L\rho_i + s\rho c_p m} \frac{\partial^2 s}{\partial z^2}, \tag{2.4}$$

together with the associated boundary conditions

$$s = 2s_1 \quad \text{at} \quad z = 0$$

$$s \to 0 \quad \text{as} \quad z \to \infty,$$

where s_1 is the mean salinity of the under-ice melt pond. These boundary conditions reflect the sudden jump in salinity at the pond-ocean interface, and rapid reduction above this into the fresh-water pond, as illustrated in Figure 2.1. Since the base of the ice crystals remained at roughly the same depth during this phase of the experiment, we assume that s and T are constant at $z = 0$ over the time frame we are interested in.

The salinity is then non-dimensionalised and characteristic non-dimensional parameters $\alpha_1 = \frac{\kappa}{D}$ (the Lewis number), $\alpha_2 = \frac{\Delta T_1 \rho c_p}{L\rho_i}$ (the reciprocal of the Stefan number, where ΔT_1 is the freezing point depression corresponding to s_1), and their product $\alpha_3 = \alpha_1 \alpha_2$ are substituted in, giving

$$D(1 + \alpha_3)\frac{\partial^2 \theta}{\partial z^2}\left(1 + \frac{\alpha_3}{1 + \alpha_3}\theta\right) = \frac{\partial \theta}{\partial t} \tag{2.5}$$

$$\theta = 1 \quad \text{at} \quad z = 0 \tag{2.6}$$

$$\theta \to -1 \quad \text{as} \quad z \to \infty, \tag{2.7}$$

where θ, the non-dimensional salinity, is given by $s = s_1(1 + \theta)$, and terms of order α_2 are neglected. (In the experiment of [Martin and Kauffman, 1974], α_2 was significantly smaller than the other parameters of the problem.)

For our salinity field, we have used the error function to produce a continuous step-like function, approximating the initial salinity curve presented in Figure 8 of Martin and Kauffman [1974] and satisfying the boundary conditions above. Figure 2.2 shows
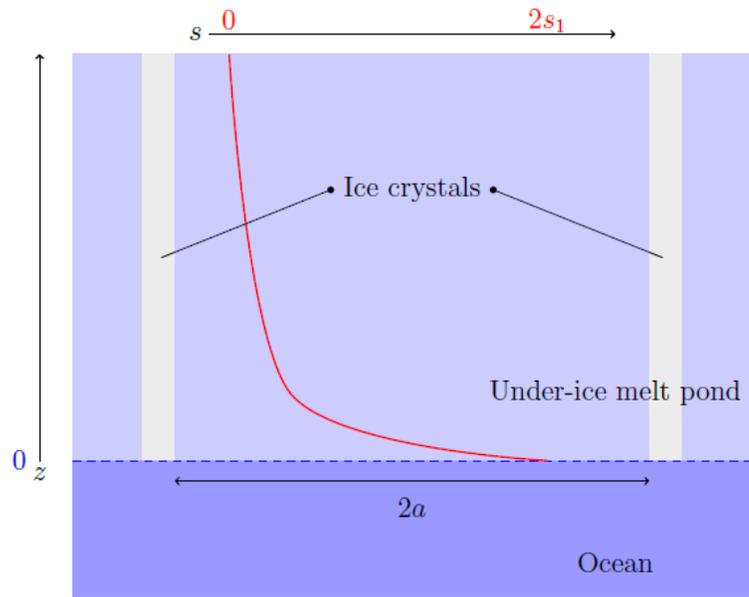
Figure 2.1: A schematic showing the geometry of the problem: an under-ice melt pond ice crystals separated by a distance $2a$, with the z axis extending upwards into the under-ice melt pond from the interface with the ocean ($z=0$, shown in dashed blue). The initial salinity profile of the pond is shown in red, with labels of 0 and $2s_1$ showing the boundary conditions.

the initial salinity profile that they refer to on the left and the initial salinity profile that we are using on the right. Note that our initial profile, Subfigure (b), only equates to the half of the salinity profile in the under-ice melt pond, where the calculations take place, while the profile in Figure 2.2 (a) extends beyond into the ocean.

(a)   (b)
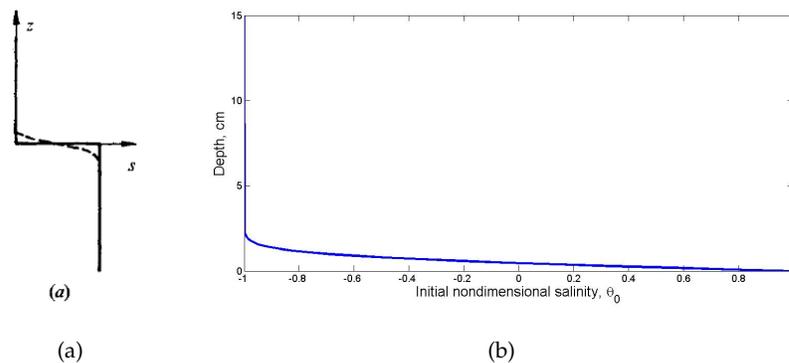
Figure 2.2: Initial salinity profiles (a) taken from Martin and Kauffman [1974]; and (b) that we are using to calculate a numerical solution to the full nonlinear diffusion equation.

Setting $D' \equiv D(1 + \alpha_3)$ and $\epsilon \equiv \frac{\alpha_3}{1+\alpha_3}$, the system reduces to the nonlinear diffusion

equation

$$D'\frac{\partial^2\theta}{\partial z^2}(1+\epsilon\theta) = \frac{\partial\theta}{\partial t},\qquad(2.8)$$

for which the change in width of the crystal is given by

$$\frac{\partial\eta}{\partial t} = -a\alpha_2\left(\frac{\partial\theta}{\partial t} - \kappa\frac{\partial^2\theta}{\partial z^2}\right).\qquad(2.9)$$

Equation 2.9 is obtained by rearranging for $\frac{\partial\eta}{\partial t}$ in the original equations and combining with the liquidus relation and nondimensionalisation of the salinity.

To solve Equation 2.8 numerically, we used the built-in Matlab routine `pdepe` [Mathworks]. Given a PDE that can be put in the form

$$c\left(x,t,u,\frac{\partial u}{\partial x}\right)\frac{\partial u}{\partial t} = x^{-m}\frac{\partial}{\partial x}\left(x^m f\left(x,t,u,\frac{\partial u}{\partial x}\right)\right) + s\left(x,t,u,\frac{\partial u}{\partial x}\right),\qquad(2.10)$$

along with an initial condition and boundary conditions, Matlab's `pdepe` function will solve a parabolic or elliptic PDE for u in space, x, and time, t, using the method of lines [Skeel and Berzins, 1990].

We set the arguments

$$m = 0,$$

$$c = 1,$$

$$f = D'\left(\epsilon\theta\frac{\partial\theta}{\partial z} + \frac{\partial\theta}{\partial z}\right), \text{ and}$$

$$s = -\epsilon D'\left(\frac{\partial\theta}{\partial z}\right)^2$$

to put Equation 2.8 in the form required by the function, and passed it the initial profile in Figure 2.2 and the boundary conditions given by 2.7 to obtain θ for each time step.

Taking the nondimensional salinity values from `pdepe`, we used a centered finite difference scheme to calculate the second-order spatial derivative of θ and integrated over time to solve Equation 2.9 and find the crystal width with depth.

Given the description of the spatial and time scales of a crystal's development in the plexiglass tank, we chose to solve the nonlinear and linearised systems over a depth of 15 cm, truncating the spatial grid that theoretically extends upwards to infinity in the vertical, and a period of 8 days, allowing us to look at the same five-day period between

days 3 and 8 that the case study crystal was observed over and to directly compare our results. Our time step was hourly and depth grid spacing was 0.1 cm, with 0 aligned with the ocean interface and z increasing upwards into the pond. The method still converges to the solution at a grid size of 1 cm, but appears blocky due to the coarseness of the spatial resolution. A grid size of 0.1 cm converges and captures the smooth profile of the curve. The solution is also reasonably invariant of the time step, with a time step 10 times smaller still allowing the method to converge on the solution, though a much coarser time step of a day leads to a slight overestimation of the growth rate and larger still time steps would prevent us from comparing between day 3 and day 8. Problematic choices of temporal and spatial resolution are flagged as warnings by the `pdepe` function. We use a crystal separation of 5 cm, and take $\alpha_3 = 1$ after [Martin and Kauffman, 1974].

2.3 Results
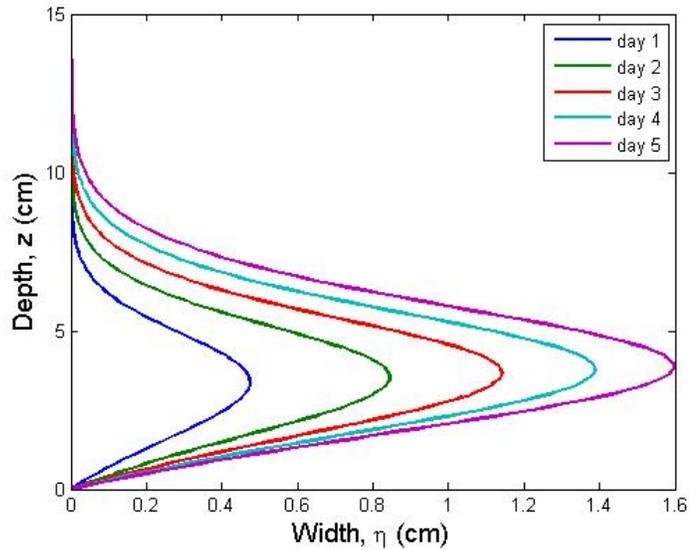
Figure 2.3: Crystal profiles calculated using our numerical routine to solve the nonlinear system of equations. Profiles for 5 days are shown, taken from the end of each 24 hours between days 3 and 8.

Crystal profiles calculated by the numerical method for the start of each day in the period between days 3 and 8 are shown in Figure 2.3. The maximum width of the crystal increases by around 1 - 2 mm each day, with the fastest growth seen in the earlier days.

The crystal shape seems similar to that observed and modelled by Martin and Kauffman [1974]. The depth at which the maximum width occurs seems to increase with time, which could be due to the diffusion of salt from the ocean into the under-ice melt pond. This could also account for the reduction in boundary velocity over time.
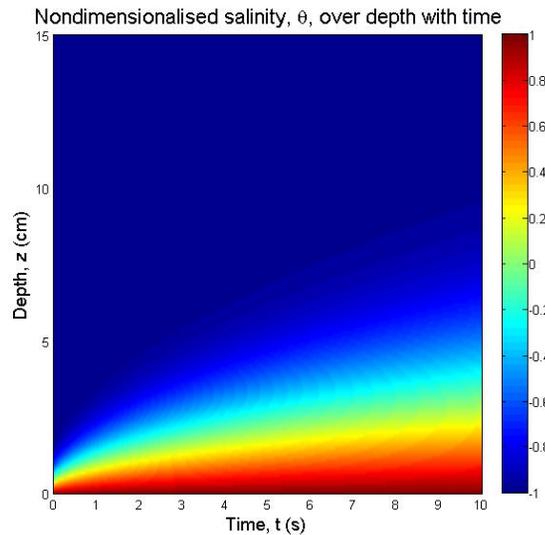
Figure 2.4: Nondimensionalised salinity in the under-ice melt pond with depth over 10 days. The lower edge, that at a depth of 0 cm, represents the pond-ocean boundary, and depth increases upwards into the pond.

Figure 2.4 shows the nondimensionalised salinity with depth over the course of 10 days. We see salt diffusing into the pond from the ocean, with concentrations highest near the pond-ocean interface and decreasing with distance from this boundary. The crystal's lateral growth rate behaves consistently with this, reducing as the water around the crystal becomes more saline.

2.3.1   Validating the model

There are no field observations to check these results against, but a sketch is given of such a crystal that formed in the cold room experiment after 5 days of growth at the pond-ocean interface. We chose the separation between the modelled crystal and the nearest other crystal to be 5 cm, as was the case for this crystal. On the left in Figure 2.5, we see a snapshot of this sketch taken from the paper, and on the right is the crystal profile calculated by our model after five days of growth shown, cropped and scaled for

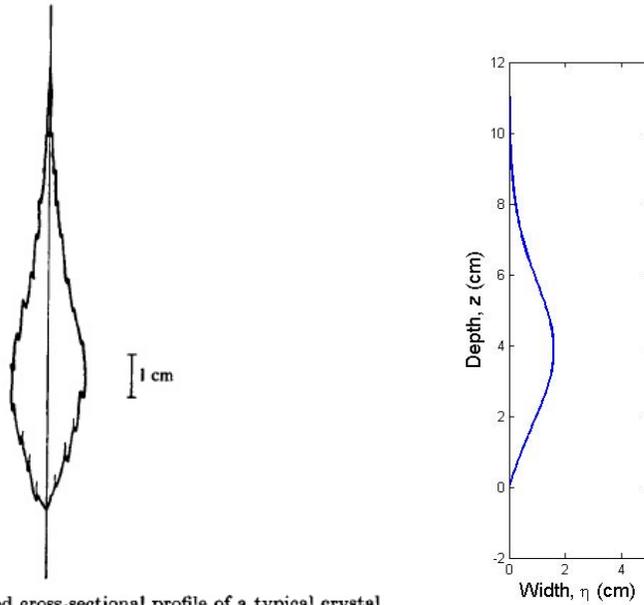easier comparison with the sketch.

FIGURE 10. The observed cross-sectional profile of a typical crystal.

Figure 2.5: (Left) Figure 10 of Martin and Kauffman [1974], showing a sketch of a crystal observed in the tank after 5 days of growth. (Right) Our simulated crystal profile after 5 days of growth.

Our crystal profile is slightly wider at its maximum but the two curves are very similar in shape when ignoring the roughness of the crystal from the experiment and taper from the widest point at similar rates.

## 2.4   Comparison with the linearised system

Martin and Kauffman [1974] noted that ϵ can be thought of as a perturbation parameter for Equation 2.8 and linearised the equation by setting $\epsilon = 0$ instead. In this limit of low epsilon, salt diffuses more strongly into the under-ice melt pond and lateral growth is slower. For a higher value of α_3, and thus higher ϵ, diffusion of salt into the pond is weaker and lateral growth is faster. For the experiment's parameter values, and in our analysis above, $\alpha_3 = 1.0$ and so $\epsilon = 0.5$. Using a standard similarity solution, this leads to an expression

$$\eta = 2a\alpha_2 \frac{\kappa}{D'} \left[\text{erf}\left(\frac{z}{2\sqrt{D't_1}} \right) - \text{erf}\left(\frac{z}{2\sqrt{D't_2}} \right) \right] \tag{2.11}$$

to approximate the increase in width, η, of a crystal at time t_2 compared to t_1. Here, a is the horizontal separation between ice crystals.

In order to compare their modelled crystal profile with that of the crystal from the tank, they chose a specifically to match the widths of the two crystals. They then note that their shape is very similar, however we are not given a direct comparison in the form of listed widths and curvatures, nor a plot of the two profiles together. The profiles are drawn in separate figures, and only the modelled profile has a complete axis attached for depth; a scale indicator is provided for the observed crystal, but not a continuous axis. The two shapes appear to be very similar, bar the roughness of the observed profile, with the modelled crystal perhaps tapering slightly more gently from its maximum width.

In the previous section, our numerical solution's crystal profile appeared consistent with the shape and width that we would expect from the experimental observations, but we also used our method to solve the linearised system in order to verify that the solution was behaving in the correct way.
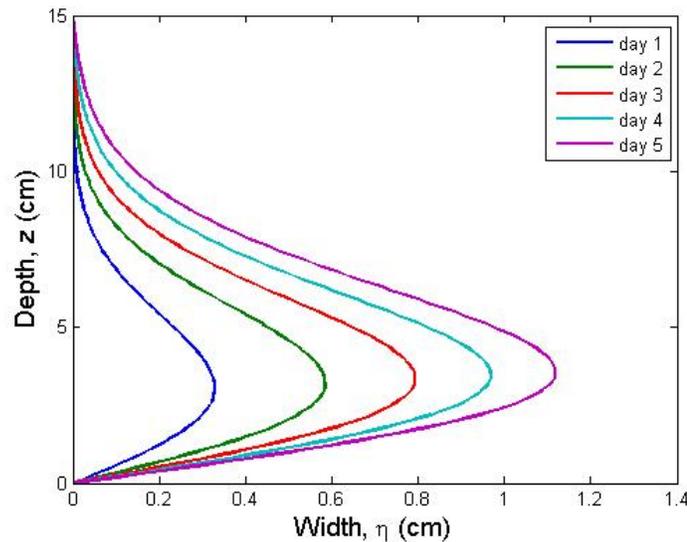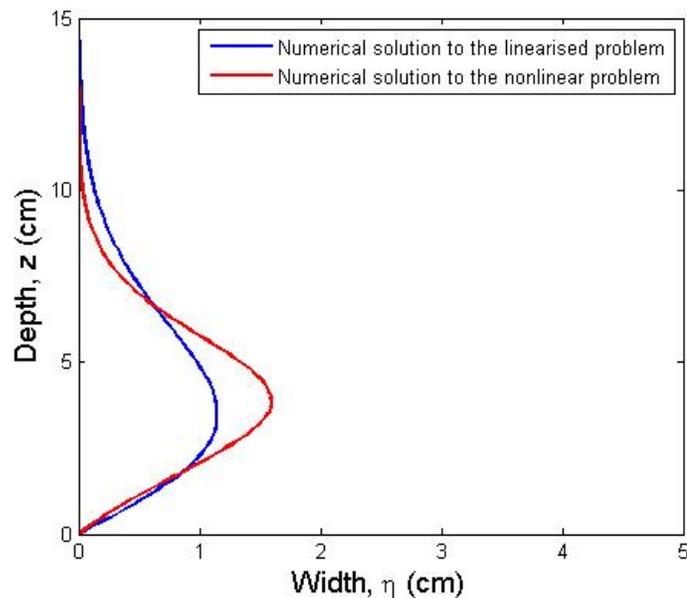

Figure 2.6: Crystal profiles calculated using our numerical routine to solve the linearised system of equations. Profiles for 5 days are shown, equating to the five day period used in the case study analysis of a crystal that formed in the cold room experiment.

We again calculated the crystal profiles for the 5-day window with the numerical routine applied to the linearised model, by setting $\epsilon = 0$ in our model, for comparison. The results for the end of each day are depicted as before in Figure 2.6. The crystal

appears to grow a little more slowly, with about 0.36 cm less lateral growth seen by the end of the fifth day simulating the linearised system compared to the nonlinear system.

Figure 2.7 compares the crystal profile found by applying our numerical scheme to the linearised problem and the crystal profile found applying our numerical solution to the full nonlinear problem. The parameter values were chosen to match those used in Martin and Kauffman [1974]. The numerical solution suggests that the lateral growth is slightly faster than predicted by the linearised model, with a horizontal maximum of 1.60 cm as opposed to 1.15 cm after 5 days. The horizontal maximum is also reached at a marginally higher depth of 3.9 cm in our numerical solution, as opposed to 3.5 cm in the analytical solution. The effect of the linearisation is to enhance the diffusion of salt into the under-ice melt pond from the ocean, which in turn raises the solidus temperature of the water and reduces the rate of lateral freezing. This is reflected in the difference in crystal widths here.


Figure 2.7: Crystal profiles after five days of growth calculated using (red) our numerical routine to solve the nonlinear system of equations and (blue) the numerical routine to solve the linearised system of equations.

2.4.1 Validation with the linearised model
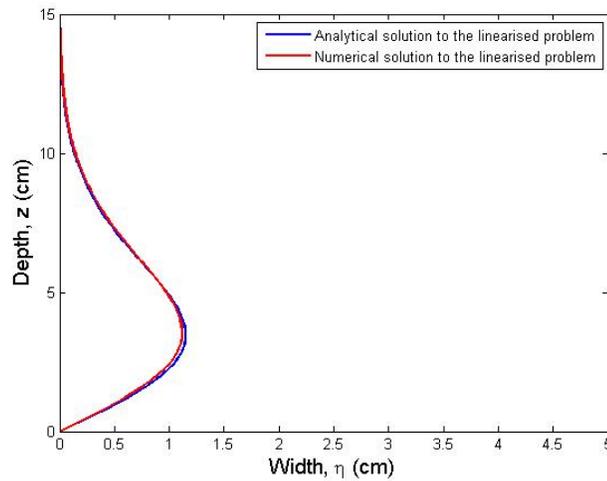
(a) Crystal profiles after five days of growth calculated using (red) the numerical routine to solve the linearised system of equations and (blue) the analytical method to solve the linearised system of equations.
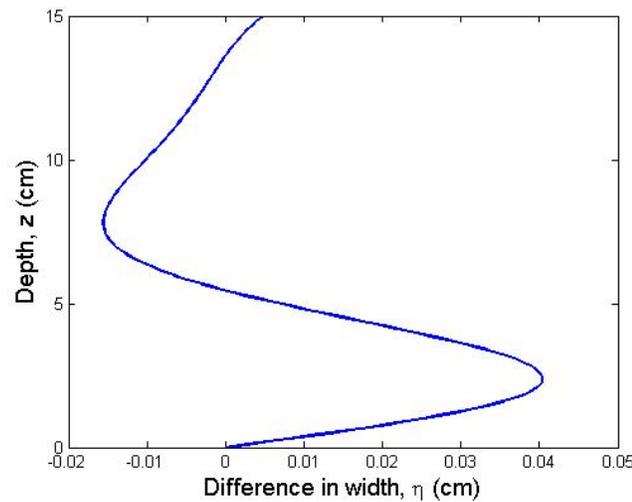
(b) The difference between the two profiles with depth.

Figure 2.8: A comparison of solutions to the linearised problem found using our numerical routine and Martin and Kauffman [1974]'s analytical method. In (a), the profiles found by the two methods are shown and, in (b), the difference between the two curves.

We can directly compare our numerical solution to the linearised problem to the analytical solution in order to validate the model more rigorously. Equation 2.8 admits a

similarity solution

$$u = \frac{z}{2\sqrt{\Delta t}}, \tag{2.12}$$

$$\theta = 1 - 2\,\mathrm{erf}(u) \tag{2.13}$$

which is trivial to calculate with only the independent variables, t and z, and key constants. We then calculate the crystal width at time t_2 using

$$\eta(t_2) = 2a\alpha\frac{\kappa}{D'}(\theta(t_2) - \theta(t_1)). \tag{2.14}$$

Figure 2.8 (a) shows the two method's solutions to the linearised problem. The two profiles seem to be in close agreement, with very similar shapes and the numerical solution underestimating the maximum width by only 0.04 cm, as is illustrated more clearly in Figure 2.8 (b), where the difference between the two curves is plotted. Our numerical model solves the linearised problem very accurately, justifying higher confidence in its solution of the nonlinear problem.

2.4.2   Consolidation and regime change criteria

Based on our results to the full nonlinear problem, false bottoms could form more quickly than originally predicted by Martin and Kauffman [1974]. Given the same crystal spacing of 5 cm as was found in the experiment for this case study, we assume the crystals reach one another and freeze together once they reach the halfway point of 5 cm, since there would be one growing from each side. After 11 days, the crystal profile of the nonlinear system has reached a maximum width of 4.9 cm, and on day 12 it has exceeded 5 cm and would have already been limited by the opposing crystal projection. We therefore end the simulation at day 11 and assume that the false bottom has then formed by the next day, day 12, with the remaining liquid taken into account in the assigned solid fraction.

Martin and Kauffman [1974] observed the false bottom in their tank to be fully formed, ie. the crystals had growth laterally and frozen together, after 14 days, so just 2 days after our model would predict. However, our estimate neglects the initial period of convection and vertical growth, which took around 3 days in the cold room experiment.

It is also reasonable to expect that not all of the crystals are spaced 5 cm apart, as this was true only for the particular crystal that Martin and Kauffman [1974] chose for their case study, and which we are modelling here: it was not a tank-wide average. The separation of 5 cm is also not listed as a maximum, but just as an example. In both Martin and Kauffman [1974]'s experiment and Campbell's observations during diving, the crystals were spaced of the order of a centimeter apart, but no details are given of the average separation or maximum separation, which would presumably be the limiting factor in determining if the false bottom was formed. Were, for example, the maximum spacing to be 7 cm, it is not unreasonable to expect that false bottom formation may be delayed from 12 days while this larger gap is filled in by lateral growth. There is presumably also a transitional period, in which the crystals are actually freezing together and the ice consolidates into a single sheet, that we have not accounted for in the proposed model here.
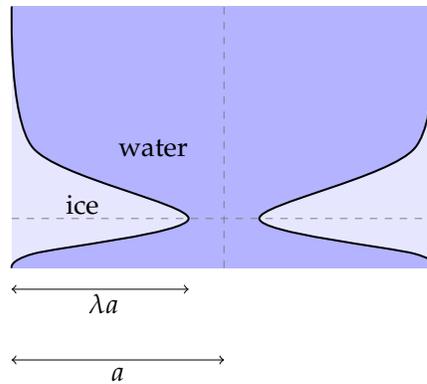
Figure 2.9: A schematic of the lateral growth of ice crystals at the pond-ocean interface, showing the relevant parameters λ and a. λ is the solid fraction of ice at the interface according to how wide the crystals have grown laterally; a is half the separation between c-axes of the ice crystals.

If a is the required distance to freeze through in order to form a false bottom and the simulation stops when the ice has grown to a maximum width of λa, where $0 < \lambda < 1$, then we give the newly formed false bottom an initial solid fraction of λ. This is illustrated in the schematic Figure 2.9. So for the case study presented in this chapter, the false bottom would be taken to be fully formed on day 12 with a high solid fraction of

$$\phi = \frac{4.9}{5} = 0.98.$$

We choose a high cut-off value of the solid fraction, $\lambda = 0.98$, since [Eicken, 1994] sug-

gests that false bottoms are nearly impermeable. Later on, in Chapter 4, we will use the work here to inform decisions in our full, multi-year sea ice-mixed layer model by using our knowledge about the time taken to form this high-solid fraction false bottom to create a parameterisation of the formation process of false bottoms beneath any under-ice melt pond that forms.

2.5 Conclusions and discussion

In this chapter, we have presented a model of the lateral growth of crystals at the interface between an under-ice melt pond and the ocean below. We have solved the model numerically for the width of the crystal at a given time, choosing parameters similar to those in a similar case study carried out by Martin and Kauffman [1974]. This allowed us to validate the model against the same crystal profile observed in their experiment. Our model reproduces the crystal shape well and grows outwards at the interface over time as expected. We then further compared, and were able to more rigorously validate, the numerical routine with the linearised problem.

Since the initial convection in the pond and the vertical growth of the crystals downward towards the interface took little time relative to the lateral growth of the crystals, we have decided not to model these stages of false bottom development. It would require a substantial amount of work and many simplifying assumptions for only a small additional accuracy in the full model of under-ice melt pond evolution that we aim to develop. A complete model would, however, include these stages.

We neglected the heat capacity of the ice crystals in this study, while in reality a fraction of the latent heat released during freezing would go into warming the crystals, and heat would be transferred between the water and the ice. This is not likely to lead to a large change in the qualitative outcome of our results, however. The ice crystals were assumed to be solid rather than mushy in our approach. A more realistic treatment of the thermodynamics would include the presence of the brine phase within the crystals, though the false bottom has been observed to be nearly impermeable; assuming the ice crystals have a similarly high solid fraction, then the effect of the brine would be minimal. The crystals are also very thin and needle like, making up only a small fraction of the volume of the pond. Improving their representation in the model is therefore

unlikely to drastically change our results. We also neglect the effects of convection in the water phase. A complete model would include any convection of heat and salt into the pond, though in the sheltered geometry of an under-ice melt pond these effects are likely to be minimal.

Our numerical solution to the full nonlinear problem does not differ significantly from that of the linearised problem, suggesting only that the false bottom may form a couple of days more quickly than the analytic solution to the linearised problem implies. Our case study suggests that, given a maximum crystal spacing of 10 cm, the false bottom would take 12 days to form. This could be a slight underestimate depending on maximum crystal separation and the time required for the horizontal projections to consolidate into a single ice sheet.
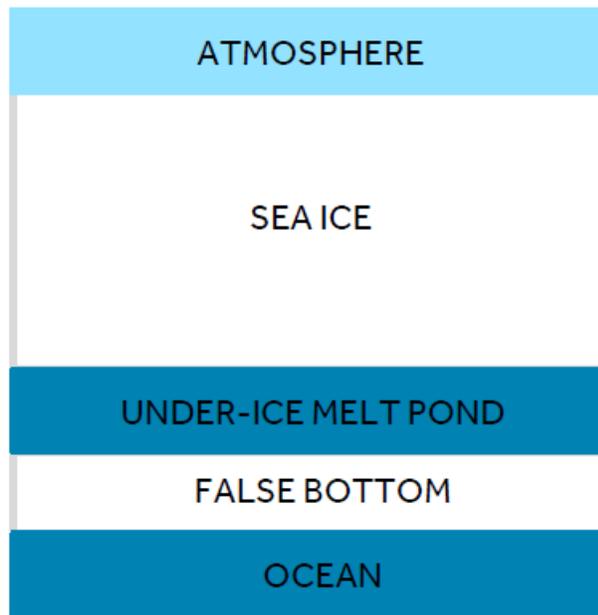
Chapter 3

Under-ice melt pond evolution

3.1 Introduction

In Chapter 1, we discussed several attempts at modelling the evolution of false bottoms once they have formed from the lateral projections of ice crystals at the pond-ocean interface. Each model only considered the false bottom interfaces as part of a semi-infinite domain in each direction. This means that the false bottom can never freeze through the under-ice melt pond, since there is no sea ice above for it to meet. These studies also neglected the impact of salinity within the under-ice melt pond. If the false bottom migrates upwards through the fresh water layer, salt will be rejected from the ice matrix into an increasingly smaller pond volume, increasing its salinity. This would decrease the rate of freezing of the ice-pond interface, and could even cause ablation.

In this chapter, we propose a more complete model not just of false bottom evolution, but also of the under-ice melt pond and the sea ice above them. We model the thicknesses of each layer of a system containing a slab of sea ice sitting above an under-ice melt pond with a fully-formed false bottom. We calculate the impact of the under-ice melt pond's salinity on the freezing/ablation rate of the ice, and include any change to the pond salinity from brine rejection from the freezing ice.

Using this model, we will explore the possible outcomes once the false bottom has formed and attempt to capture the evolution of an under-ice melt pond observed in the field. We will then test the sensitivity of the model to various key parameters and deduce the impact that the ponds have on the mass balance of the sea ice both locally and regionally.

Figure 3.1: A schematic of the setup of strata that we are modelling in this chapter.

3.2   A model of under-ice melt pond and false bottom evolution

We have developed a one-dimensional model to investigate the life cycle and impacts of under-ice melt ponds. While previous studies have modelled the false bottom in isolation [Notz et al., 2003; Alexandrov and Nizovtseva, 2008], we are simulating a slab of sea ice sitting above an under-ice melt pond, which is trapped against the ice by a fully formed false bottom. Below this is the ocean. This setup is illustrated in Figure 3.1. We do not include a surface melt pond above the sea ice, but we will consider the potential impact of doing so later. The primary change would be a reduction of the albedo of the ice, which would allow more heat to be absorbed into the system from radiation. The temperature profile of the sea ice would also change, rising to the liquidus temperature of the ice at the interface with the surface melt pond and seeing warming due to the release of latent heat during the refreezing of the melt pond. These changes would all have the effect of prolonging the time taken to freeze the under-ice melt pond or speeding up the time taken for a false bottom to melt.

When considering phase change, we use front-tracking rather than an enthalpy model. Taking an enthalpy approach has the advantage of better representing the bound-

aries between the difference sections of different phases in the system. In using a front-tracking method, typically one has to assign a solid fraction at the freezing/melting boundaries between phases while the mathematical theory, backed up by observations, informs us that the solid fraction at the phase boundary must be zero during freezing Notz and Worster [2006]. An enthalpy approach is able to fully represent the solid fraction of the sea ice at these points. More straight-forward front-tracking methods have none-the-less been proven capable of representing similar layered pond-ice scenarios well, such as that of [Maykut and Untersteiner, 1971], and since we are using a mushy-layer approach, we are still able to determine the solid fraction using the ratio of brine salinity to bulk salinity.

3.2.1 Temperature and salinity evolution

The mushy layer equations are used to describe the temperature, T, evolution within the sea ice and the false bottom,

$$c_{\text{eff}}\frac{\partial T}{\partial t} = \nabla \cdot (k_{\text{eff}}\nabla T) + \mathcal{L}\frac{\partial \phi}{\partial t} - c_b \boldsymbol{u} \cdot \nabla T + A_R, \tag{3.1}$$

which says that the change in temperature over time is given by the change in temperature due to heat diffusion plus any change due to phase change minus any advection of heat out of the region, plus any heating due to radiation. Here, c_{eff} is the effective volumetric specific heat capacity and k_{eff} is the effective thermal conductivity, calculated as per Feltham et al. [2006]. $\mathcal{L}$ is the latent heat of fusion per unit volume, ϕ is the solid fraction, c_b is the specific heat capacity of the brine portion of the mushy layer, $\boldsymbol{u}$ is the Darcy velocity of the brine phase, and A_R is the heating due to radiation.

The local salt balance is then similarly given by

$$(1 - \phi)\frac{\partial C}{\partial t} = \nabla \cdot (D_m \nabla C) + \frac{\rho_i}{\rho_b}(C - C_i)\frac{\partial \phi}{\partial t} - \boldsymbol{u} \cdot \nabla C, \tag{3.2}$$

for brine salinity C. Here, D_m is the diffusion coefficient of salt within the medium, ρ_i is the density of ice, ρ_b is the density of the brine, and C_i is the salinity of the ice. The temperature and salinity are linked by the liquidus relation,

$$T = T_L(C) = T_L(0) - \Gamma C, \tag{3.3}$$

where Γ is a positive constant.

The temperature evolution in the pond is given by a diffusion equation, Equation 3.4, with enhanced transfer coefficient, κ, due to turbulent mixing. Salt is treated similarly, as seen in Equation 3.5, with a turbulence-enhanced diffusion coefficient, D_{turb}. The equations are

$$\frac{\partial T}{\partial t} = \frac{\partial}{\partial z}\left(\kappa \frac{\partial T}{\partial z}\right) + \frac{1}{c_{\text{eff}}}\frac{\partial F_{\text{net}}(z)}{\partial z}, \tag{3.4}$$

$$\frac{\partial C}{\partial t} = \frac{\partial}{\partial z}\left(D_{\text{turb}}\frac{\partial C}{\partial z}\right). \tag{3.5}$$

Here, $F_{\text{net}}(z)$ is the net radiation at depth z.

3.2.2 Boundary conditions

3.2.2.1 Ice-Atmosphere

At the top of the domain, an energy balance is used to calculate the ice's surface temperature. The incoming longwave and shortwave radiation, F_{LW} and F_{SW}; outgoing blackbody radiation; sensible heat flux, F_{sens}; latent heat flux, F_{lat}, and conductive heat flux must be in equilibrium, together with any change in energy due to surface melting in the summer months:

$$F_{\text{LW}} + (1-\alpha)(1-\iota)F_{\text{SW}} - \epsilon\sigma T^4_{\text{surface}} - F_{\text{sens}} - F_{\text{lat}} - k_{\text{eff}}\left.\frac{\partial T}{\partial z}\right|_{\text{surface}}$$
$$= \begin{cases} 0 & \text{if } T_{\text{surface}} < T_L \\ \phi\mathcal{L}\left.\frac{\mathrm{d}h}{\mathrm{d}t}\right|_{\text{surface}} & \text{if } T_{\text{surface}} = T_L, \end{cases} \tag{3.6}$$

where ϵ is the emissivity, σ is the Stefan-Boltzmann constant, T_{surface} is the temperature at the surface of the sea ice, α is the ice's albedo, $1-\iota$ is the fraction of shortwave radiation absorbed at the surface, k_{eff} is the effective thermal conductivity, and h is the thickness of the sea ice layer above the under-ice melt pond.

After Taylor and Feltham [2004], the sensible and latent radiation are given by

$$F_{\text{sens}} = \rho_{\text{air}}c_{\text{air}}\mathcal{C}_T u(T_{\text{air}} - T_{\text{surface}}) \tag{3.7}$$

and

$$F_{\text{lat}} = \rho_{\text{air}} \mathcal{L}_v \mathcal{C}_T u (q_{\text{air}} - q_{\text{surface}}) \tag{3.8}$$

respectively, where ρ_{air} is the density of the air, c_{air} is the specific heat capacity of the air, $\mathcal{L}_v$ is the latent heat of vaporisation, $\mathcal{C}_T$ is a bulk transfer coefficient, T_{air} is the 2 m air temperature, q_{air} is the 2 m specific humidity of the air, and q_0 is the specific humidity at the surface of the sea ice.

3.2.2.2 Pond-ice boundaries

Using Beer's law to calculate the radiation attenuation with depth would entail larger errors due to the presence of stacked layers of different optical properties. Back-scattering will occur at each interface, and the ice and water layers will have different attenuation coefficients. Instead, we use a two-stream radiation model whereby the net radiation in each layer is given by the difference between the upwelling and downwelling radiation in each layer, as was used to good effect in the surface melt pond model of Taylor and Feltham [2004]. The change in upwelling and downwelling radiation, $F_\uparrow$ and $F_\downarrow$, in each layer with depth are given by Equations 3.9 and 3.10 respectively, and the net radiation in each layer is given by the difference between them:

$$\frac{\partial F_\uparrow}{\partial z} = (r + \kappa) F_\uparrow - r F_\downarrow, \tag{3.9}$$

$$\frac{\partial F_\downarrow}{\partial z} = r F_\uparrow - (r + \kappa) F_\downarrow, \tag{3.10}$$

$$F_{\text{net}} = F_\uparrow - F_\downarrow, \tag{3.11}$$

where κ is the absorption coefficient for the layer and r is the scattering coefficient. At the boundary between each pair of adjacent internal layers, the upwelling and downwelling stream values must be equal to those at the top of the next layer. This conserves energy, though causes us to neglect any scattering at the interfaces between the layers. This might lead to a small over-estimation in the amount of energy reaching the lower levels of the system. Since the majority of the radiation is absorbed at the surface of the sea ice anyway, and we include scattering within the layers, this effect is likely to be small. We do account for the Fresnel component of the radiation at the surface of the sea ice, where the difference in refraction indices of the two media is large, but between the ice and

water layers it is assumed that refraction indices are similar. The two-stream radiation model also operates under the assumption that any incoming radiation is diffuse. This is largely true for the summer months, in which cloud cover is high, but could introduce errors in winter when radiation could regularly meet the ice from a specific incident angle.

Stefan conditions describe the change in position of the ice-water interfaces with time as the ice ablates or grows. To find the boundary velocity, heat fluxes at each side of the boundary are balanced:

$$\rho \mathcal{L} \phi_a \frac{\mathrm{d}h_a}{\mathrm{d}t} = k_{\mathrm{eff}_a} \frac{\partial T}{\partial z}\bigg|_{\mathrm{ice}_a} - k_{\mathrm{pond}} \frac{\partial T}{\partial z}\bigg|_{\mathrm{pond}_a} \tag{3.12}$$

$$\rho \mathcal{L} \phi_b \frac{\mathrm{d}h_b}{\mathrm{d}t} = k_{\mathrm{eff}_b} \frac{\partial T}{\partial z}\bigg|_{\mathrm{ice}_b} - k_{\mathrm{pond}} \frac{\partial T}{\partial z}\bigg|_{\mathrm{pond}_b}, \tag{3.13}$$

where k_{pond} is the thermal conductivity of the under-ice melt pond, parameters with the subscript a correspond to the boundary between the sea ice and the under-ice melt pond, and those with the subscript b corresponds to the boundary between the under-ice melt pond and the false bottom.

We assume that any diffusive salt transport within the sea ice is negligible. Including the desalination of the lower levels of the sea ice due to diffusion of fresh water from the pond into the ice could improve estimates of the pond salinity. As a first approximation, however, we only consider the change in pond salinity from any increase or decrease due to the change of the pond volume, as well as the effect of any salt rejected or fresh water melt released, during the freezing or ablation of the pond-ice boundaries. Where the ice has bulk salinity C_{bulk}, this is given by a change in salinity

$$\frac{\mathrm{d}C_{\mathrm{pond}}}{\mathrm{d}t} = \frac{1}{h_{\mathrm{pond}}} \left(C_{\mathrm{bulk}_a} \frac{\mathrm{d}h}{\mathrm{d}t}\bigg|_a - C_{\mathrm{bulk}_b} \frac{\mathrm{d}h}{\mathrm{d}t}\bigg|_b \right). \tag{3.14}$$

We assume that the temperature at these constantly growing and ablating boundaries satisfies the liquidus relation for the local brine salinity,

$$T = T_L(C_{\mathrm{pond}}) = T_L(0) - \Gamma C_{\mathrm{pond}}. \tag{3.15}$$

3.2.2.3   Ice-ocean boundary

At the boundary between the sea ice or the false bottom and the ocean, the upwelling radiation must be equal to 0.

The change in position of this boundary is given by

$$\rho \mathcal{L} \phi_o \frac{\mathrm{d}h}{\mathrm{d}t}\bigg|_o = k_{\mathrm{eff}_o} \frac{\partial T}{\partial z}\bigg|_o - F_{\mathrm{ocean}}, \tag{3.16}$$

where F_{ocean} is the heat flux upwards from the ocean into the ice, and parameters with the subscript o correspond to the boundary between either the false bottom or the sea ice and the ocean, depending on whether a false bottom is present or not. If a false bottom is present, ϕ_o is therefore the solid fraction at the base of the false bottom, while if there is no false bottom, ϕ_o is the solid fraction at the base of the sea ice.

We will use a prescribed far-field salinity in the liquidus relation, Equation 3.15, to find the temperature at this lowest boundary.

3.2.3   Implementation

We solved the model presented at the start of this chapter numerically in order to investigate the evolution of under-ice melt ponds and false bottoms. We assume that the temperature profile in each layer is linear at the start of the simulation and use Matlab's `pdepe` routine to solve the PDEs for temperature within each layer in each subsequent timestep. The `pdepe` routine uses method of lines and a spatial finite element discretisation [Skeel and Berzins, 1990]. The salinity of the under-ice melt pond is updated via a finite difference scheme for the change due to ice growth/ablation according to Equation 3.14. We choose the coefficent $\Gamma = 0.0514$ in the liquidus relation, as was used in Taylor and Feltham [2004].

NCEP forcing is used in calculating the energy balance at the surface [Kalnay et al., 1996], Equation 3.6, directly for the incoming shortwave and longwave radiation, and through the 2 m air temperature used to calculate the sensible and latent heat, which are given respectively by Equations 3.7 an 3.8. A climatology generated from the years 1981 to 2010 of these data is shown in Figure 3.2. The forcing data are taken for the location 80 N 210 E in both the reference case and the sensitivity studies of this chapter, though we carry out a more systematic sensitivity study to the forcing data location in Chapter

4.
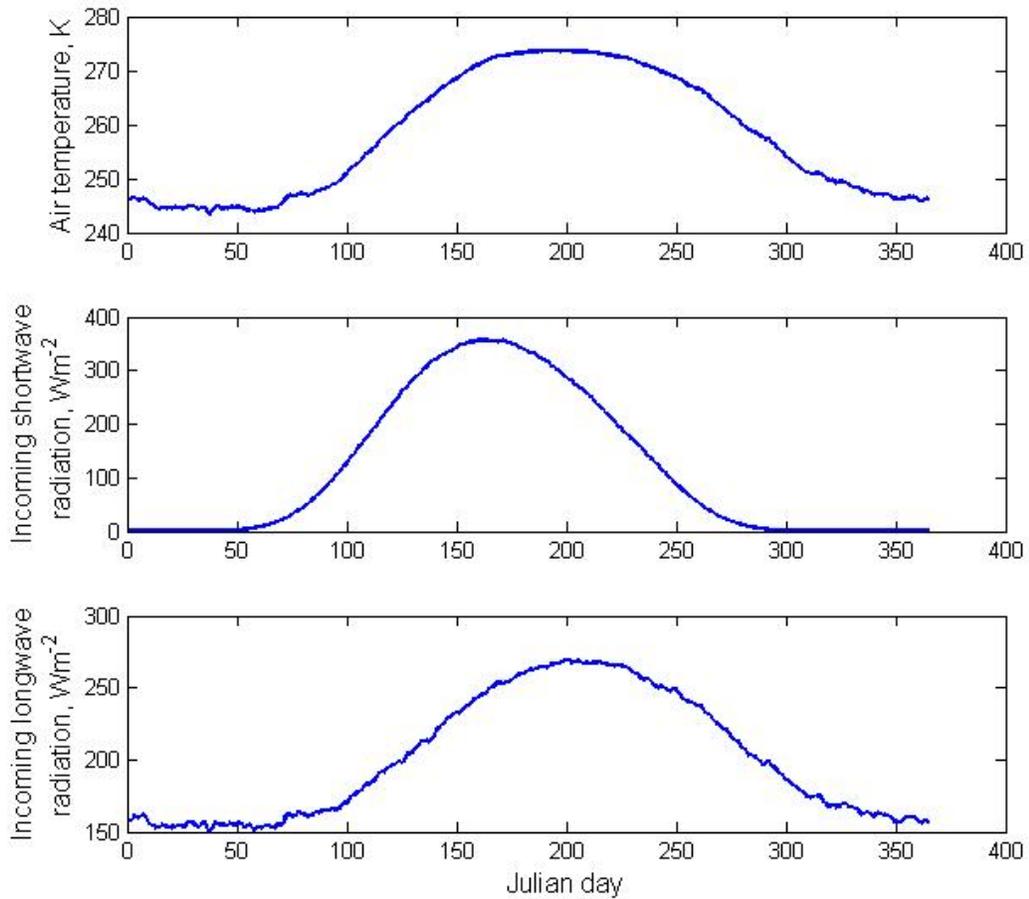
Figure 3.2: Air temperature, incoming shortwave radiation, and incoming longwave radiation climatologies from NCEP data.

The oceanic forcing is assumed to be constant at 2 Wm^2, and we take the sea ice to be 80 cm thick at the beginning of the simulation, which corresponds to the start of September. We assume the false bottom has already formed at the start of the simulation and is initially 2 cm thick, beneath an under-ice melt pond 20 cm deep.

3.2.3.1   Discretisation and thresholds

We use a spatial grid of 80 grid cells in the parent sea ice, 20 in the under-ice melt pond, and 10 in the false bottom. The size of a grid cell for each layer is calculated at the

beginning of each time step. We use a timestep of 6 hours, though we use climatologies containing daily average values. We assume the temperature remains constant at this daily mean for the four time steps corresponding to that day. The grid size and time step were chosen such that the method converges to a stable solution for the range of initial conditions that we use in this chapter.

The salinity of the under-ice melt pond could prevent it from completely freezing as it reaches very shallow depths, so we set a cut-off pond depth of 1 cm, after which it is assumed that the pond has frozen. We also set a cut-off thickness for the false bottom of 0.5 cm, below which it is assumed to have ablated.

An error in the total amount of salt present is introduced when calculating bulk salinity and boundary changes on a discretised grid. In each timestep, the new boundary position is found by solving a Stefan condition. This gives a solution in continuous space, which will almost certainly not match up with the discretised grid. To fix this, we alter the bulk salinity calculation to take into account the number of grid cells being melted or grown. First of all, we calculate how many grid cells the change in boundary condition of ice phase X equates to, G, using

$$G = \text{round}\left(\frac{\mathrm{d}h^X}{\mathrm{d}t}\right)\frac{n^X}{H^X}. \tag{3.17}$$

Here, superscript X refers to the layer of ice in question, n is the number of grid cells in that layer, H is its thickness, and $\frac{\mathrm{d}h^X}{\mathrm{d}t}$ is the change in position of the boundary between that ice layer and water. We then determine the new bulk salinity (time t_{i+1}) at the ice-pond boundary using

$$C_{\text{bulk}}^X(t_{i+1}, n) = \begin{cases} C_{\text{bulk}}^X(t_i, G) & \text{if melting} \\ C_{\text{pond}}(1 - \phi^X) & \text{if freezing} \end{cases} \tag{3.18}$$

and the new ice phase X bulk salinity profile using

$$C_b^X(1:G) = C_{\text{bulk}}^X(t_i)|_e nd \tag{3.19}$$

if freezing. If melting, we linearly interpolate the previous bulk salinity profile with the new bulk salinity at the boundary.

We added a calculation of the change in bulk salinity at the base of the false bottom, too. Finally, after calculating the new salinities in the ice, we calculate the difference in salt and attempt to correct for this by subtracting some of this salt from each ice grid cell. This is not perfect, largely due to the error in rounding the boundary change to a multiple of grid cell size when calculating the bulk salinities at the boundary, but still significantly reduces the error in total salt to a negligible amount.

3.3 Results

Much of the literature surrounding under-ice melt ponds suggests that false bottoms thicken over time and 'migrate' upwards, with the false bottom growing at its upper interface with the pond faster than its lower interface with the ocean ablates. From our simulations, we see that this is actually one of two possible outcomes. Under certain initial conditions, the false bottom migrates upwards and thickens to begin with but eventually ablates at the upper interface. This is because the under-ice melt pond's salinity increases as the sea ice and false bottom freeze into it: salt is rejected from the ice matrix and into a pond of shallower depth than before. The freezing point of sea water increases as salinity increases so the ice growth slows and, if the water becomes saline enough, the ice may ablate. This second outcome was observed in the field work of Hanson [1965], in the location where two false bottoms had formed.

In this section, we will describe two case studies that illustrate the two possible outcomes, then test the models ability to replicate the evolution of an observed under-ice melt pond. We present the results of our sensitivity studies and will then discuss the regional impact that our model predicts the under-ice melt ponds have on the mass balance of the sea ice.

3.3.1 Freezing case study: a low salinity under-ice melt pond

When the initial salinity of the under-ice melt pond is low, just a few psu, we found that the false bottom is often able to completely freeze through this fresh water layer. This process typically takes place over fairly short time scales, usually just a few days. In Figure 3.3 we see the ice-water boundary positions with time for an under-ice melt pond with an initial salinity of just 2 psu. The blue line corresponds to the sea ice-pond
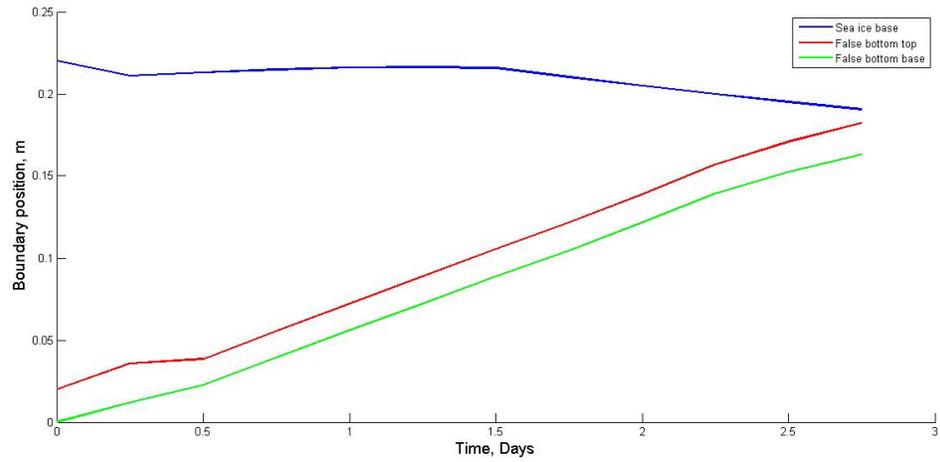
Figure 3.3: Boundary position evolution for a pond of initial salinity 2 psu and an associated false bottom.

interface, the red line corresponds to the false bottom-pond interface, and the green line corresponds to the false bottom-ocean interface. At the start of the simulation, the pond is 20 cm deep, the false bottom is 2 cm thick, and the sea ice above them is 1 m thick.
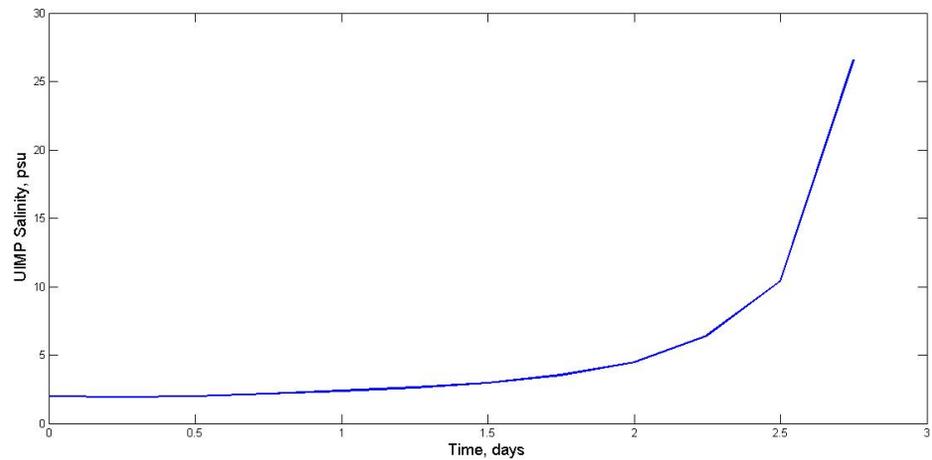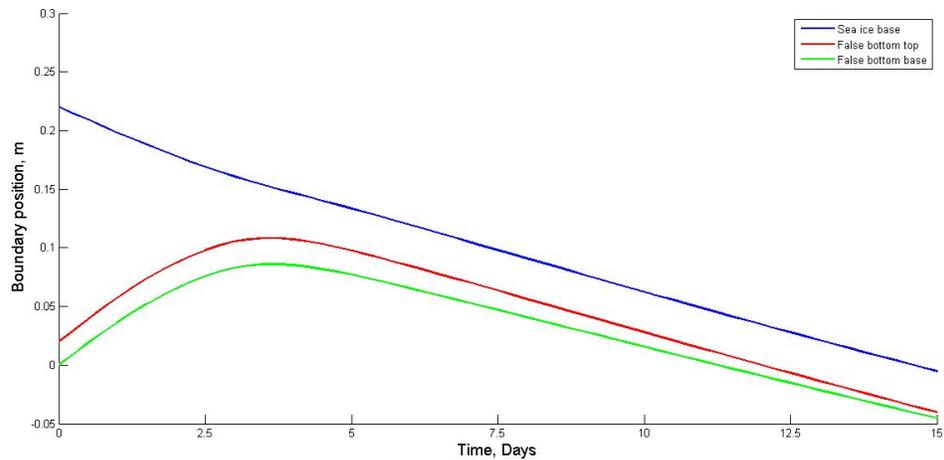

Figure 3.4: Salinity of an under-ice melt pond over time, from an initial salinity of 2 psu.

The false bottom migrates rapidly upwards through the pond at a rate of roughly 6 cm day^{-1}, freezing through the fresh water layer in less than three days. This growth rate can be verified through analytics. The growth rate of the lower boundary is given

by

$$\left.\frac{\mathrm{d}h}{\mathrm{d}t}\right|_o = \frac{1}{L\phi\rho}\left(k_eff\frac{\partial T}{\partial z} - F_{\text{ocean}}\right)$$

$$\sim \frac{1}{3\times10^8\times0.8\times1.09}\left(2\frac{\Delta T}{\Delta H_{\text{false bottom}}} - 2\right)$$

$$\sim \frac{1}{3\times10^8\times0.8\times1.09}\left(2\frac{T_L(C_O) - T_L(C_{\text{pond}})}{0.02}\right)$$

$$\sim \frac{1}{3\times10^8\times0.8\times1.09}\left(2\times\frac{(271.2 - 273.0)}{0.02} - 2\right)$$

$$= 7.2\times10^{-7}\ \text{m s}^{-1}$$

$$= 6.1952\ \text{cm day}^{-1}.$$

The pond salinity remains fairly constant until the final stages of freezing, so the growth rate remains approximately linear throughout the evolution of the false bottom. The pond and oceanic heat fluxes into the false bottom are relatively small compared to the internal conductive heat flux, so both boundaries of the false bottom migrate at roughly similar rates, dominated by the conductive heat flux through the false bottom. The boundary between the sea ice and the pond also grows into the fresh water, but at a significantly lower rate of around 1 cm day^{-1}. The salinity of the pond increases monotonically as the ice grows, rising from 2.0 to 26.6 psu, as shown in Figure 3.4.

Figure 3.5: Boundary position evolution for a pond of initial salinity 10 psu and an associated false bottom.

3.3.2   Ablating case study: a more saline under-ice melt pond

Keeping the same initial parameter values as in the low salinity case study above but increasing the initial pond salinity to 10 psu, we see a different type of false bottom evolution, displayed in Figure 3.5. In this scenario, the false bottom migrates upwards through the pond and thickens over the first 4 days, before shifting downwards again as the upper interface ablates. Eventually, it thins to below the critical thickness and is considered to have completely vanished.
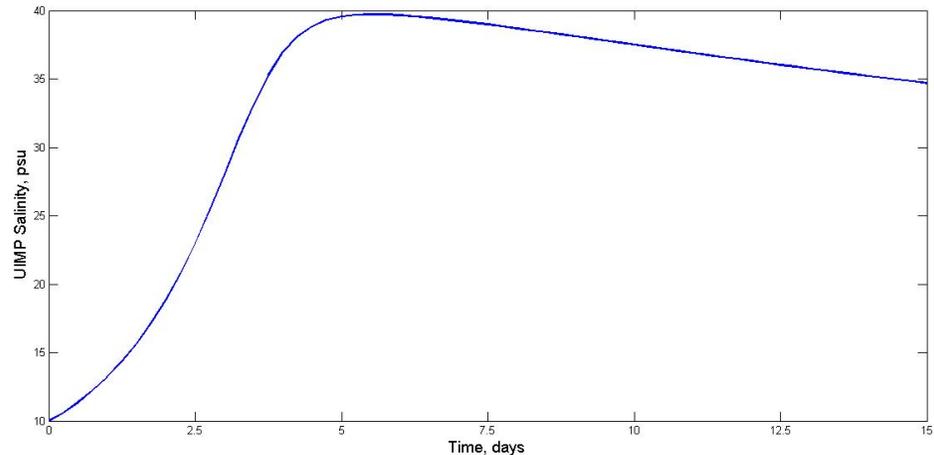
**Figure 3.6:** Salinity of an under-ice melt pond over time, from an initial salinity of 10 psu.

The eventual thinning of the false bottom is because the salinity in the pond reaches such high values that the ice stops growing and ablates instead. In Figure 3.6, we see the pond salinity rise from 10.0 to a maximum of 39.7 psu, significantly higher even than the ocean salinity of 33 psu. This reverses the temperature gradient in the false bottom ice sheet and it begins to ablate at its upper boundary. The pond freshens slightly due to the combined effects of this ablation and that of a small increase in pond depth, but not enough to begin freezing from below again.

Most observational studies have not included data on the eventual state of this phenomenon, so its is useful to see from modelling that these two outcomes are viable.

3.3.3   Comparison with observations

There have been relatively few continuous field observations of under-ice melt ponds to compare our model with. Hanson [1965] provided schematic diagrams of under-ice melt ponds in their observation sites, though with some notable differences to the scenarios our model is capable of replicating. Firstly, stacked false bottoms are shown in both plots, and secondly, a surface melt pond in the process of refreezing is present in one plot. In their plot containing a surface melt pond, the two false bottoms join together to form one ice sheet, making the time period after this perhaps the simplest to reproduce with our model.

By setting the surface temperature of the sea ice in our model equal to the liquidus temperature (273.15 K) and lowering the albedo to 0.4 following the results of [Perovich et al., 2002], we can capture some of the effect of the surface melt pond on the sea ice's temperature profile. From the diagram of Hanson [1965], we can approximate that there is about 50 cm of sea ice, an under-ice melt pond of around 84 cm depth, and a false bottom of roughly 12 cm thickness on August 25th. We ran our model using these initial conditions in time steps of 6 hours for 30 days from this date and compared our model output with Hanson's diagram in Figure 3.7. We had to guess the under-ice melt pond salinity, which we took to be a fresh 2 psu, and used an oceanic heat flux of 10 W m^{-2}.
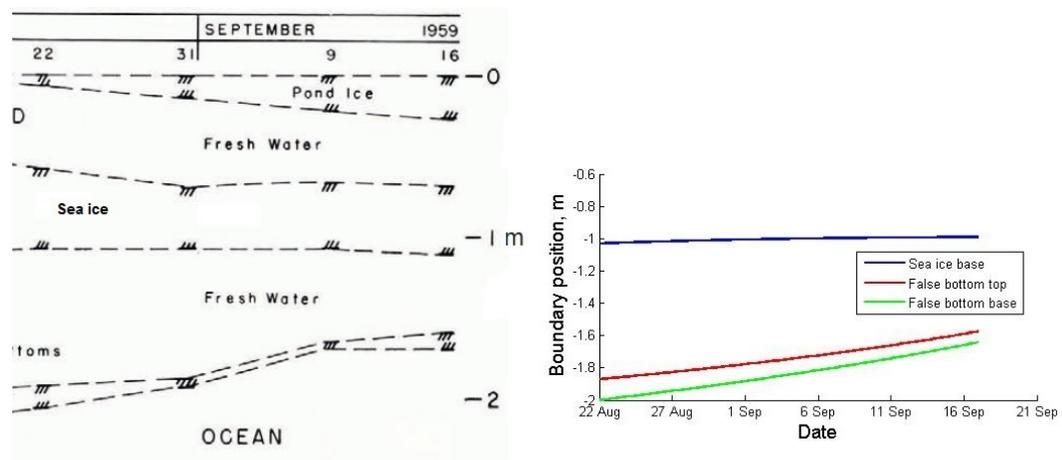
Figure 3.7: (Left) A snapshot of the boundary positions of a surface melt pond, sea ice, under-ice melt pond, and false bottom measured in the field. Taken from Hanson [1965]. (Right) Boundary positions calculated by our model for 25 days from August 22nd. Initial positions were estimated by eye from the diagram, the temperature at the surface of the sea ice was set to the liquidus temperature and the surface albedo was lowered to reflect the presence of a surface melt pond in the observations.

The boundary positions calculated by our model are shown on the right, while a snapshot of the figure from Hanson [1965]'s article is shown on the left. Our figure has been sized to match the vertical scale of the diagram as closely as possible. The behaviour of the ice-water boundaries are in remarkable agreement given that we do not have complete data for the site and do not model the surface melt pond. Our false bottom thins slightly over time, albeit in a more uniform fashion than the observed false bottom. The observed ponds seems to shrink to about 60% of its depth, while ours remains slightly larger at 70% of its original depth. Since the false bottoms both migrate up about 30 cm, this difference in final pond depth is probably due to the small difference in the sea ice base position. In their diagram, the observed sea ice grows a little into the under-ice melt pond after ablating for a while in late August, whereas our modelled false bottom continues to ablate at a reduced rate in September.

Some small details are different between the observed and modelled false bottoms. The observed false bottom, for example, exhibits a decrease in average thickness but its actual change in thickness is not monotonic: it thins after the two false bottoms join together to form a thick false bottom, then thickens again in September. Our modelled false bottom thins much more smoothly. Overall, however, our model captures the evolution of the pond and false bottom well given a likely error introduced in the estimation of the initial conditions.

3.4   Sea ice mass balance

We now want to use this model to assess the impact that an under-ice melt pond has on the parent sea ice above it. To quantify the effect that under-ice melt ponds have on the thickness of the parent sea ice, we carry out two simulations, whose initial setup is illustrated in Figure 3.8.

Firstly, we take a slab of ice of thickness H_0 sitting directly above the oceanic mixed layer. We allow this slab to evolve for 50 days, and note its thickness H_1 at the end of the 50 day period. Secondly, we take an identical slab of sea ice, again of thickness H_0, this time sitting above an under-ice melt pond and false bottom. The ice-ocean interface is now at the lower boundary of the false bottom instead of the base of the sea ice.

Having seen that there are two possible final outcomes to the false bottom's evolu-
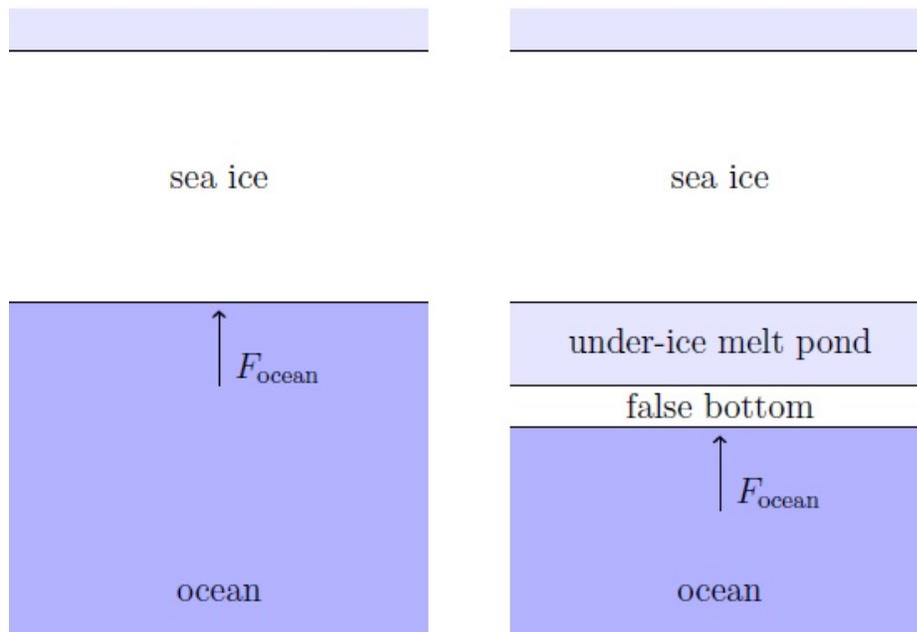
Figure 3.8: A schematic of the initial states of the two simulations that we run to assess the effect of under-ice melt ponds on the parent sea ice thickness.

tion, we need to take this into account when allowing this second, more complex system to evolve. In one case, the false bottom may freeze through the entire under-ice melt pond. At this point we assume it consolidates together with the sea ice, forming a larger slab of sea ice, as illustrated in Figure 3.9.
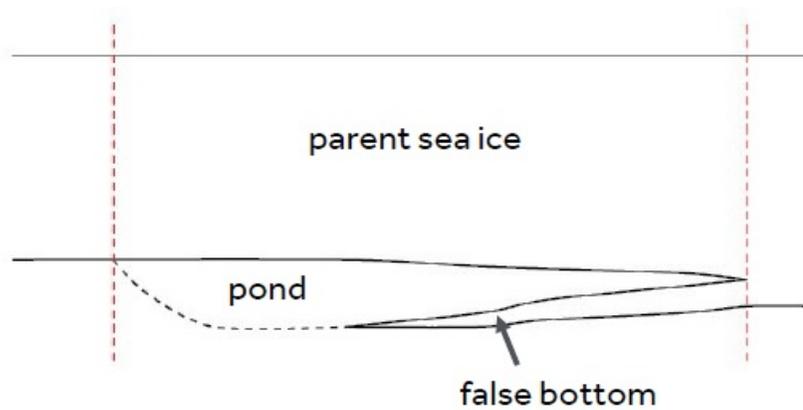
Figure 3.9: Schematic showing the freezing of a false bottom through an under-ice melt pond and joining with the parent sea ice above it.

Alternatively, the false bottom could completely ablate, in which case we assume that

the under-ice melt pond dissipates and that we are left with only the sea ice above (see Figure 3.10.)
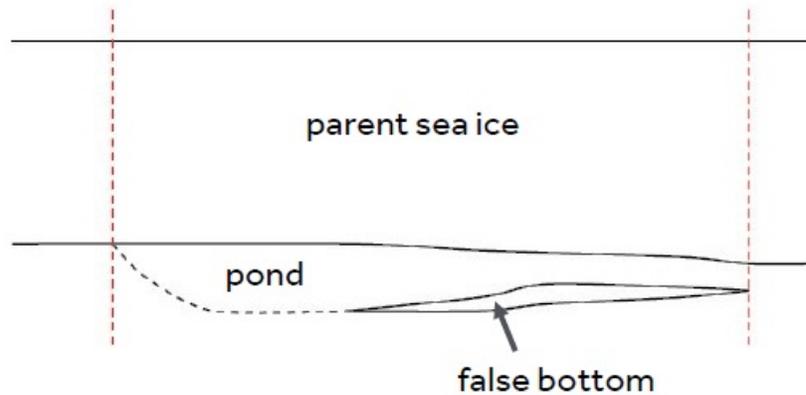
Figure 3.10: Schematic showing the freezing of a false bottom ablating and the parent sea ice progressing without an under-ice melt pond.

We translate these processes into two stages in our model. In 'Stage 1,' we evolve an under-ice melt pond and fully-formed false bottom beneath a parent slab of sea ice. Once the false bottom has either reached the base of the sea ice or ablated, we move to 'Stage 2,' in which the remaining slab of sea ice, ie. either the joined false bottom and parent sea ice or just the parent sea, ice is allowed to evolve for the rest of the 50 day period. The right-hand red dotted lines in Figures 3.9 and 3.10 co-incide with the start of Stage 2 for each case.

We note the thickness of the remaining slab of ice in the under-ice melt pond case, H_1', at the end of Stage 2. By comparing H_1 to H_1' at the end of the simulation period, we can measure how much ice is gained or lost vertically due to the presence of the under-ice melt pond.

We use the same cut-off thresholds for under-ice melt pond depth and false bottom thickness of 1 cm and 0.5 cm as criteria to move to Stage 2 under the assumption that the under-ice melt pond has frozen or the false bottom has ablated respectively. As the false bottom approaches the base of the sea ice, it is unlikely that the boundaries will line up exactly to eliminate the under-ice melt pond layer. The false bottom could intersect the sea ice in the timestep in which the under-ice melt pond has been completely frozen, resulting in a negative final under-ice melt pond depth. We therefore calculate

the thickness of the sea ice at the start of Stage 2 using

$$H_1'^{\text{initial}} = H_0^{\text{final}} + \max\left(H_{\text{pond}}^{\text{final}}, 0\right) + H_{\text{false bottom}}^{\text{final}} \tag{3.20}$$

in the case that the pond freezes, where H_{pond} is the under-ice melt pond depth, $H_{\text{false bottom}}$ is the false bottom thickness, and the superscripts initial and final correspond to the initial value in Stage 2 and the final value in Stage 1.

Both simulations are initialised with a parent sea ice of 80 cm, and the under-ice melt pond case includes an under-ice melt pond of initial thickness of 20 cm and initially salinity 5 psu, and a false bottom initially 2 cm thick. A constant oceanic forcing of 2 W m^{-2} is applied during the two simulations, corresponding to an assumption that the ocean salinity and temperature beneath the ice-pond system remain constant throughout the simulations. We use NCEP data as atmospheric forcings, as shown in Figure 3.2, and assume initially linear temperature profiles through the sea ice and the false bottom, running between the liquidus temperatures at their respective upper and lower interfaces.

3.4.1 Results

In the under-ice melt pond simulation, the false bottom migrated upwards through the sea ice and reached the base of the sea ice after 10.5 days. Figure 3.11 shows the depth of the under-ice melt pond, the boundary positions of the false bottom and the base of the sea ice, and the salinity of the under-ice melt pond over this period. The false bottom migrates upwards, freezing into the under-ice melt pond and releasing salt, during the first three days. At this point, the pond becomes more saline than the ocean, the false bottom begins to ablate at its upper interface, the sign of the temperature gradient within it is reversed, and it freezes at its lower interface. Due to the stronger negative temperature gradient, the sea ice is still able to grow into the under-ice melt pond, and eventually reaches the critical distance from the false bottom and the under-ice melt pond is assumed to have frozen. Due to the difference in solid fraction of the sea ice (0.8) and the false bottom (0.98), the pond freshens slightly while the false bottom is migrating downwards despite the decrease in pond depth during this period.

At the end of the 50 day period, the sea ice was 5.4 cm thicker in the under-ice melt
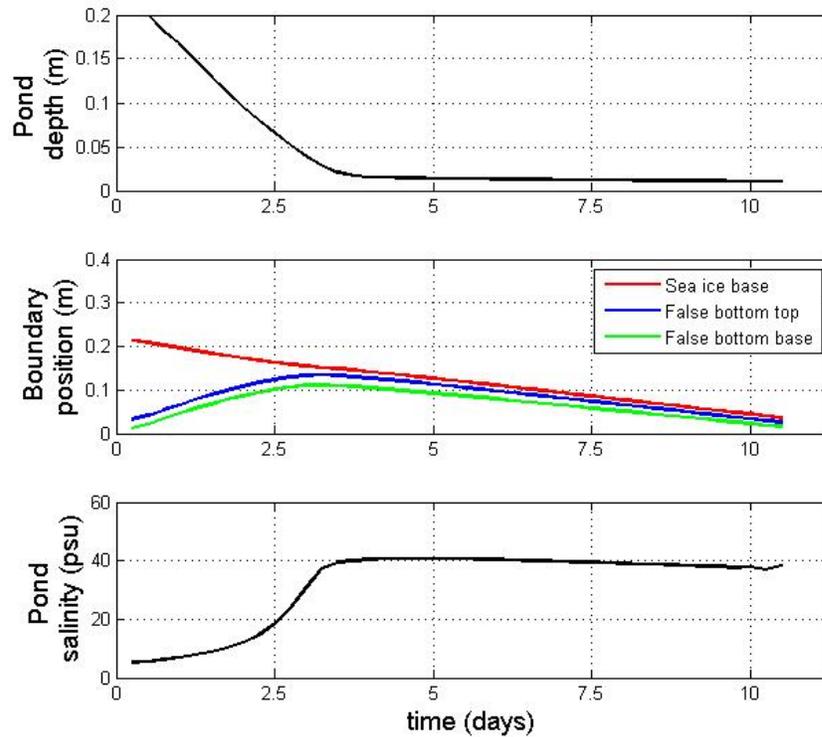
Figure 3.11: (Top) Under-ice melt pond depth (m). (Middle) Position of (red) the base of the sea ice, (blue) the top of the false bottom, and (green) the base of the false bottom (m). (Bottom) Under-ice melt pond salinity (psu).

pond case than in the slab case; the ice was 1.52 m thick at the end of the under-ice melt pond simulation , while it was just 1.46 m thick at the end of the slab sea ice simulation. This equates to an increase in ice thickness of 3.7% due to the under-ice melt pond relative to the bare-ice simulation.

This supports the theory that under-ice melt ponds lead to thicker sea ice, though under different conditions perhaps this is not the case. We have already seen that the false bottom could ablate rather than freeze through the entire pond. In the following section, we therefore test the model's sensitivity to variations in key parameters.

3.4.2 Implications for the Arctic sea ice

In this reference run, 5.4 cm extra ice is seen in the final vertical profile in the under-ice melt pond case than in the slab case, meaning that the ice is 3.7% thicker that it would

have been had there been no under-ice melt pond. Throughout our sensitivity studies, the gain in ice due to the under-ice melt pond equates to between 0.8 and 7.9% of the final thickness of the slab case, making the phenomena locally significant to the mass balance of the sea ice.

However, the overall impact that this has is determined by the prevalence of these pools of fresh water beneath the ice. A number of attempts have been made to estimate the fraction of the area of the base of the ice underlain by under-ice melt ponds. The most conservative estimates suggest that an area of about 5% of the total sea ice area, while the highest estimates suggest it could be closer to 40% [Eicken, 1994; Notz et al., 2003]. Certain regions with particularly favourable conditions for the formation of under-ice melt ponds have been observed to have over half of the basal area covered by the ponds [Hanson, 1965]. This area of rather high fraction was in the region of a research station, however, so drainage through the ice may have been enhanced by human activity.

A crude estimate can be made of the impact that under-ice melt ponds have on the Arctic sea ice using these pond fractions as a guideline. If we assume a constant sea ice area throughout our simulations and that the sea ice is horizontally homogenous, we can estimate the change in ice volume due to the presence of under-ice melt ponds, Δv (m^3), by calculating

$$\Delta v = A \cdot \Phi_u \cdot \Delta H,$$

where A is the sea ice area (m^2), Φ_u is the under-ice melt pond fraction, and ΔH (m) is the increase in sea ice thickness due to the presence of an under-ice melt pond under the given conditions. For the following calculations, we will use $A = 5 \times 10^{12}$ m^2, chosen by eye as a realistic value for the time of year from the September minimum extent in recent years [NSIDC]. We will use the suggested lower and upper bounds on Φ_u to be 0.05 and 0.4 as suggested above, ignoring the high suggestion of 50% as an upper value in order to be conservative in our estimate.

The lowest and highest amounts of ice growth seen in the sensitivity studies are 1.1 and 11.6 cm respectively. These values would set a range of between 2.75 and 232 km^3 of ice. This corresponds to between 0.3 and 3.2% of the final volume of ice in the slab case. The gain of ice in our reference case would equate to 13.5 to 108 km^3 of additional

ice across the Arctic. While these number are not huge and are unlikely to contribute significantly to the seasonal sea ice cover, the effects could be regionally important in areas of unusually high under-ice melt pond fraction. The seasonal marginal ice zone, for example, has a high surface melt pond fraction. Assuming that the under-ice melt pond fraction is proportional to the surface melt pond fraction, this region could also exhibit a high under-ice melt pond fraction, perhaps above the upper estimate of 40% of the sea ice cover.

3.5   Sensitivity studies

We have tested the model's sensitivity to several parameters' initial values: sea ice thickness, under-ice melt pond depth, false bottom thickness, under-ice melt pond salinity, and the oceanic heat flux. The effect of changing these parameters can be measured in differences in the final sea ice thickness, whether the false bottom freezes through the pond or ablates, and how long it takes for the false bottom to either reach the sea ice or thin to nothing.

Each simulation begins at the start of September, which equates to the start of the refreezing season, and is run for 50 days. Apart from when testing the model's sensitivity to that parameter, the simulations are initialised with parent sea ice of 80 cm; an under-ice melt pond thickness of 20 cm and salinity 5 psu; a false bottom 2 cm thick; and an oceanic forcing of 2 W m^{-2}, as in the reference case simulation.

Table 3.1 contains the minimum and maximum gains in ice thickness due to the under-ice melt ponds for each parameter that we tested. The range is shown in the right-hand column to allow for easy comparison between parameters. We can see that the model was most sensitive to the initial pond salinity, with the gain in ice varying by almost 10 cm depending on the value chosen. The ice gain was also heavily dependent on the initial parent sea ice thickness, which alters the rate of heat transfer away from the under-ice melt pond by steepening or shallowing the temperature gradient. The initial under-ice melt pond depth, initial false bottom thickness, and the oceanic forcing all altered the final gain in ice thickness relatively weakly, however, within the ranges tested.

Some interesting interactions between the pond and the sea ice are revealed in trends

Parameter	Tested range	Min ice growth (cm)	Max ice growth (cm)	Range (cm)
Initial parent sea ice thickness (m)	0.5 - 1.5	2.9	9.5	6.6
Initial pond depth (m)	0.1 - 0.5	0.0	1.1	1.1
Initial pond salinity (psu)	2 - 15	1.1	10.4	9.3
Initial false bottom thickness (cm)	1 - 5	3.5	6.7	3.2
Oceanic forcing (Wm^{-2})	-4 - 10	4.5	5.6	1.1

Table 3.1:: Parameters tested in our sensitivity studies, the ranges of values that we tested, and the associated minimum, maximum and range in ice growth compared to the slab case for each of them.

in the sensitivity study results, giving us an insight into how the under-ice melt pond affects the mass balance of the sea ice above it. We now present these results for each parameter and its effect on the amount of sea ice gained.
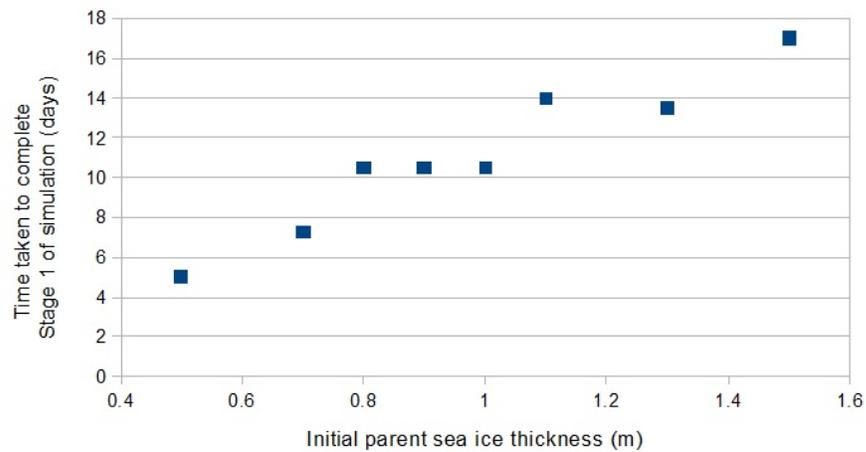
3.5.1   Parent sea ice thickness

Changing the thickness of the parent sea ice above an under-ice melt pond changes the temperature gradient at the upper interface of the pond; while the temperatures at the upper and lower boundary of the sea ice remain the same, the difference between them is divided over a thinner/thicker slab of sea ice. We tested ice thicknesses of 0.5 to 1.5 m at 20 cm intervals, and also the base run value of 0.8 m. We found that the thicker the sea ice, the greater the relative ice growth is seen due to the under-ice melt pond.

For all initial sea thicknesses the false bottom froze through the fresh water layer, though Figure 3.13 shows that for thicker sea ice values this process took longer, due to the smaller temperature gradient in the ice above the pond. In Figure 3.12, we see the gain in sea ice thickness due to the under-ice melt pond. In the slab case, thicker sea ice grows more slowly at its base due to the reduced temperature gradient, whereas in the under-ice melt pond case the base of the sea ice grows more rapidly in the less saline under-ice melt pond and the false bottom also freezes upwards through the fresh

water, adding to the sea ice thickness. The thicker the sea ice, the greater this difference between the two cases, since the under-ice melt pond water freezes in each case but the sea ice continues to grows more slowly with increased sea ice thickness.
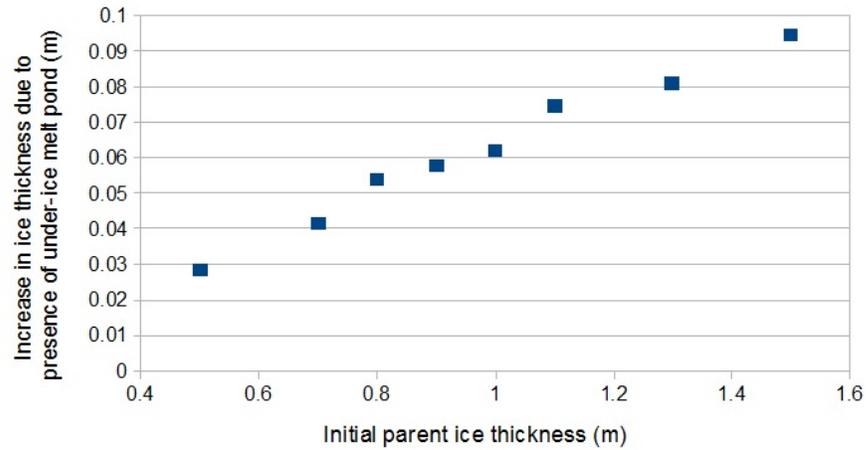

Figure 3.12: Increase in ice thickness at the end of a 50 day simulation due to the presence of an under-ice melt pond with overlaying sea ice of varying initial thickness.

Figure 3.13: Time taken for the under-ice melt pond to freeze with initial parent sea ice thickness.

Most of this growth is seen in the parent sea ice rather than coming from the false bottom; Figure 3.14 shows that the thickness of the false bottom layer at the end of Stage 1 decreases with initial parent sea ice thickness.
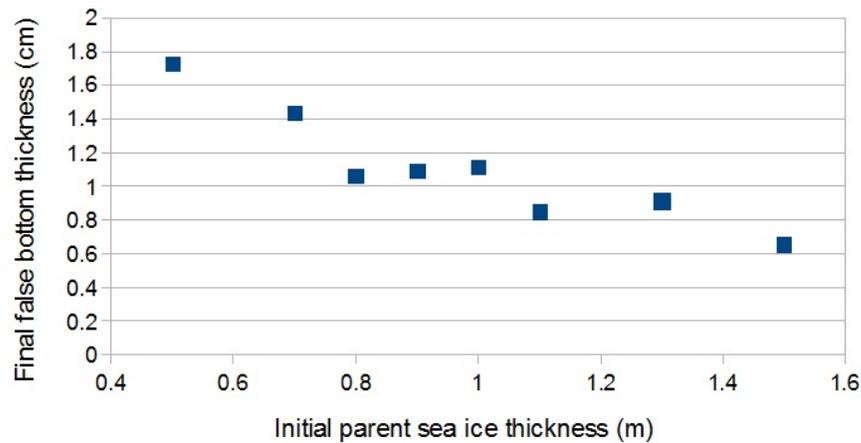
**Figure 3.14:** Final false bottom thickness with initial parent sea ice thickness.

3.5.2 Under-ice melt pond depth

We varied the initial under-ice melt pond depth between 10 and 50 cm at intervals of 10 cm. There is a clear change in the system's behaviour with increasing pond depth, whereby the under-ice melt pond freezes in cases of shallower under-ice melt pond depths, but the false bottom ablates before it is able to freeze through deeper ponds. We include an extra case with an initial pond depth of 25 cm to more accurately determine the switching point between the two regimes. The ice gain and final outcome (under-ice melt pond freezes/false bottom ablates) is shown in Figure 3.15, where we see that this switching point occurs at pond depths of 26-30 cm.

Regardless of whether the false bottom ablates or freezes through the under-ice melt pond, a deeper initial under-ice melt pond thickness means that more time is needed to complete this first stage of the simulation. Although deeper under-ice melt ponds correlate with false bottom ablation, the false bottom persists for longer than it takes to freeze a shallower pond, as shown in Figure 3.16.
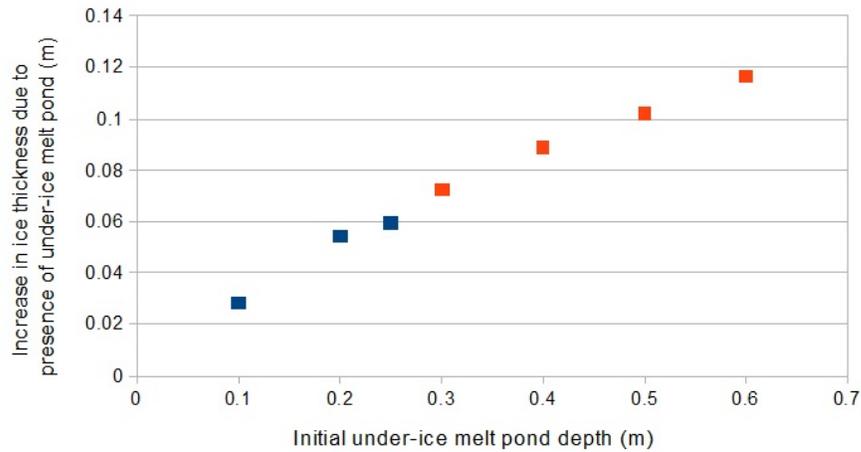
Figure 3.15: Increase in ice thickness at the end of a 50 day simulation due to the presence of an under-ice melt pond with varying initial depth.
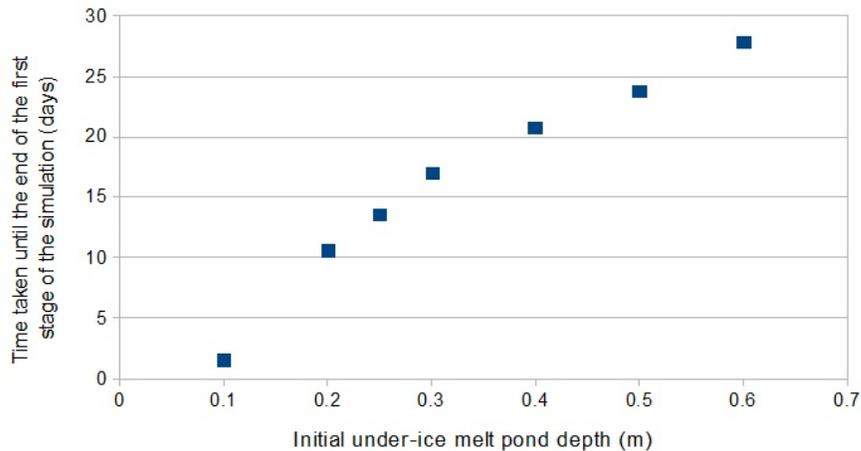

Figure 3.16: Time taken to complete the first stage of the simulation with initial under-ice melt pond depth.

In the cases where the under-ice melt pond freezes, deeper ponds result in more gain in sea ice thickness, since a larger amount of fresh water is being frozen. In the cases where the false bottom ablates, slightly less incoming radiation is able to reach the false bottom in the deeper pond case. Importantly, any salt released during freezing is also distributed into a larger amount of fresh water, so the under-ice melt pond remains fresher. The rate of growth of the upper interface of the false bottom is therefore higher

in the deeper pond cases. The false bottom therefore takes longer to ablate and the base of the sea ice grows into the fresh water layer during this time, and at a more rapid rate than it does into the saltier ocean water, and so more ice is gained by the deeper the pond.

3.5.3 False bottom thickness

The initial thickness of the underlying false bottom was varied between 1 and 5 cm, with gain in thicknesses shown in Figure 3.17. For a thin initial false bottom thickness of 1 cm, the false bottom ablated before it was able to freeze through the under-ice melt pond. However, for initial thicknesses of 2 cm or more the under-ice melt pond froze. Slightly more ice is gained when starting with a thicker false bottom, though this appears to be more to do with the extra ice introduced by the false bottom in the first place rather than its effect on the pond's evolution.
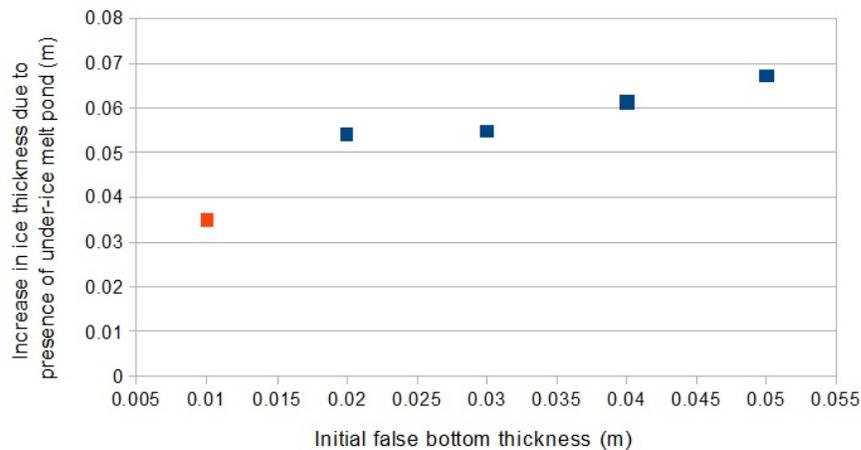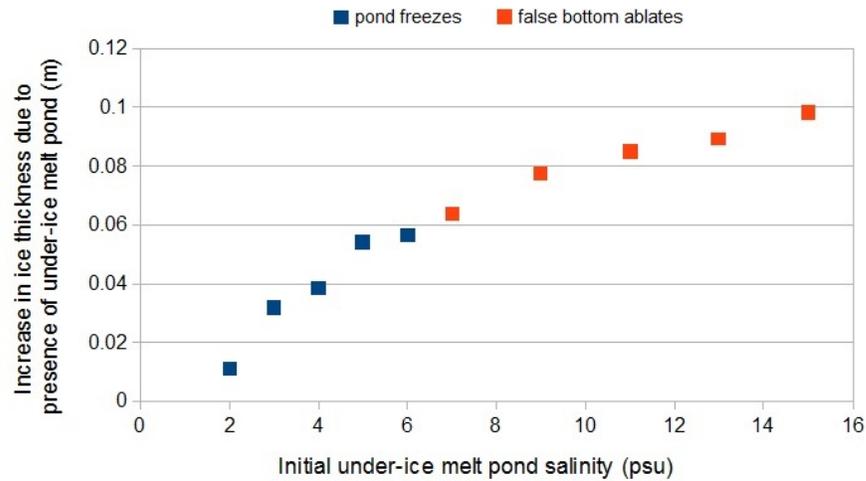

Figure 3.17: Increase in ice thickness at the end of a 50 day simulation due to the presence of an under-ice melt pond with underlying false bottom of varying initial thickness.

3.5.4 Pond salinity

We next varied the initial under-ice melt pond salinity between 2 and 15 psu. In Figure 3.18, we see that there are two distinct regimes in the outcomes of the tested values. For low initial under-ice melt pond salinities (6 psu or less), the under-ice melt pond freezes,

whereas the false bottom ablates for initial salinities of 7 psu up. Interestingly, the gain in ice thickness in the under-ice melt pond case relative to the slab case increases with initial pond salinity. We now investigate the reason for this.

Figure 3.18: Increase in ice thickness at the end of a 50 day simulation due to the presence of an under-ice melt pond with different initial salinities.

Figure 3.19 shows the time taken to reach the end of Stage 1 (either for the under-ice melt pond to freeze or for the false bottom to ablate). In the low initial salinity regime, in which the under-ice melt pond freezes, the pond persists for longer the higher the salinity; it takes just 3 days to freeze the 2 psu pond but 13 days to freeze the 6 psu pond. This is because the growth rate of the ice is lower due to the higher salinity, and so the pond takes longer to freeze. In the second regime, there is little variation in time taken for the false bottom to ablate. This takes around 14 days for all high-salinity tested values, with a slight negative trend in time taken for the highest values. The reason for this can be seen in our previous case study in Section 3.3.2. For a high initial pond salinity, the false bottom initially grew, releasing salt into the pond until it became too saline for further growth of the false bottom into the pond. In fact, it became more saline than the ocean below, and so the difference between the conductive and oceanic heat fluxes reversed sign and it began to migrate downwards instead, ablating at its upper interface and freezing into the ocean. This leads to Stage 1 of the simulation taking longer than in the low salinity cases in which the false bottom simply freezes through the fresh water layer, and so the sea ice is insulated from below for longer. Due to the

temperature gradient within the sea ice, its base continues to grow into the under-ice melt pond throughout this process, so the positive trend in ice thickness with initial pond salinity remains positive for these high initial pond salinity cases. Once the false bottom begins migrating downwards, fresh water is again released into the under-ice melt pond and its salinity decreases, so we continue to see more ice growth associated with higher initial under-ice melt pond salinities up until at least 15 psu.
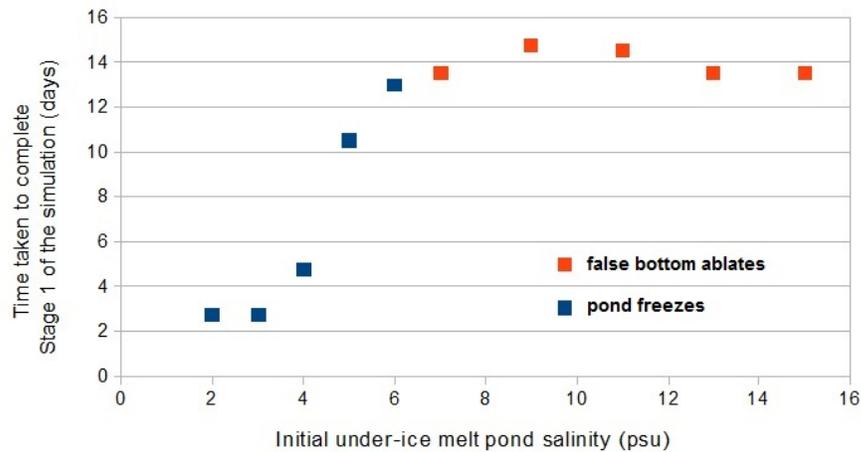

Figure 3.19: Time taken for the completion of Stage 1 of the simulation with initial under-ice melt pond salinity.
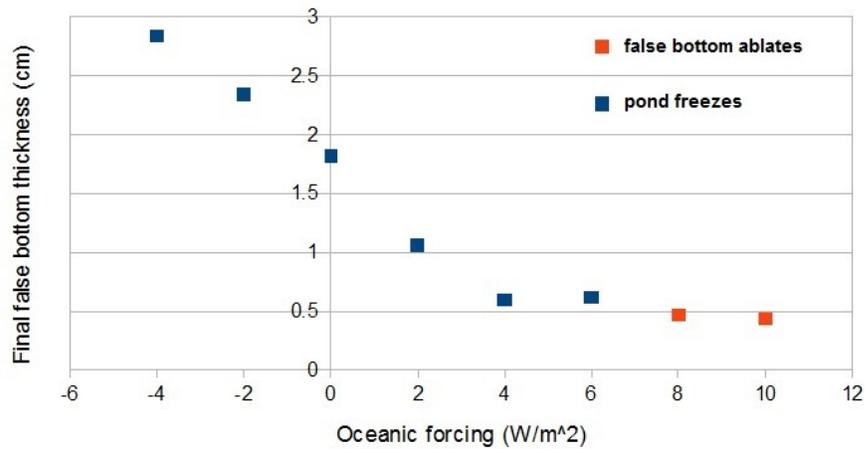
3.5.5 Oceanic forcing

Little trend was seen in the gain in ice thickness with oceanic forcing, as shown in Figure 3.20. For all values tested between -4 and 10 W m^{-2}, around 5 cm of ice was gained due to the presence of the under-ice melt pond. However, for stronger forcings of 8 - 10 W m^{-2} the false bottom ablated before the pond froze.

The false bottom thicknesses at the end of Stage 1 are plotted in Figure 3.21 and, unlike the gain in ice thickness, do show a clear negative trend with increasing oceanic forcing. This illustrates the insulative effect of the false bottoms: instead of directly affecting the base of the sea ice, the false bottom insulates the sea ice above from the sea. There is therefore little trend in the gain in ice thickness with oceanic forcing, despite the slower migration rate in the freezing cases.
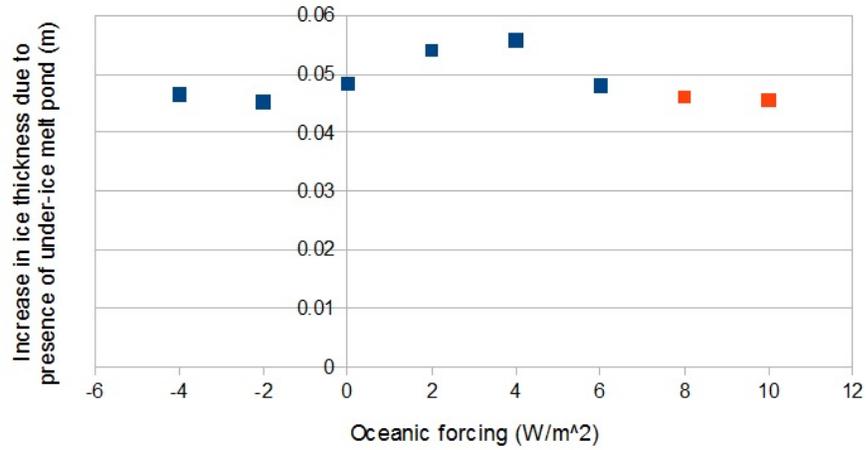
Figure 3.20: Increase in ice thickness at the end of a 50 day simulation due to the presence of an under-ice melt pond with different oceanic forcing strengths.

Figure 3.21: Final false bottom thickness with different oceanic forcing strengths.

3.6   Conclusion

We developed a one-dimensional thermodynamic model of under-ice melt ponds sitting below sea ice with a fully formed false bottom. We calculate the temperature and salinity of the under-ice melt pond using diffusion equations, together with brine rejection from the interfaces, and treat the sea ice and false bottom as mushy layers, a combination of

ice and brine. We use NCEP atmospheric forcings in the surface energy balance of the sea ice and prescribe a far-field temperature and salinity within the ocean, along with a heat flux between the ice and the water. Stefan conditions are used to calculate the boundary positions.

Using this model, we were able to identify two typical evolutions of false bottoms. Firstly, the false bottom can freeze through the entire fresh water layer or, secondly, it can ablate or melt before it reaches the base of the sea ice. We were also able to reproduce the evolution of an observed false bottom to a good approximation, capturing the overall trend in its thickness, migration rate, and the pond depth as well. Sensitivity studies showed that the initial pond salinity and initial sea ice thickness have a large effect on the outcome of the model and on the amount of ice gained due to the pond.

Across the Arctic as a whole, we estimate that up to 232 km^3 of sea ice could be produced from the freezing of under-ice melt ponds. It appears that the impact of under-ice melt ponds on the mass balance of the sea ice as a whole could be fairly small, but it has a non-negligible local effect vertically and could be significant in regions of high under-ice melt pond fraction.

3.7   Discussion

Our model appears to be the most complete treatment of false bottom evolution to date. Whereas others have simulated false bottoms in isolation, we have included sea ice and under-ice melt pond layers, allowing us to investigate the limiting effects of pond salinity and to determine the final outcome of the false bottom's development, as well as to assess the impact of the phenomenon on the ice above it.

Under-ice melt ponds have a significant impact on the mass-balance of the sea ice above them and, in regions of high under-ice melt pond fraction, it is important to include them within the treatment of sea ice in climate models. In such regions, a 3.2% increase in ice volume or greater could be seen. This would have knock-on effects on the ice albedo and longevity, as well as the amount of radiation reaching the ocean below.

We made a number of simplifying assumptions in order to estimate the impact on the volume of the Arctic sea ice, which are clearly unrealistic. The Arctic sea ice in reality is far from horizontally homogenous, for example, so we would expect a wide range of

ice thicknesses, under-ice melt pond depths and salinities, and false bottom thicknesses to be present across the region. However, this gives us a rough upper and lower bound on the impact that the fresh water pools have on the sea ice volume.

As the Arctic warms, we expect to see more surface melt and more porous ice, so the prevalence of under-ice melt ponds could increase significantly. They could, therefore, be of more importance to the sea ice's mass balance in the future. As well as an increase in Arctic average temperatures leading to more surface melt, we expect to see a lower ratio of multi-year ice to first year ice [Comiso, 2012]. First year ice is sea ice within twelve months old, as opposed to multi-year ice, which is ice that has survived at least one summer melting period. First year ice is typically smoother than multi-year ice, and so surface melt leads to a higher pond fraction due to its topography [Hanesiak et al., 2001]. If these widespread surface ponds are able to drain through the ice and form under-ice melt ponds, this could increase the under-ice melt pond fraction (though perhaps decrease their depth.)

In the model itself, it would be more realistic to include a surface melt pond on the sea ice above the under-ice melt pond, since observations suggest that they commonly persist on the surface well into the under-ice melt ponds' life cycle. However, this would have complicated the model both in terms of computational cost and in isolating the impact of under-ice melt ponds on the mass balance of the sea ice. We see in our comparison with an observed pond that our model is able to adequately reproduce the evolution of a false bottom simply by changing the surface temperature and albedo of the sea ice to account for a surface pond when necessary.

We assigned a constant heat flux from the ocean to the ice in each simulation, but in reality this value would vary seasonally. By varying this parameter, we saw that it had a large effect on the length of time the false bottom persisted, and using different heat fluxes could control whether the false bottom freezes through the under-ice melt pond or ablates.

Changes to the ice cover also affect key properties of the oceanic mixed layer beneath the ice. Ablation releases fresh water into the ocean, making it less saline and shallowing the mixed layer. Conversely, basal ice growth adds salt rejected from the ice matrix during the freezing process, increasing the mixed layer salinity and depth. Ice thickness controls the amount of radiation reaching the mixing layer and heating it, and ice cover

effects precipitation and the transfer of kinetic energy to the ocean. In turn, mixed layer temperature and freezing point, and hence its salinity, determine the heat flux to the base of the ice, affecting basal growth or ablation rates.

It would therefore be useful to have a more accurate description of the ice-ocean interactions. Coupling the model presented in this chapter to a model of the oceanic mixed layer could enable us to determine the effect that the alteration of basal ablation due to under-ice melt ponds has on the mixed layer properties, and also any secondary effects that this has on the mass balance of the sea ice.

Chapter 4

Under-ice melt ponds and the oceanic mixed layer

4.1 Introduction

Petty et al. [2013] developed a coupled sea ice-ocean mixed layer model to investigate the cause of the bimodal distribution of water mass temperature in the Antarctic continental shelf seas. They set out to determine the role that various processes and forcings play in the difference in temperature between the Amundsen and Bellinghausen Seas and the Weddell and Ross Seas, which are several Celsius cooler than the prior. They were able to use this model to reproduce mixed layer behaviour typical to the region and to identify the atmospheric forcings as the reason for the difference in mixed layer properties and evolution by switching said forcings typical to the two regions.

Since the model of Petty et al. [2013] has been successfully used to model sea ice-mixed layer interaction and is not as computationally demanding as other, more complex mixed-layer models, we will adapt it here for use with our under-ice melt pond model. In this chapter, we will investigate the impact of under-ice melt ponds on key properties of the oceanic mixed layer, due to their impact on the basal ablation of the sea ice.

4.2 Ocean mixed layer model description

4.2.1 Coupling with the under-ice melt pond model

In our model, the oceanic mixed layer sits below either a slab of sea ice, sea ice with an under-ice melt pond, or sea ice with an under-ice melt pond and false bottom. The sea ice slab or under-ice melt pond and false bottom processes are simulated using the model presented in Chapter 3, with the exception of their interactions with the ocean. In

Chapter 3, the only interaction between the system and the ocean was via a prescribed heat flux from the ocean into the ice and through a constant ocean salinity, determining the liquidus temperature at the interface, whereas now we have two-way interactions via several mechanisms:-

- firstly, the mixed layer salinity now determines the liquidus temperature at the ice-ocean boundary, allowing the basal ablation rate to respond to seasonal freshening or salinisation of the ocean as the ice melts or freezes;

- secondly, any surface melting or basal ablation is assumed to drain into the mixed layer, freshening it, and basal growth causes salt to be rejected from the ice matrix into the mixed layer, making it saltier; and

- finally, the heat flux upwards from the mixed layer to the surface, F_O, is directly calculated, rather than set equal to a prescribed constant.

4.2.2   Mixed layer

The mixed layer entrains or detrains water depending on inputs from surface winds, precipitation, radiative heating, salt and fresh water fluxes from the sea ice, and the density of any water that it entrains. Deepening the mixed layer requires work to be done via one of these mechanisms in order to change the potential energy. We use the energy balance model of Kraus and Turner [1967] to model the evolution of the mixed layer beneath the sea ice. The model was first adapted for use with sea ice by Petty et al. [2013], which we draw from heavily.

We set a maximum depth after which point the mixed layer cannot deepen. We also set a minimum depth, chosen to be 5 m, at which point it cannot shallow further. Its change in depth, h_m, is calculated using

$$\frac{\mathrm{d}h_m}{\mathrm{d}t} = \frac{1}{h_m b + c_m^2}(c_1 P_{\text{wind}} + h_m c_2 (P_{\text{temp}} + P_{\text{salt}} + P_{\text{solar}})). \tag{4.1}$$

The coefficient

$$\frac{1}{h_m b + c_m^2}$$

accounts for the power needed to entrain water from below into the mixed layer due to differences in density of the mixed layer and deeper ocean waters. c_m is the unsteadi-

ness coefficient, representing the loss of energy through friction due to turbulence of the mixed layer, c_1 is the maximum wind stirring in the mixed layer, and c_2 is the power dissipation due to convective mixing. If the water below the mixed layer has temperature T_B and salinity S_B, and the mixed layer has temperature T_m and salinity S_m, then the difference in buoyancy between the mixed layer and the deeper ocean is given by

$$
b = \begin{cases} g\alpha(T_m - T_B) - g\beta(S_m - S_B) & \text{if } h_m < h_{\max} \\ 0 & \text{if } h_m = h_{\max}, \end{cases}
\tag{4.2}
$$

where g is the acceleration due to gravity, α is the thermal expansion coefficient, and β is the saline contraction coefficient. P_{wind} is the rate of input of turbulent kinetic energy into the mixed layer via surface wind friction. For a depth of power dissipation of 10 m, this is given by

$$
P_{\text{wind}} = e^{-\frac{h_m}{10}} u_*^3,
\tag{4.3}
$$

where u_* is the friction velocity given by

$$
u_* = \sqrt{A_i c_{d_i} \frac{\rho_a}{\rho_w} u_a^2 + (1 - A_i) c_{d_l} \frac{\rho_a}{\rho_w} u_a^2}.
\tag{4.4}
$$

Here, A_i is the fraction of ocean covered by sea ice, c_{d_i} is the turbulent transfer coefficient over ice, c_{d_l} is the turbulent transfer coefficient over water, ρ_a is the density of air, ρ_w is the density of the water, and u_a is the wind speed. The heat fluxes from mixed layer into the base of the sea ice and open-lead surface layer are given by

$$
F_O = \rho_w c_w c_h u_*^i (T_m - T_f)
\tag{4.5}
$$

and

$$
F_l = \rho_w c_w u_*^l (T_m - T_l),
\tag{4.6}
$$

where c_w is the specific heat capacity of water, T_f is the freezing temperature of the mixed layer water, and T_l is the temperature of the lead surface water. c_h is the heat transfer coefficient between a solid and a fluid, equivalent to the Stanton number, and does not apply for heat transfer between fluids (such as is the case in Equation 4.6.) u_*^i is the friction velocity between the sea ice and the ocean, u_*^l is the friction velocity between the

open lead water and the ocean. These are defined as

$$u_*^{i,l} = \left(\sqrt{c_{d_{i,l}} \frac{\rho_a}{\rho_w}} \right) u_a. \tag{4.7}$$

F_O and F_l can be used to calculate the power into the mixed layer due to heat fluxes via

$$P_{\text{temp}} = \frac{g\alpha}{\rho_w c_w} \left((1 - A_i) F_l + A_i F_O \right). \tag{4.8}$$

We find the power input into the mixed layer from salt and fresh water fluxes using

$$P_{\text{salt}} = -g\beta \left(A_i (F_{\text{base}} - F_{\text{surf}}) + (1 - A_i) F_{\text{precip}} + F_{\text{area}} \right), \tag{4.9}$$

where

$$F_{\text{base}} = -\frac{\rho_i}{\rho_w} (S_m - S_i) \frac{\mathrm{d}h_i}{\mathrm{d}t} \bigg|_{\text{base}}, \tag{4.10}$$

$$F_{\text{precip}} = S_m \psi_{\text{net}}, \tag{4.11}$$

$$F_{\text{area}} = -\frac{\rho_i}{\rho_w} (S_m - S_i) h_i \frac{\mathrm{d}A_i}{\mathrm{d}t}, \tag{4.12}$$

and

$$F_{\text{surf}} = \frac{\rho_i}{\rho_w} (S_m - S_i) \frac{\mathrm{d}h_i}{\mathrm{d}t} \bigg|_{\text{surface}}. \tag{4.13}$$

ρ_i is the density of the sea ice, S_i is its bulk salinity, and ψ_{net} is the precipitation minus any evaporation. Finally, radiative power input is given by

$$P_{\text{solar}} = -\frac{g\alpha}{\rho_w c_w} F_{\text{solar}}, \tag{4.14}$$

with

$$F_{\text{solar}} = F_{\text{SW}} \left(A_i (1 - \alpha_i) \iota_i (1 - e^{-\kappa_w h_m}) e^{-\kappa_i h_i} + (1 - A_i)(1 - \alpha_w) \iota_w (1 - e^{-\kappa_w h_m}) \right). \tag{4.15}$$

F_{SW} is the incoming shortwave radiation, α_i is the albedo of the sea ice, ι_i is the fraction of shortwave radiation that penetrates the surface of the ice, κ_i is the extinction coefficient of shortwave radiation in ice, α_w is the albedo of the water, ι_w is the fraction of shortwave radiation that penetrates the surface of the open water, κ_w is the extinction coefficient of shortwave radiation in water, and h_i is the thickness of the sea ice.

Changes to the mixed layer's temperature, T_m, and salinity, S_m, are given by

$$\frac{\mathrm{d}T_m}{\mathrm{d}t} = \begin{cases} \frac{1}{h_m}\left(F_{\text{solar}} - \frac{1}{g\alpha}P_{\text{temp}} - \frac{\mathrm{d}h_m}{\mathrm{d}t}(T_m - T_B)\right) & \text{for } \frac{\mathrm{d}h_m}{\mathrm{d}t} > 0 \\ \frac{1}{h_m}\left(F_{\text{solar}} - \frac{1}{g\alpha}P_{\text{temp}}\right) & \text{for } \frac{\mathrm{d}h_m}{\mathrm{d}t} \leq 0 \end{cases} \tag{4.16}$$

and

$$\frac{\mathrm{d}S_m}{\mathrm{d}t} = \begin{cases} \frac{1}{h_m}\left(\frac{1}{g\beta}P_{\text{salt}} - \frac{\mathrm{d}h_m}{\mathrm{d}t}(S_m - S_B)\right) & \text{for } \frac{\mathrm{d}h_m}{\mathrm{d}t} > 0 \\ \frac{1}{h_m}\frac{1}{g\beta}P_{\text{salt}} & \text{for } \frac{\mathrm{d}h_m}{\mathrm{d}t} \leq 0 \end{cases} \tag{4.17}$$

respectively.

4.2.3 Sea ice area evolution

While we still assume that the sea ice is horizontally homogenous, we now introduce a sea ice area fraction, $0 < A_i < 1$, which represents the fraction of the given area that is covered by sea ice. In the fraction that is not covered by ice, we allow the mixed layer to interact with a shallow surface layer of water instead. Assuming that the temperature of this surface layer of water is T_l and the mixed layer has freezing temperature T_f, then the change in ice fraction is given by

$$\frac{\mathrm{d}A_i}{\mathrm{d}t} = \begin{cases} \frac{H_f(1-A_i)}{\mathcal{L}\rho_i h_i} & \text{if } A_i < 1 \text{ and } T_l < T_f \\ \frac{H_f(1-R_B)(1-A_i)}{\mathcal{L}\rho_i h_i} & \text{if } A_i > 0 \text{ and } T_l \geq T_f \\ 0 & \text{otherwise} \end{cases} \tag{4.18}$$

after Petty et al. [2013]. The potential heat flux, H_f, is the difference between the heat flux from the mixed layer into the surface/lead water and the heat flux due to the latent heat released/absorbed during freezing/melting of the mixed layer (i.e. the remaining heat available to change the sea ice area), calculated using

$$H_f = \rho_w c_w c_h u_*^l(T_m - T_l) - \rho_w c_w c_h u_*^l(T_m - T_f) = \rho_w c_w c_h u_*^l(T_f - T_l), \tag{4.19}$$

and R_B is the fraction of the heat flux from the ocean that is put towards basal melting, as opposed to lateral melting. For example, $R_B = 1$ implies that all melting is basal. It is taken to be 0.4 after [Petty et al., 2013]. Similarly, the basal melting due to the ocean heat flux is scaled with R_B.

4.2.4 Full model

Figure 4.1 illustrates the model set up and simulation structure outlined in this subsection. We solve Equations 3.1 to 3.16 from Chapter 3 to model the temperature within the sea ice and the change in boundary positions between the ice and water layers. We use Equations 4.1 to 4.19 to find the oceanic mixed layer temperature, salinity, and depth.

The model requires input in the form of precipitation, reference level air temperature and specific humidity, and incoming longwave and shortwave radiation. Ambient temperature and salinity profiles within the ocean are needed, as well as initial states of the ice and ocean, namely the initial thickness of the sea ice and the initial depth, salinity, and temperature of the mixed layer.

4.2.5 Simulation structure and transitions

Rather than initialise the model with an under-ice melt pond, we now begin with a bare slab of sea ice and model the formation of the fresh water layer and the false bottom. This means that the under-ice melt pond model has three distinct stages.

4.2.5.1 Stage 1: Under-ice melt pond and false bottom formation

To begin with, we use our coupled sea ice-mixed layer model to evolve a slab of sea ice forward in time. In this stage, we assume that a fraction of any water from surface melting collects beneath the sea ice and does not mix into the ocean, rather than draining directly into the mixed layer. 33. Depending on how quiescent the ocean is and the presence or lack of any physical shelter around the fresh water, the assumption that no mixing between the pond and ocean takes place may or may not be realistic. However, we know from observations that false bottoms do exist, and almost always sit below fresh water containing very little contamination from the ocean. Given our aim is to simulate such scenarios, the assumption that no mixing takes place with the ocean is reasonable. Once an under-ice melt pond has formed beneath the sea ice and has met certain conditions, e.g. has been present for a minimum amount of days, then we assume that a false bottom has formed at the interface between the interface between the pond and the ocean and we move to Stage 2. If these conditions are never met, then we assume that no pond forms and run the year with the slab model only.
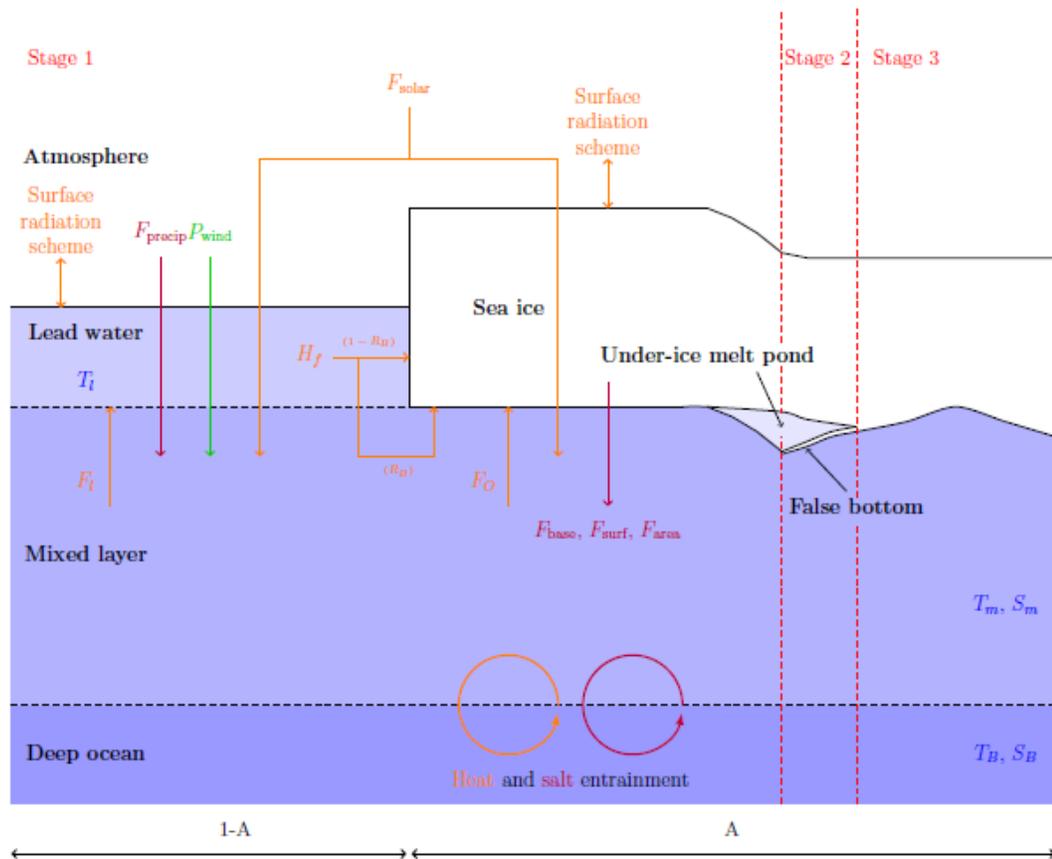
Figure 4.1: A schematic of the model setup and the three stages of the under-ice melt pond simulations carried out in this chapter. Slab simulations do not allow under-ice melt ponds to form, and are therefore equivalent to Stage 3 for the entire simulation. Heat and salt forcings are labelled in orange and purple respectively. Wind mixing is shown in green.

In the slab model, the slab of sea ice initialised at the start of Stage 1 is allowed to evolve for a year, with all surface melt water draining directly into the mixed layer rather than accumulating beneath the ice; no under-ice melt pond is allowed to form. Precipitation over the open-water fraction enters the mixed layer, as does any basal and lateral melt.

4.2.5.2   Stage 2: Evolution of an under-ice melt pond with a false bottom

In Stage 2, we switch to our under-ice melt pond-mixed layer model and again allow all surface melt to drain into the mixed layer. To begin with, the sea ice has the same thickness as it did at the end of Stage 1, the initial under-ice melt pond depth is also taken

from the end of Stage 1, and the false bottom is assumed to have an initial thickness of 2 cm and a solid fraction of 0.98, as determined in Chapter 1. A lower solid fraction would slightly reduce the amount of fresh water released from ablation of a set volume of the false bottom, but would cause the false bottom to ablate more rapidly. It is unlikely to have a notable impact on the qualitative results of our study.

The system is allowed to evolve until the false bottom has frozen through the under-ice melt pond or ablated. If it ablates, we deposit the fresh water from the under-ice melt pond into the mixed layer, freshening it.

4.2.5.3   Stage 3: Sea ice evolution after the under-ice melt pond disappears

Finally, we take the remaining slab of sea ice and allow it to evolve as a slab, as we did once the false bottom had completed its life-cycle in Chapter 2, with surface melt draining into the ocean until the end of the year, after which we return to Stage 1 again.

The structure of the model is shown in more detail in Appendix A.

4.2.5.4   Under-ice melt pond formation

While the fresh melt water is collecting beneath the sea ice in Stage 1, the sea ice must grow into this under-ice melt pond instead of the ocean. This has the effect of changing the liquidus temperature and the sea ice-water interface and any basal ice growth now subtracts from the volume of the pond. In this case, the calculation of the amount of salt added to the under-ice melt pond from basal growth must be adapted to

$$F_{\text{base}} = -\frac{\rho_i}{\rho_w}(S_{\text{pond}} - S_i)\frac{\mathrm{d}h_i}{\mathrm{d}t}\bigg|_{\text{base}} \tag{4.20}$$

instead of Equation 4.10, due to the pond having a different salinity to the ocean.

4.2.5.5   Surface melt

We chose not to model surface melt ponds explicitly for simplicity. To begin with, we neglect their presence altogether, and later we add a parameterisation of their impact on the albedo, anticipating that it will enhance the amount of surface melt and reduce basal growth into the under-ice melt ponds, allowing them to reach the critical depth to move

on to Stage 2 faster. This approach captures their leading-order impact on the ice while adding little computational cost.

4.2.5.6   Deep ocean properties

Temperature and salinity profiles are initially equal to the prescribed ambient profiles, and are updated as the mixed layer entrains or detrains deeper ocean water. If the mixed layer deepens, the temperature and salinity of the entrained ocean depths are updated to be equal to the new mixed layer temperature and salinity. If the mixed layer shallows, the ocean depths that it leaves gradually revert back to their original ambient values over the course of a chosen relaxation period. T_B and S_B, used in Equations 4.2, 4.16 and 4.17, are taken from these updated profiles in the next time step.

4.3   Numerical simulation

4.3.1   Numerical method of solution

As in Chapter 3, we initialise the sea ice with linear temperature profiles and use Matlab's built in `pdepe` routine to find the temperature profile within each layer in the subsequent timesteps. Again, the salinity of the under-ice melt pond is updated via a finite difference scheme for the change due to ice growth/ablation according to 3.14. We choose the coefficent $\Gamma = 0.0514$ in the liquidus relation, as was used in Taylor and Feltham [2004]. The mixed layer is assigned an initial salinity of 33 psu, an initial temperature of -1.8 C, and an initial depth of 30 m. We choose a relaxation period of 90 days, over which the deeper ocean grid cells revert back to their ambient values, after Petty et al. [2014], who used a relaxation period of 3 months. We give linear ambient profiles for the ocean temperature and salinity and use ERA-Interim data to provide atmospheric forcings. These are shown in detail later in the chapter. We set the maximum mixed layer depth to be 100 m, which proves sufficient to capture both the seasonal patterns in the mixed layer properties and the impact of the thermodynamic changes caused by the under-ice melt pond.

We use a courser spatial grid of 30 grid cells in the parent sea ice, 20 in the under-ice melt pond, and 10 in the false bottom in this chapter in order to reduce the computational

cost when carrying out coupled simulations for multiple years, and similarly switch to a timestep of one day. The numerical solutions still capture the evolution of the sea ice, under-ice melt pond, and false bottom well and produce sufficiently smooth solutions for our analysis. We look at a fixed domain of 100 m of ocean with a discrete grid of 100 levels, i.e. a metre a grid cell.

We use a forward finite difference scheme to calculate the new mixed layer depth, temperature, and salinity at each timestep, using any surface melt and the basal growth/ablation from the sea ice model. Similarly, the mixed temperature and salinity are then used to determine the oceanic forcing and the liquidus temperature at the base of the sea ice model's domain in the next time step.

During Stage 1, we set a certain fraction of surface melt water drainage to contribute to under-ice melt water formation rather than to mixed layer freshening. We assume that 80% contributes to the gathering fresh water water layer and 20% drains into the mixed layer, under the assumption that if under-ice melt ponds form then it must be a location of little mixing of fresh-water into the ocean below, but that some mechanisms (such as lateral run-off of melt water from the floe) could still deliver melt water to the mixed layer. Given the lack of observations of the under-ice melt pond formation, we cannot know whether this is a realistic ratio or not, but it gives reasonable results, allowing under-ice melt ponds to form and the mixed layer to maintain realistic salinity and depth during the drainage period. Reducing the percentage stored in the fresh water layer would delay the onset of the formation of the false bottom, and could prevent the pond from reaching the criteria altogether if set too low. Once the under-ice melt pond has reached a prescribed critical depth of 10 cm and has been present for at least 12 days, then we assume that the false bottom has formed. We then move to Stage 2. When determining whether the pond has frozen or the false bottom has ablated in Stage 2, we use the same cut-off values of 1 cm for the under-ice melt pond and 0.5 cm for the false bottom as in Chapter 3, and similarly initialise the thickness of the slab of sea ice in Stage 3 with Equation 3.20.

If the mixed layer rapidly shallows, for example at the start of the summer melt season, then the temperature and salinity profile of the ocean directly below the mixed layer will retain similar properties to the mixed layer for some time before it relaxes back to ambient values, meaning it will have a similar buoyancy to the mixed layer.

When calculating the new mixed layer depth in the next time step, this could lead to an unrealistic jump in the mixed layer depth were we to use the properties of the ocean in the grid cell directly below the mixed layer when solving Equation 4.2. We therefore employ a predictor-corrector approach in calculating the mixed layer depth. We first 'predict' the ocean properties using the properties of the ocean grid cell directly below the mixed layer. If this results in a change in mixed layer depth greater than 1 m, then we 'correct' by redoing the calculation with the ocean grid cell 10 m below the mixed layer.
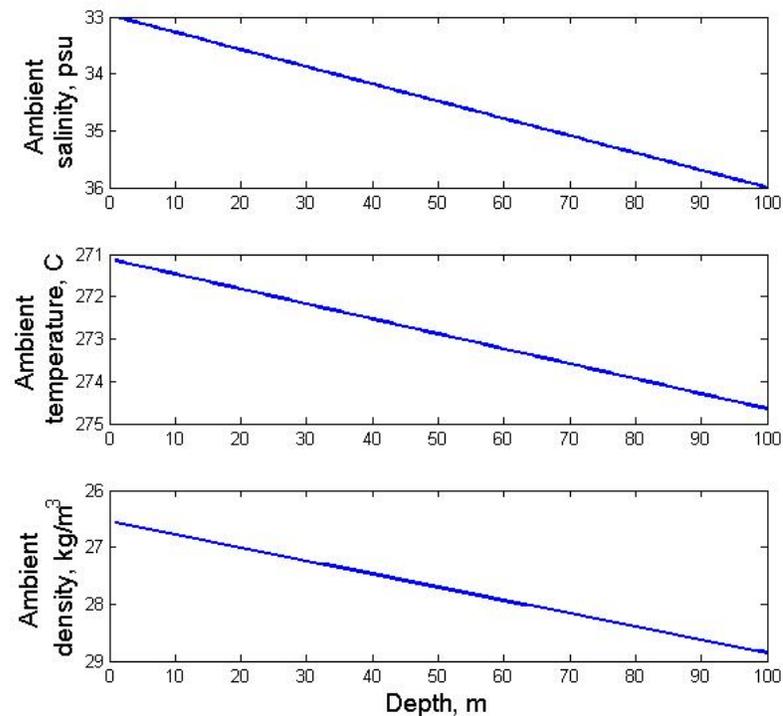
Figure 4.2: Initial ambient salinity and temperature profiles, and the corresponding density profile, for the ocean water of depth between 0 and 100 m.

4.3.2 Annual cycle

Firstly, we look at one year of evolution of the under-ice melt pond system and the bare slab system. We start both scenarios with the same initial conditions, namely a slab of ice 2.5 m thick at 75°N 210°E at the beginning of January. The ambient profiles for tem-

perature and salinity, and the corresponding density profile, in the ocean are shown in Figure 4.2. The salinity increases with depth from 33 psu at the surface to 36 psu at 100 m deep, while the temperature increases from -2 °C at the surface to 1.5 °C at 100 m deep. This yields an ambient density profile in the ocean that increases linearly with depth. There is typically a kink in the temperature and salinity profiles of the Arctic ocean, with the temperature and salinity gradually decreasing with depth after a maximum in the range of 50-150 m deep [Steele and Boyd, 1998; Uttal et al., 2002]. We chose the simplifying assumption of linear temperature and salinity profiles to make our results easier to interpret and to allow us to more readily change the strength of the ambient density profile, to which we later test the sensitivity of the model. The maximum and minimum values of our ambient profiles were chosen to be consistent with typical profiles from the Scripps Institution of Oceanography.
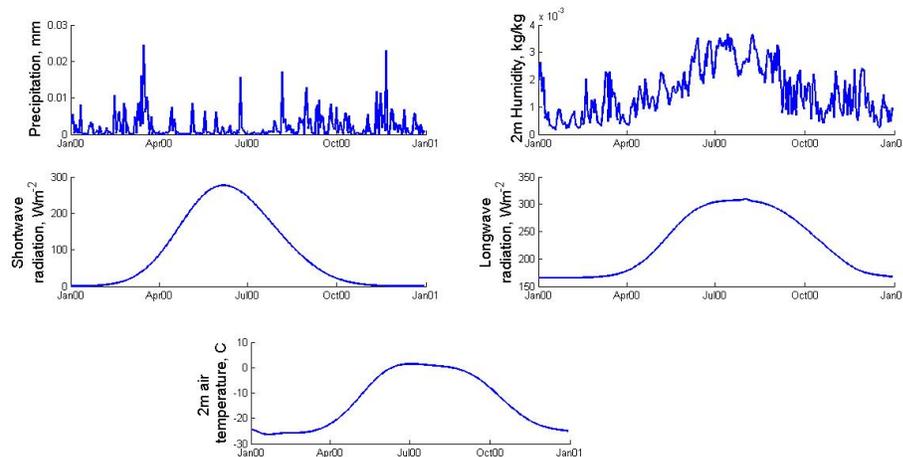
Figure 4.3: Precipitation, 2 m specific humidity, incoming shortwave and longwave radiation, and 2 m temperature forcings for 75°N 210°E.

The forcings used for precipitation, 2 m specific humidity, incoming shortwave radiation, incoming longwave radiation, and 2 m air temperature are shown in Figure 4.3. The first two of these parameters use ERA-Interim for 2015 at 75 °N 210 °E, while the second two are the same Gaussian interpolations of ERA-Interim reanalysis data for the same location that were used in Flocco et al. [2015] and were originally presented and evaluated by Dee et al. [2011]. A constant wind speed was used throughout the simulation, to ensure that individual weather events did not confuse our results. Since the

wind speed exhibits no strong seasonal cycle that might affect the timing of events, this is a reasonable simplification for our study. We chose a value of 3 ms^{-1}.

In Figure 4.4, we see the thicknesses of the sea ice layers in the slab (red) and under-ice melt pond (blue) cases over the course of one year. In both cases, the sea ice thickens during the winter and early spring, thins in the warmer months, and begins to thicken again in the latter months of the year. There is a sudden increase in thickness in the under-ice melt pond case early in the thinning period, after which the sea ice continues to thin. This spike is due to the formation of the false bottom, after which point we calculate the ice thickness as the difference between the surface of the sea ice and the base of the false bottom. In this way, we account for the formation of the new ice and the extra distance that any incoming solar radiation has to penetrate through to reach the ocean.
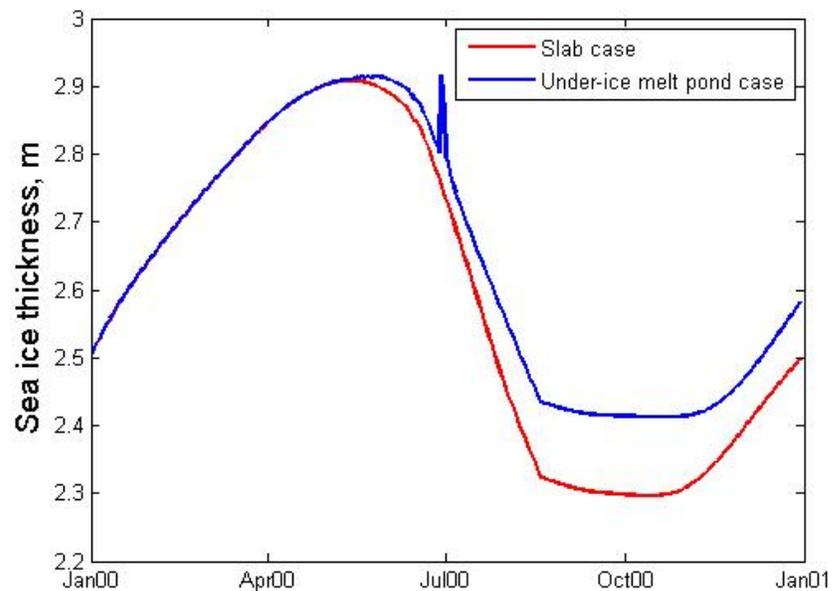
Figure 4.4: Sea ice thickness (m) over the course of 1 year, starting at the beginning of January, for the slab (red) and under-ice melt pond (blue) cases.

As expected, the two slabs of sea ice thicken at exactly the same rate over the spring months but then deviate from one another during the warmer season after the formation of the false bottom. The difference between the two cases reaches a maximum during the summer, but they continue to follow similar gradients along their separate paths.

Around November, the two profiles begin to thicken again, consistent with measurements from the SHEBA campaign Perovich et al. [1999]. In the rest of this section, we look at the reasons for these differences and investigate any concurrent differences in the oceanic mixed layer's key properties in the two simulations.

Figure 4.5 shows the depth of fresh water collected beneath the sea ice during Stage 1. The onset of this accumulation of melt water corresponds to the point at which the sea ice thicknesses begin to diverge, and once it reaches the critical depth and has been present for at least 12 days, we set it to zero and begin Stage 2.
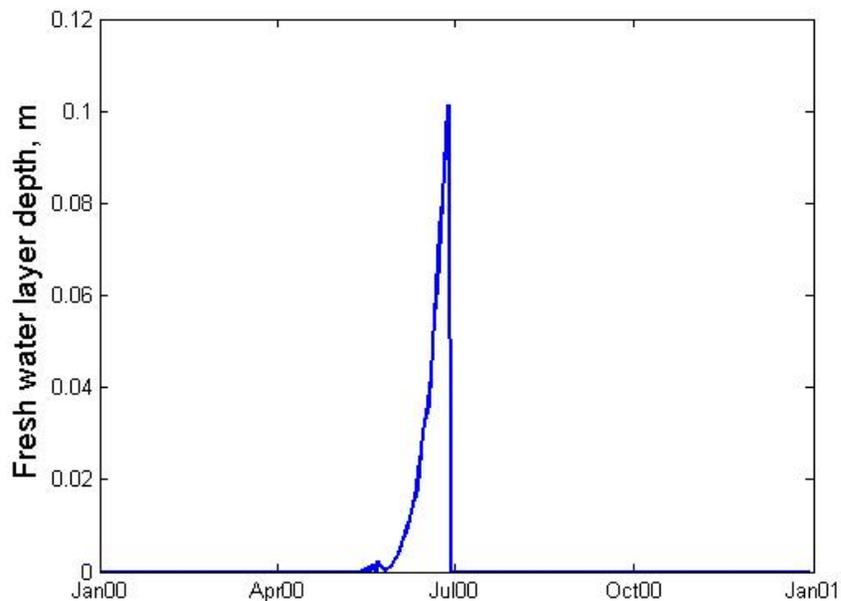
Figure 4.5: Depth (m) of the fresh water layer collecting beneath the sea ice in Stage 1 over the course of 1 year, starting at the beginning of January, for the slab (red) and under-ice melt pond (blue) cases. Once Stage 2 begins, we reset it to zero.

If the layer of fresh water has a non-zero depth, then the sea ice grows into this layer, reducing its thickness, rather than growing into the ocean water. We can see evidence of this in Figure 4.5 in a period spanning mid to late May, where the fresh water layer alternates between growing and shrinking. Our model also takes into account the change in liquidus temperature that accompanies this different freezing medium; rather than using the mixed layer salinity to calculate the liquidus temperature, we instead use the under-ice melt pond's salinity. We see this shift clearly in Figure 4.6, where the liquidus

temperature at the base of the ice jumps from around -2 °C to roughly -0.3 °C during the period that the fresh-water layer is present without a false bottom, and decreases again once the false bottom has formed and the base of the domain is again in direct contact with the ocean. In the early stages of the melt season, the liquidus temperature drops back down to the lower value at points when the sea ice freezes through the thin layer of fresh water that has amassed beneath it and is again growing into the ocean. The region that appears to be solid blue is actually comprised of rapid oscillations between the two water type's liquidus temperature as the sea ice freezes through shallow layers of fresh water and melt water again drains and collects beneath the ice, forming a new fresh water layer. These oscillations could be an artifact of the finite spatial and temporal resolutions of the model, with finer time step and grid cell size potentially resolving this initial drainage and freezing process better. However, in this period the fresh water layer is of the order of a millimeter deep and it is unlikely to be deep enough for distinguishable false bottom formation, so is not important in the context of our aims.
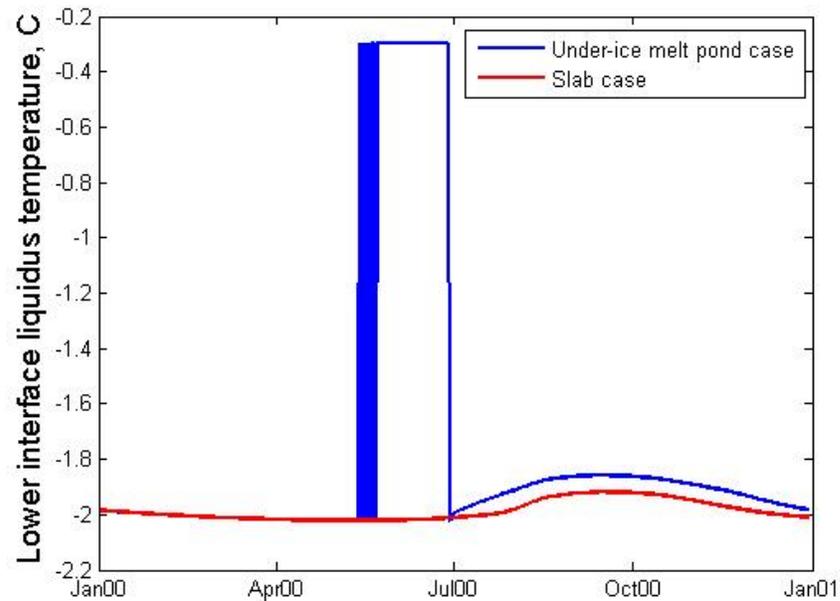
Figure 4.6: Liquidus temperature (°C) at the base of the sea ice over the course of 1 year, starting at the beginning of January, for the slab (red) and under-ice melt pond (blue) cases.

Once the false bottom has formed and we again use the ocean salinity during ice growth, there is a difference in the liquidus temperature of the two cases. The slightly

higher value in the under-ice melt pond case suggests that the mixed layer is less saline after the formation of the false bottom in this simulation.
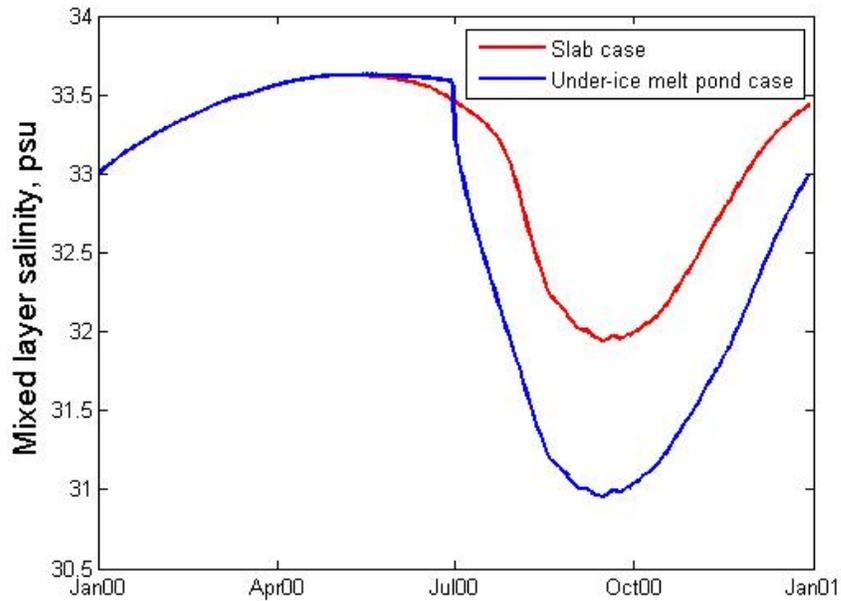
Figure 4.7: Mixed layer salinity (psu) over the course of 1 year, starting at the beginning of January, for the slab (red) and under-ice melt pond (blue) cases.

We see in Figure 4.7 that the mixed layer is indeed fresher in the under-ice melt pond case in the wake of the false bottom's formation. Before this, they evolve at the same rate until the start of the melt season. Once the ice begins to thin, the mixed layer freshens more rapidly in the slab case, since all of the surface melt drains into the mixed layer; in the under-ice melt pond case, before the formation of a false bottom, we allow only 20% of the surface melt to drain into the mixed layer and gather the remaining 80% beneath the sea ice to form the under-ice melt pond. [Flocco et al., 2015] found that the ice below the surface pond in their refreezing simulations rapidly became impermeable after some initial drainage, which could affect the seasonality and depth of the forming fresh-water layer. [Polashenski et al., 2017] noticed similar seasonal changes in ice permeability, blocking surface drainage of melt water through the sea ice. This may indicate that under-ice melt ponds are more likely to form due to macroscopic flaws and cracks in the sea ice or via lateral run-off from a floe. More observations are needed of the formation stage of under-ice melt ponds to identify which mechanism(s) is (are) dominant and

important to include in models, as most field and lab work has been focussed on the properties and evolution of extant under-ice melt ponds. The primary impact of using a more complete treatment of the formation of the fresh-water layer would most likely be in the timing and rapidity of the formation process due to seasonal changes in the ice cover's properties, as well as exposure and resilience to weather events. For now, our general approach allows us to consider any of the three drainage mechanisms discussed here.
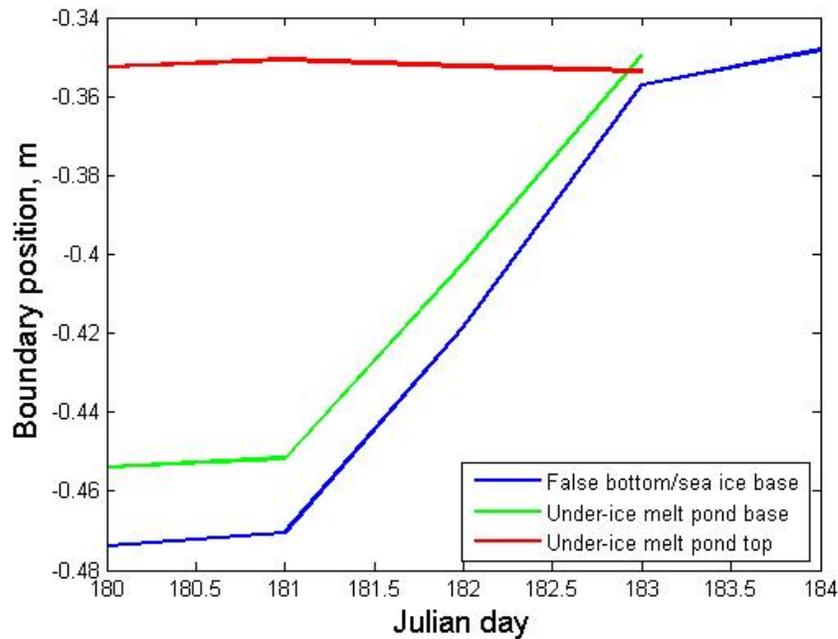
Figure 4.8: Boundary positions (m) of the under-ice melt pond and the domain's base during the evolution of the under-ice melt pond.

In Figure 4.4, we saw rapid ablation after the false bottom forms. This corresponds to the migration of the false bottom upwards, effectively transferring fresh water from the under-ice melt pond to the ocean. Figure 4.8 shows the position of the under-ice melt pond boundaries during its evolution, as well as the position of the base of the domain (either the base of the false bottom or the base of the sea ice.) The swift migration upwards from the end of June forwards corresponds with the large drop in mixed layer salinity in the under-ice melt pond case. During this period, the under-ice melt pond case's mixed layer becomes considerably fresher than that of the slab case, before following a similar trajectory to the slab case once the false bottom has frozen through the

under-ice melt pond. This corresponds to the short period in which the mixed layer is more saline in the under-ice melt pond case before rapidly freshening beyond that of the slab case.

As the sea ice thickens again in the cooler months, the mixed layer becomes more saline again, in large part due to salt rejection during the growth of the ice. Figure 4.9 shows the fluxes of salt into the mixed layer over the year simulation. Negative values indicate freshening.
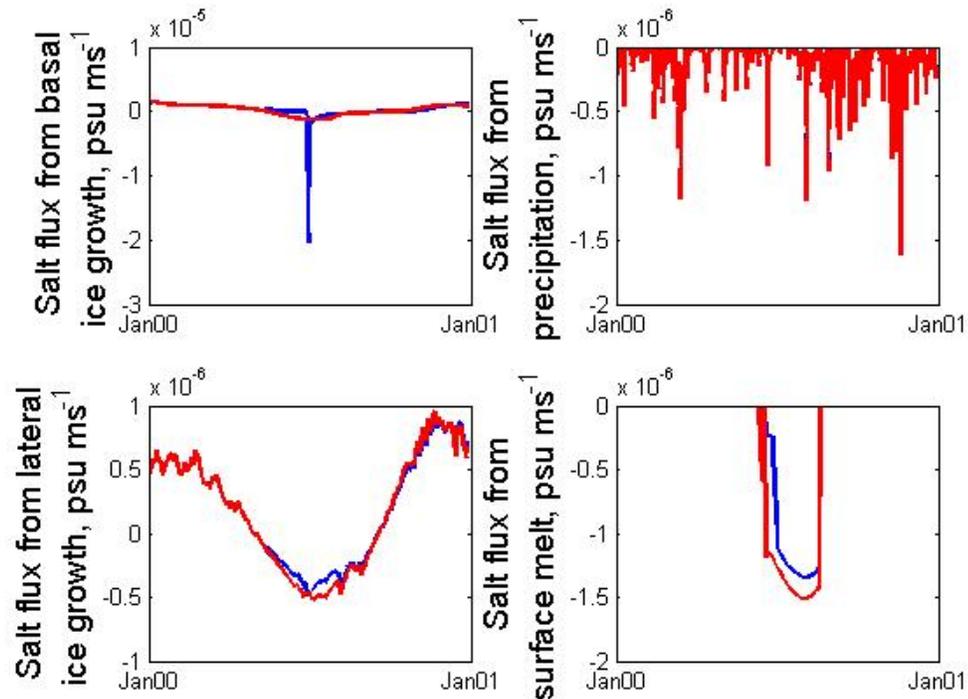

Figure 4.9: Virtual fluxes of salt into the mixed layer via basal ice growth/ablation, precipitation, lateral ice growth/ablation, and ice surface ablation over 1 year starting at the beginning of January for the slab (red) and under-ice melt pond (blue) cases. Note that the scale of y-axis of the panel showing salt flux due to basal ice growth is an order of magnitude larger than the other panels.

The top-left subplot shows the salt flux due to the growth or ablation of the sea ice at its base. We see that there is indeed an increased salt flux into the mixed layer during the formation of the under-ice melt pond relative to the evolution of the bare slab of ice. A clear, much more dominant, spike in freshening is apparent during the migration of the false bottom, before a return to very similar salt fluxes to those in the slab case,

explaining the persisting difference in the salinity time series beyond the evolution of the false bottom.

The freshening due to precipitation, shown in the top-right subplot, is almost identical between the two cases; the same precipitation time series is used to force the two simulations, but the amount reaching the mixed layer is limited by the fraction of the surface area of the ocean that is covered by sea ice. The smaller the open lead fraction, the less fresh precipitation enters the mixed layer. In Figure 4.10, we see that the two cases exhibit very similar ice area fractions. The slab case's sea ice reaches a slightly lower area fraction in the summer months.
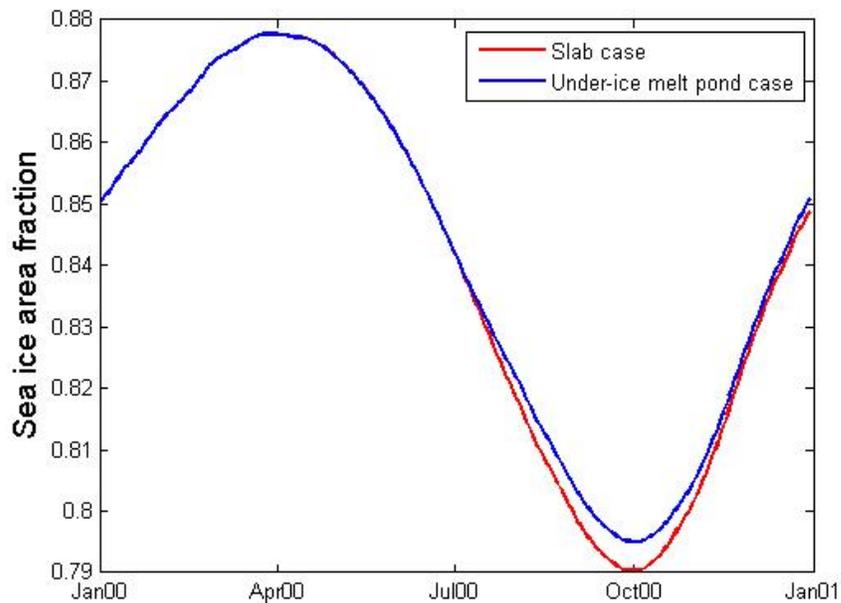
Figure 4.10: Sea ice area fraction over the course of 1 year for the slab (red) and under-ice melt pond (blue) cases.

The bottom-left subplot of Figure 4.9 shows the salt flux due to lateral growth/ablation of the sea ice, i.e. a change in its area. This salt flux depends on the difference between the mixed layer salinity and the sea ice's bulk salinity, as well as the volume of ice grown/ablated. The resulting salt fluxes are fairly similar in the two cases, with the main difference occurring in summer, when the difference in mixed layer salinity appears to be highest and there is the beginning of the largest difference in the change in ice area.

The salt fluxes due to surface melt, shown in the bottom-right subplot of Figure 4.9, are zero for the majority of the year. In the summer, they quite rapidly increase to their peaks, and again decrease swiftly at the end of the melt season. The under-ice melt pond case sees slightly less freshening due to surface melt, potentially due to a difference in the amount of surface melt or due to the difference in mixed layer salinities.

Figure 4.11 shows the depth of the mixed layer for each case over the course of a year. In both scenarios, the mixed layer is deeper in the winter months, with a maximum of around 43 m, and shallower in the summer, reaching the model's minimum depth of 5 m. The two time series evolve identically up until the start of the melt season, when the under-ice melt pond case's mixed layer becomes slightly deeper than the slab case's. This can be attributed to the higher mixed layer salinity in this period in the under-ice melt pond case. Once the false bottom joins the base of the sea ice and the mixed layer drastically freshens, we see an accompanying rapid shallowing of the mixed layer. The model's hard minimum prevents any difference in mixed layer depth between the two cases in high summer, but the slab case's higher salinity makes it deepen more during in the cooler months at end of the year.
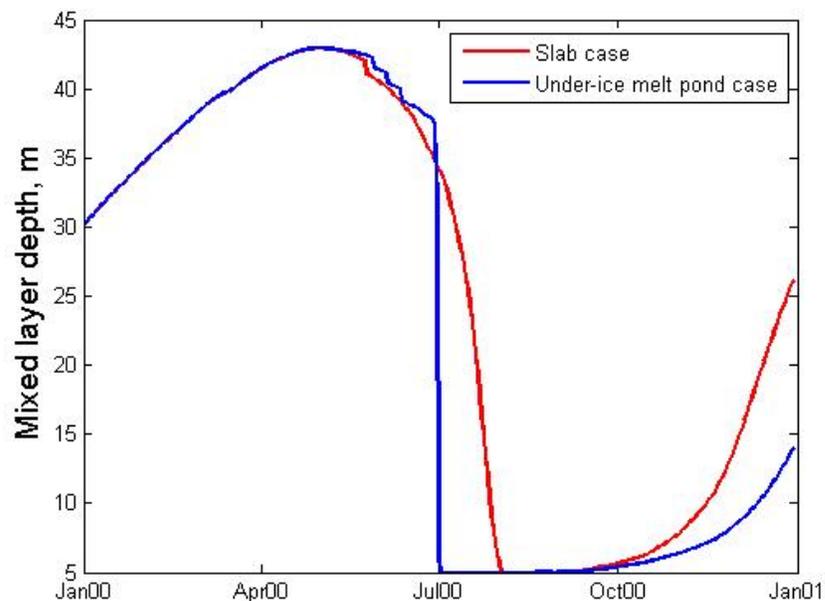
Figure 4.11: Mixed layer depth (m) over the course of 1 year, starting at the beginning of January, for the slab (red) and under-ice melt pond (blue) cases.
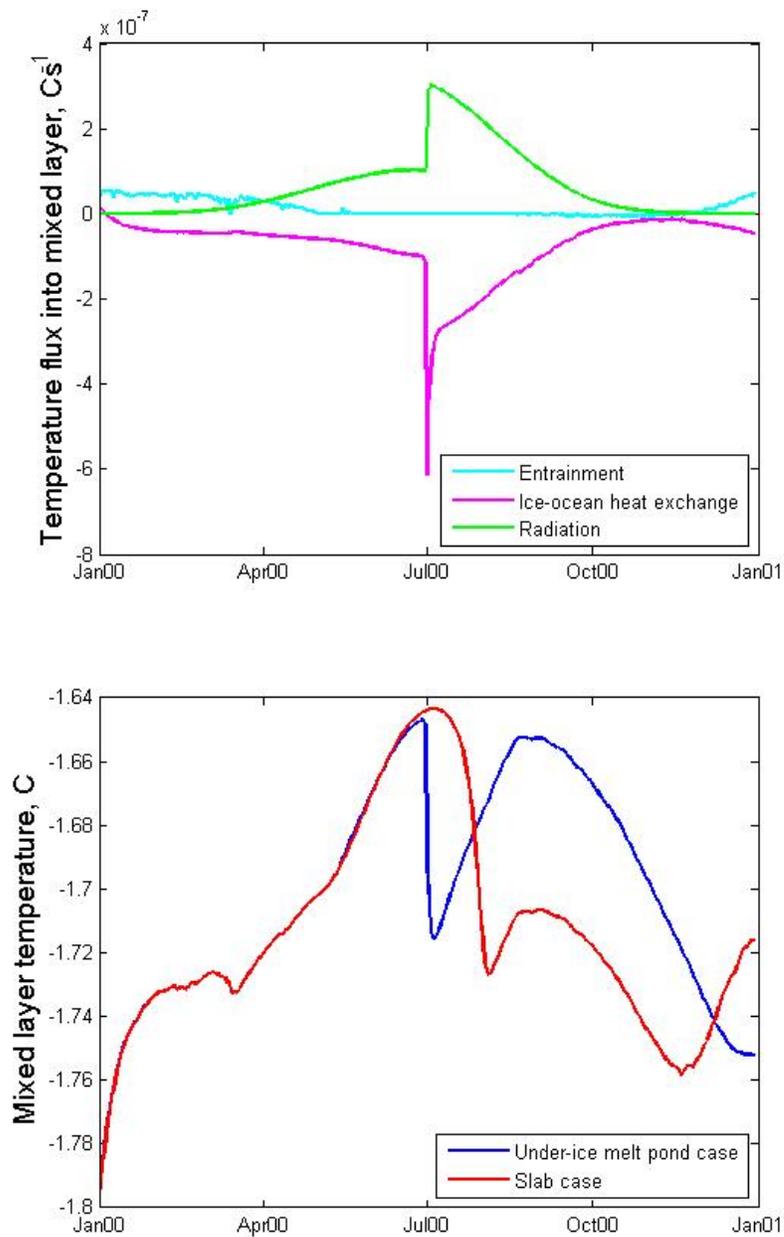
Figure 4.12: (upper) Temperature fluxes into the mixed layer over the course of the year for the under-ice melt pond case. Fluxes shown are those due to entrainment (cyan), heat exchange with the sea ice (magenta), and radiative heating (green). (lower) Mixed layer temperature (°C) over the course of 1 year for the slab (red) and under-ice melt pond (blue) cases.

The mixed layer temperature (see Figure 4.12 (lower)) also affects its buoyancy, driving entrainment or detrainment of deeper ocean water. In our model, changes to the mixed layer are a complex mix of incoming solar radiation, heat flux to the sea ice, latent

heat, heat flux to the open lead waters, and the entrainment of warmer water. In both cases, the water is typically warmer in the summer and cooler in the winter, as expected, with cooling during periods of heavy melt, due to loss of latent heat when melting ice. There is a decrease in the summer when each mixed layer quickly shallows to a minimum. At this point, any heat flux into or out of the mixed layer is spread over a much smaller volume of water, and so has a proportionally larger effect before the system can adjust. The heat flux from the mixed layer into the sea ice dominates at this point, as seen in Figure 4.12 (upper).

These modelled mixed layer properties are reasonably consistent with measurements presented in Peralta-Ferriz and Woodgate [2015], in which they used marine profiles taken using CTDs to analyse regional mixed layer properties across the Arctic. Peralta-Ferriz and Woodgate [2015] found the mixed layer to average 30 - 40 m in the Winter, and regularly between 40 and 50 m, for the Canada Basin, while our model output exhibits a Winter maximum mixed layer depth of around 43 m within the same geographical region. Our model shallows to a minimum of 5 m in the summer, whereas these observations suggest that higher values are more realistic, with a summer average of 9 m. Our predicted winter salinity values are a little high compared to the measurements, but summer salinities fall within the high-end of the measured range of roughly 16-32 psu. Our coupled sea ice-ocean model generally captures the annual cycles of mixed layer temperature, salinity, and depth.

4.3.3 The mixed layer's effects on the ice

By decoupling the ice model from the mixed layer model, we can see the effect that introducing a simple mixed layer model has on the ice's evolution. Here, we look at simulations identical to those that we just discussed, with the exception that the ocean properties are the same throughout the simulation, i.e. there is no model to alter the mixed layer properties from their initial conditions.

Figure 4.13 shows the ice thicknesses of the four simulations (under-ice melt pond model with and without the ocean, and slab model with and without the ocean.) We see that the mixed layer model has the effect of thinning the sea ice compared to the uncoupled model.
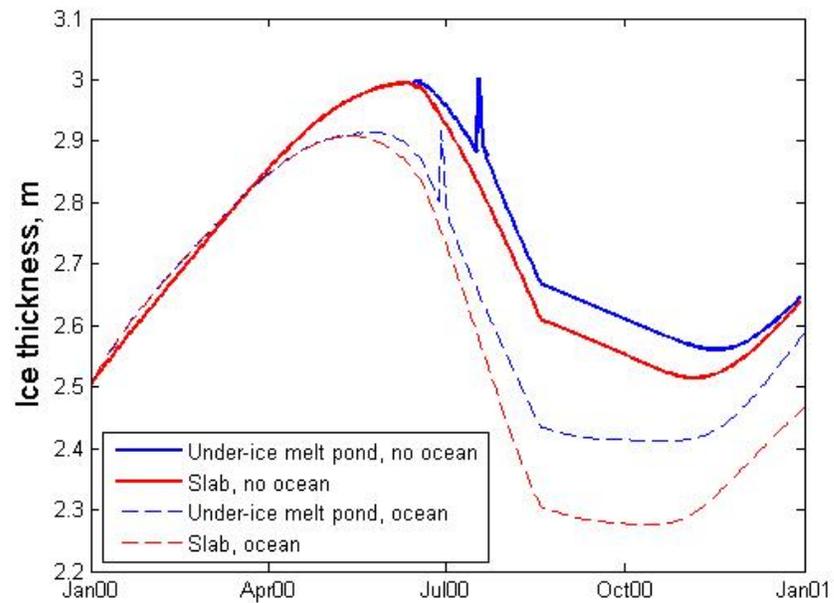
Figure 4.13: Sea ice thickness (m) over one year for the under-ice melt pond and slab case with (dashed) and without (solid) the ocean model.
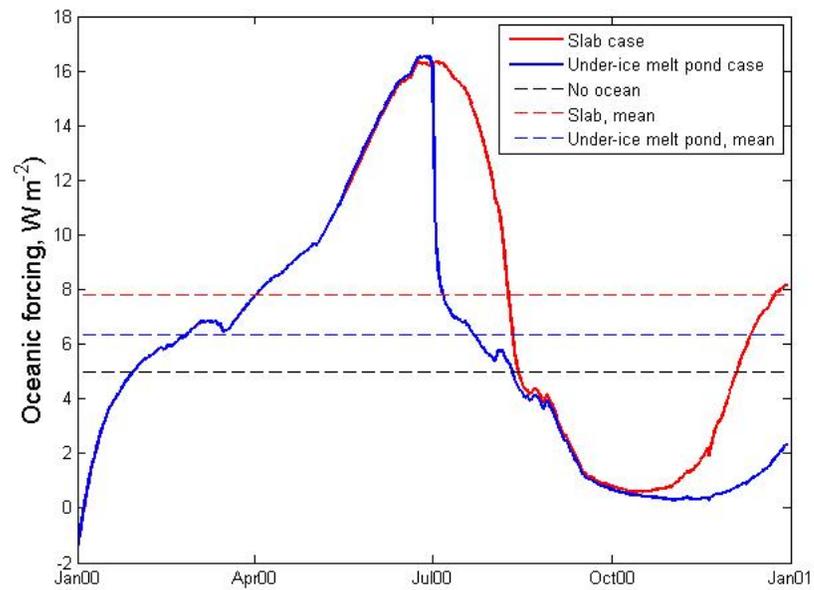
Figure 4.14: Oceanic forcing (Wm^{-2}) for the under-ice melt pond and slab case with (dashed) and without (solid) the ocean model.
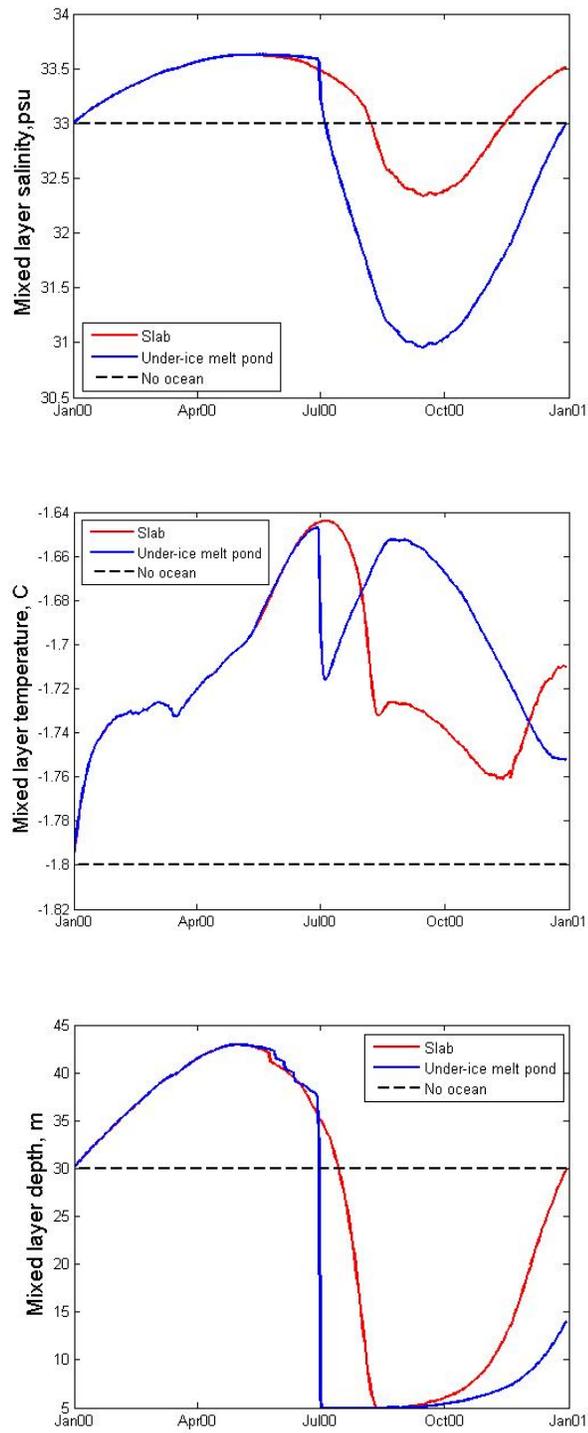
In Figure 4.15, we see the mixed layer properties of the coupled simulations together with the initial conditions. The mixed layer temperature is significantly higher in the coupled simulations, which should lead to a higher heat flux into the sea ice. We show the heat flux from the mixed layer into the ice in Figure 4.14, alongside which the mean value for the year for the two cases and the constant value of the decoupled model are plotted, to check this. The decoupled model does have a lower oceanic forcing value than the mean of either of the two coupled model simulations, which results in thicker sea ice than in the coupled model simulations.

4.3.4   Under-ice melt ponds and the oceanic mixed layer

The comparison of the two coupled ice-ocean simulations suggest that the formation and evolution of under-ice melt ponds could have a significant effect on key properties of the mixed layer. Based on this study, the mixed layer seems to be slightly saltier during the early stages of this process, when a false bottom has not yet formed and we see enhanced thickening of the sea ice. Once the false bottom has formed and migrates upwards, we see a freshening of the mixed layer, causing it to shallow to a summer minimum sooner than it would were the under-ice melt pond absent. The mixed layer also remains fresher in the cooler months at the end of the year, when it starts to deepen again. This indicates there could be a cumulative effect over the course of multiple years.

The ice is significantly thicker as a result of the under-ice melt pond, even before the false bottom forms. Again, while this difference lessens by the end of the year, it is still present going into the next annual cycle, suggesting there could be a stronger effect if an under-ice melt pond forms in the next year as well.

In the following section, we will therefore carry out several multi-year simulations to test the long-term effects of under-ice melt ponds on the sea ice and the oceanic mixed layer. We will then test the sensitivity of the model to several parameters and see whether the effects of the under-ice melt pond on its surroundings seen here are similar under other conditions.

Figure 4.15: Mixed layer properties for the slab (solid, red), under-ice melt pond (solid, blue), and no ocean (dashed, black) cases.

## 4.3.4.1   Reference case: Multi-year simulation
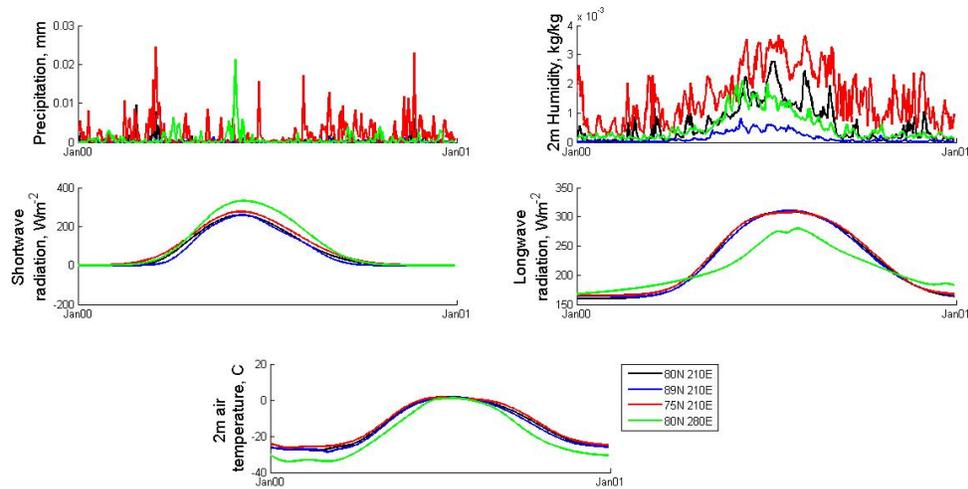
Figure 4.16: Precipitation, 2 m specific humidity, incoming shortwave and longwave radiation, and 2 m temperature forcings for 80°N 210°E, 89°N 210°E, 75°N 210°E, and 80°N 280°E.

We now carry out a multi-year reference simulation, which we will subsequently use to carry out sensitive studies against, with forcings for 80°N 210°E, namely the precipitation, 2 m specific humidity, the incoming shortwave and longwave radiation, and the 2 m air temperature, shown in Figure 4.16. We use the same ambient profiles illustrated in Figure 4.2. We run the model for ten years with these forcings and ambient profiles, after a spin-up period of three years.

In this simulation, the false bottom is assumed to have formed once a non-zero depth of fresh water has accumulated beneath the sea ice for at least 12 days, as indicated necessary in the results of Chapter 2 and has reached a depth of at least 10 cm. We reset the depth of this fresh water layer to zero and continue to the next stage of the simulation. In Figure 4.17, we see the depth of the fresh water layer over time. It rises from 0 to over 10 cm at an increasing rate over the course of days.
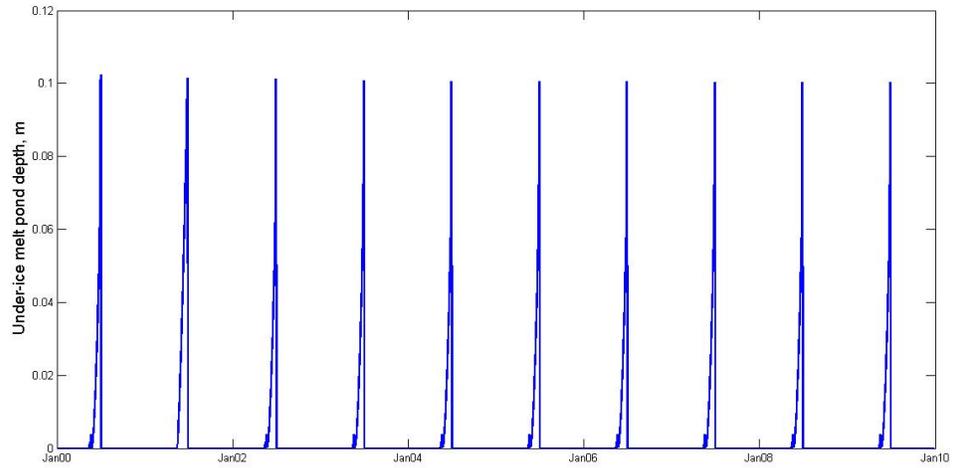
Figure 4.17: Depth (m) of the fresh water layer beneath the sea ice over time. It reduces to zero each year once we switch to the under-ice melt pond evolution stage of the simulation.
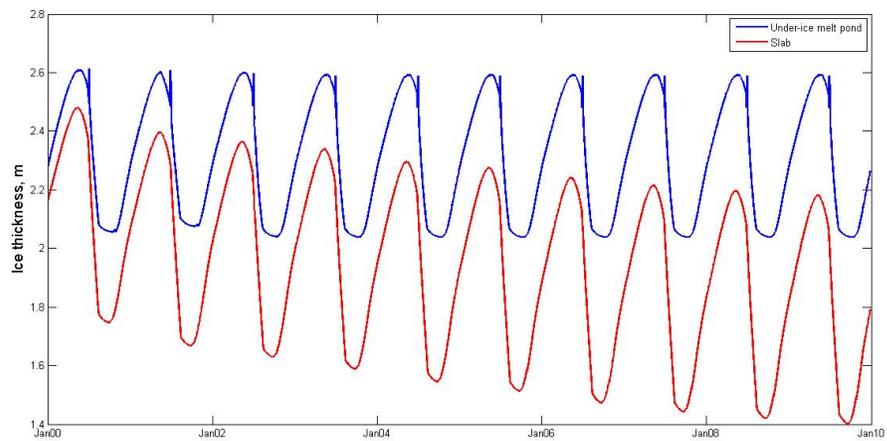
Figure 4.18: Sea ice thickness (m) for ten years, after a spin up period of three years, for the under-ice melt pond case (blue) and the slab case (red).
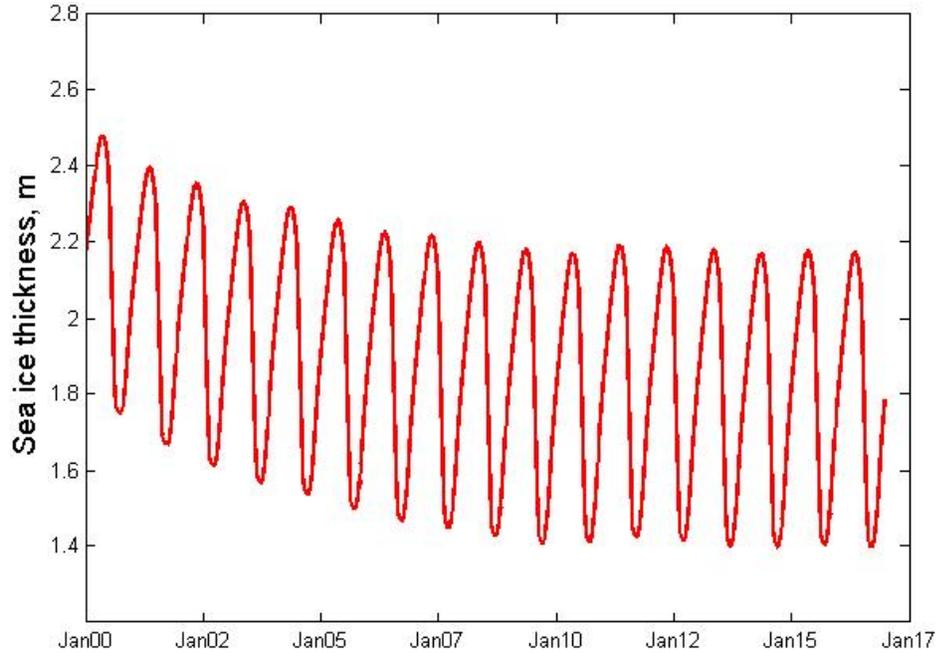
Figure 4.19: Sea ice thickness (m) for seventeen years, after a spin up period of three years, for the slab case.

Figure 4.18 shows the ice thickness for the under-ice melt pond case (blue) and the slab case (red) for ten years following an initial spin up period of three years. The sea ice in the under-ice melt pond case appears to have reached a fairly steady state, oscillating between around 2.6 m thick in the cold months and just under 2.1 m thick in the warm months. A clear sudden increase in ice thickness is seen when the false bottom forms each year, significantly raising the thickness of the ice early in the melt season. The formation of the false bottom puts the under-ice melt pond case on a path of thicker sea ice than the slab case, which appears to be approaching a steady state of lower thickness.

Carrying out a longer simulation confirms that the ice of the slab case has indeed reached a stable seasonal cycle of ice thicknesses by the end of the ten year period (see Figure 4.19), at which point the slab case ice is oscillating between about 2.2 m of ice in the winter and 1.4 m at the September minimum.

The mixed layer depths for the two cases are fairly similar during this ten year period. They follow an annual cycle of deepening in the cold months and shallowing to the

prescribed minimum of 5 m in the warmer months. They deepen and shallow at the same time as each other, but the mixed layer in the under-ice melt pond case is slightly shallower at its winter maximum than the slab case's mixed layer. The mixed layer deepens to about 45 m in the cold months, whereas the slab case reaches over 55 m deep by the end of the ten year period. Since we keep the wind constant, the difference in mixed layer depth must be due to either a difference in temperature or salinity.
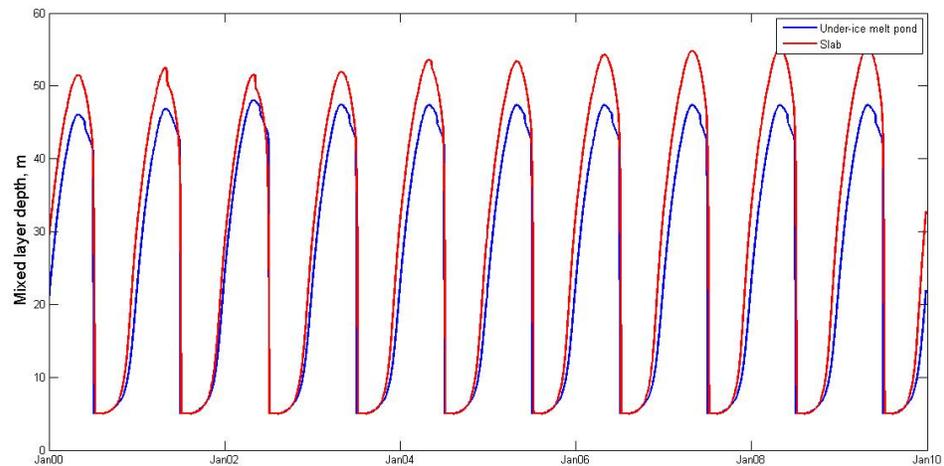
Figure 4.20: Mixed layer depth (m) for ten years, after a spin up period of three years, for the under-ice melt pond case (blue) and the slab case (red).

There is little difference in the mixed layer temperatures of the under-ice melt pond and slab cases. The two time series are shown in Figure 4.21, where we see that the mixed layer reaches marginally warmer peaks in the under-ice melt pond case than in the slab case, and the slab case is slightly warmer during the spring months, possibly due to the presence of thinner sea ice. Both occupy a band between roughly -1.76 and -1.66 °C apart from one anomalous spike in the second year of the under-ice melt pond simulation, and both are generally warmer in the summer and colder in the winter, as expected. The spike in the second year is due to entrainment of warmer water rather than any sea ice interaction, a shown in Figure 4.22, where we plot the contributions for the change in mixed layer temperature in that year from the entrainment of warmer water and from heat fluxes between the sea ice and the ocean in the under-ice melt pond case. It is an artifact of the predictor-corrector method for calculating mixed layer properties described in Section 4.3.1. Following the rapid detrainment of deep ocean water from the
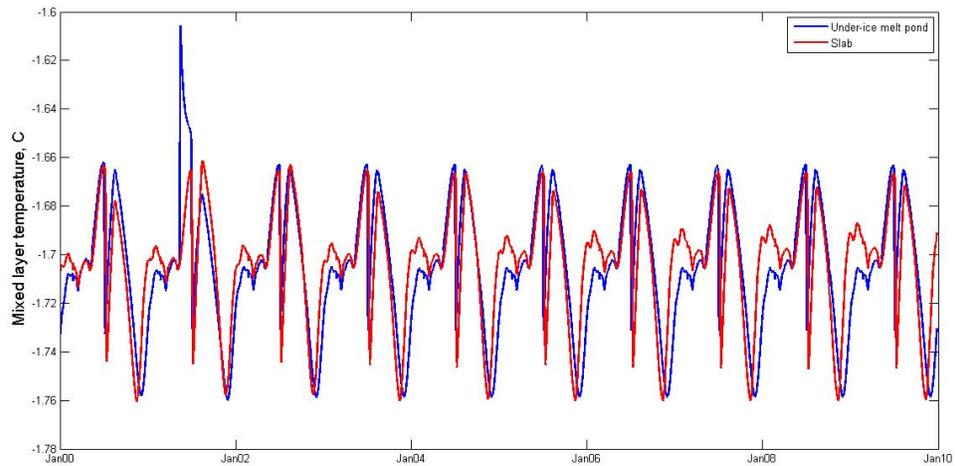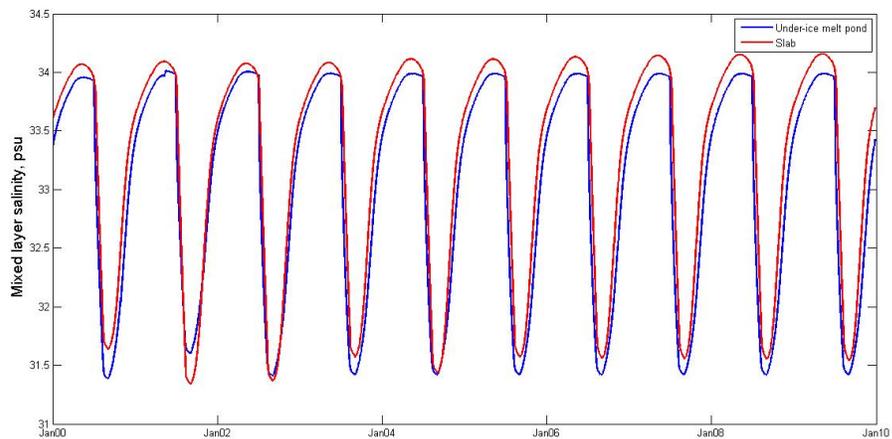
Figure 4.21: Mixed layer temperature (°C) for ten years, after a spin up period of three years, for the under-ice melt pond case (blue) and the slab case (red).

mixed layer, there is little difference in buoyancy between the mixed layer waters and that in the grid cell directly below it. The properties of the 10th grid cell are therefore used in the mixed layer calculations, suppressing sudden entrainment and distributing the heat fluxes into the mixed layer over a shallower depth of water.

There does not seem to be such a large difference in the two temperature time series to explain the difference in mixed layer depth. There is, however, a significant difference in the mixed layer salinity time series for the two cases (see Figure 4.23.) While there are distinct annual cycles in the mixed layer salinities, that of the under-ice melt pond simulation is much fresher on average than that of the slab simulation. This would lead to a more buoyant, lower density mixed layer, accounting for the shallower mixed layer in the under-ice melt pond case. While there is little additional salt added to the mixed layer from the formation of the false bottom compared to the slab case, there is a sudden dramatic freshening during the evolution of the false bottom, which rapidly migrates upwards. This effectively delays the transfer of fresh melt water to the mixed layer and then deposits it into the ocean over a very short period of time.
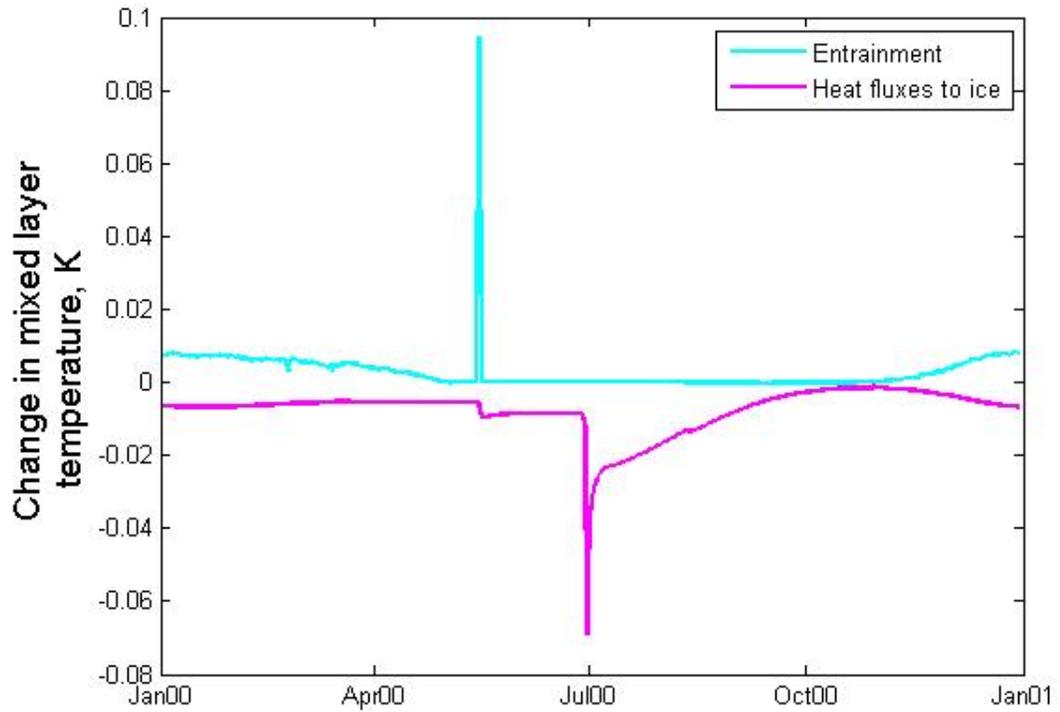
Figure 4.22: Contributions to the change in mixed layer temperature (C) from entrainment and sea ice-ocean heat fluxes during the second year of the reference simulation, in which a spike in mixed layer temperature is seen around mid May.

Figure 4.23: Mixed layer salinity (psu) for ten years, after a spin up period of three years, for the under-ice melt pond case (blue) and the slab case (red).
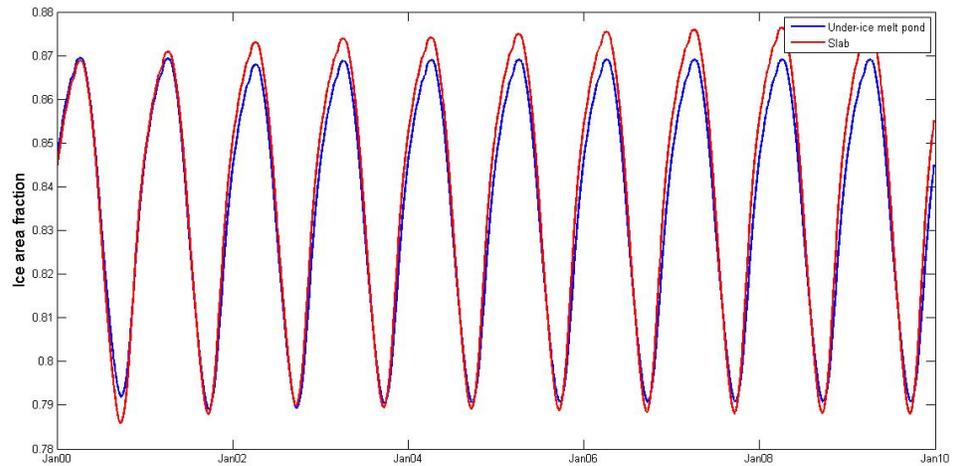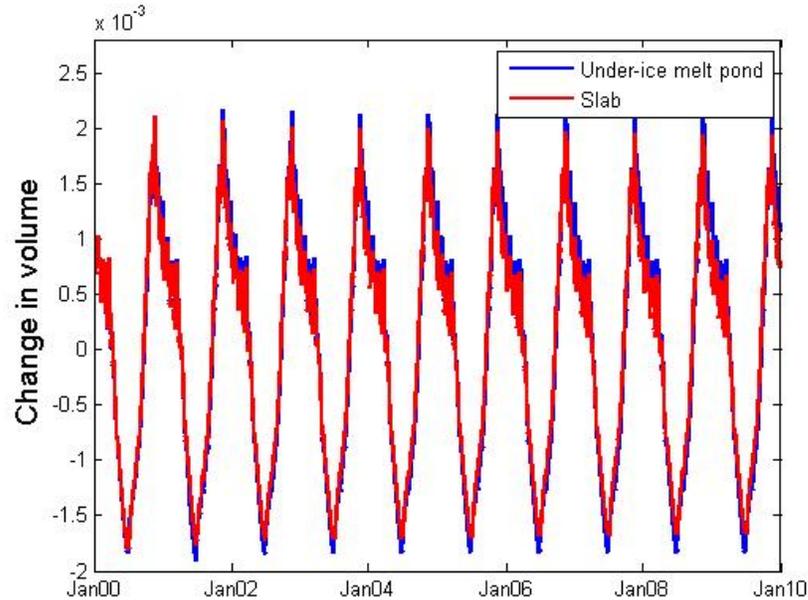
Figure 4.24: Sea ice area fraction for ten years, after a spin up period of three years, for the under-ice melt pond case (blue) and the slab case (red).
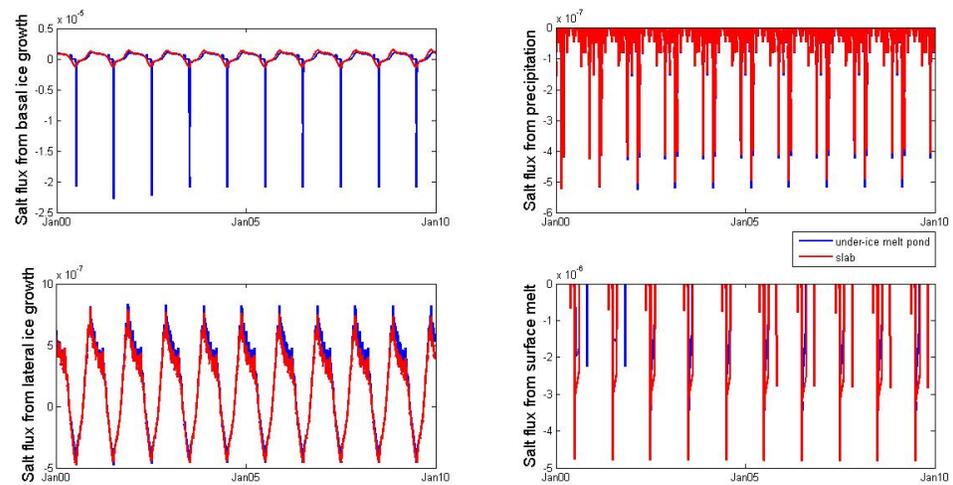
Figure 4.25: Salt fluxes into the mixed layer (psu ms^{-1}) for ten years, after a spin up period of three years, for the under-ice melt pond case (blue) and the slab case (red).

Our model parameterises the false bottom formation process as described earlier in the chapter, which could have an effect on the salinity profile. We add the salt from the false bottom formation in one time step once the false bottom has completely formed according to the results of Chapter 2, though the mere two centimeters of ice growth does not seem to involve a large amount of salt rejection, and is vastly outweighed by

the rapid release of fresh water during its migration upwards. The subsequent winter ice growth is similar in magnitude to that of the slab case, so the mixed layer remains fresher than that of the slab case in the wake of the under-ice melt pond.

Figure 4.26: Volume change of sea ice due to lateral growth/melt for ten years, after a spin up period of three years, for the under-ice melt pond case (blue) and the slab case (red).

Figure 4.24 shows the fraction of horizontal area covered by sea ice for the two simulations. While the two cases see a similar areal minimum in the warm months, the slab case sees slightly higher horizontal growth of the sea ice in the winter. The relationship between the mixed layer salinity and the sea ice area is somewhat complicated. The salt contribution to the mixed layer from lateral growth/melt is not only proportional to the change in area fraction, but also the difference between the sea ice and mixed layer salinities, as well as the sea ice thickness. Not only does the lateral ice growth increase the salinity of the slab simulation's mixed layer, but a higher ice area fraction also allows less precipitation to reach the mixed layer, reducing its freshening effect.

We plot the salt fluxes from each source for the two simulations in Figure 4.25, where we see that the precipitation is indeed slightly higher in the under-ice melt pond case, where there is more exposed ocean. The salt flux due to lateral growth/melt is actually higher during the winter in the under-ice melt pond case, since its thicker sea ice means

it sees a greater volume increase despite the higher lateral growth in the slab case. This is shown in Figure 4.26, where we plot the change in volume due to lateral growth/melt of the sea ice for the under-ice melt pond and slab simulations.

4.3.5 Sensitivity studies

4.3.5.1 Location

Figure 4.16 shows climatologies for four locations within the Arctic circle. The incoming shortwave radiation, incoming longwave radiation, and air temperature climatologies are those used by Flocco et al. [2015], and the precipitation and 2 m humidity are from the ERA-Interim dataset. Flocco et al. [2015] did not include precipitation in their study, whereas it is important for us to consider due to its impact on the oceanic mixed layer. We therefore use corresponding ERA-Interim data for the precipitation. Similarly, we use ERA-Interim data for the specific humidity when calculating the latent heat flux at the surface of the sea ice or exposed ocean. The same constant wind speed of $3\,\mathrm{ms}^{-1}$ was used throughout the simulations at each of the four locations.

The sea ice thicknesses and area fractions that arise from using these forcings are shown in Figure 4.27. We see that both properties coincide well with each region's climate, particularly air temperature, for which colder locations see significantly higher ice volumes.

The mixed layer properties react predictably to the locations' differences in forcings, as shown in Figure 4.28. Locations with lower air temperatures and incoming solar radiation, and thus contain thick sea ice and generally have cooler mixed layers. Their mixed layers are more saline, due to salt rejection during freezing of thick slabs of sea ice, leading to a reduction of mixed layer buoyancy, less stratification and deeper mixed layers. Differing rates of precipitation also plays a role in the divergence of the locations' mixed layer salinity.
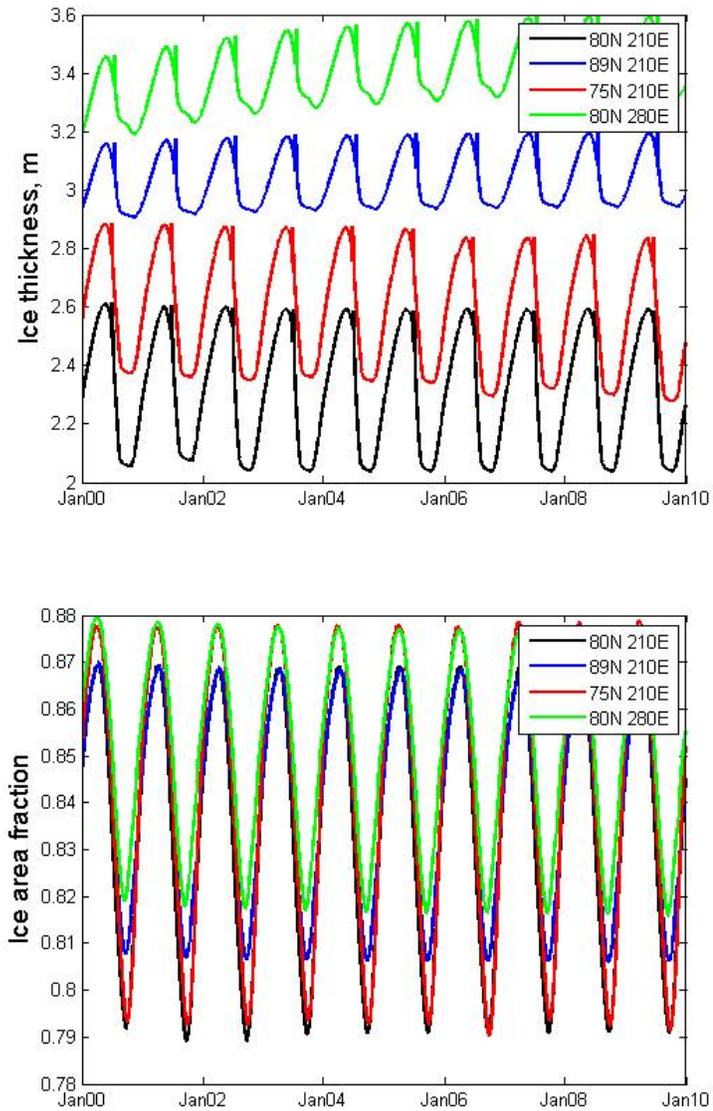
Figure 4.27: Sea ice thickness (m) and area fraction for ten years, after a spin up period of three years, at the four locations.
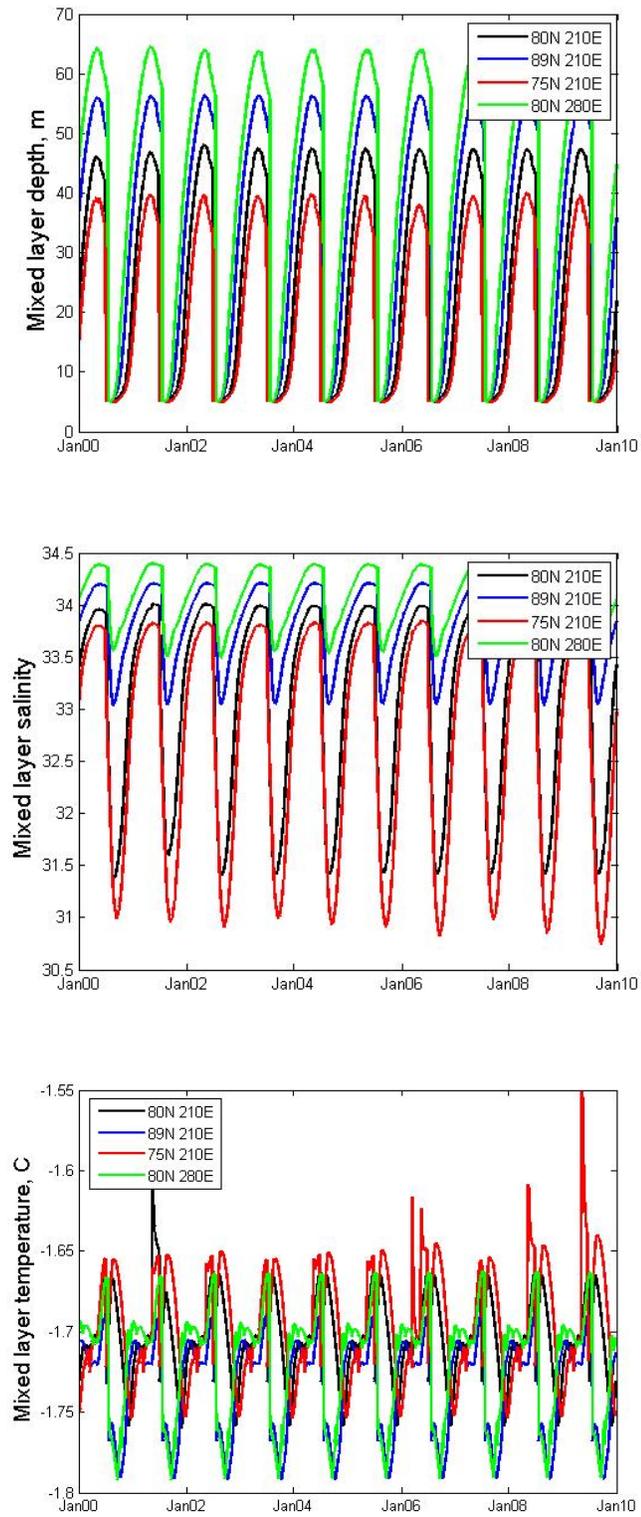
Figure 4.28: Mixed layer depth (m), salinity (psu), and temperature (C) for ten years, after a spin up period of three years, at the four locations.

4.3.5.2   Relaxation time

The relaxation time determines how quickly the ocean properties at a certain depth return to their ambient values after the mixed layer has shallowed to a point above said depth. We now test the effect of reducing the chosen relaxation time from 90 days (reference value) to a much shorter 10 days.
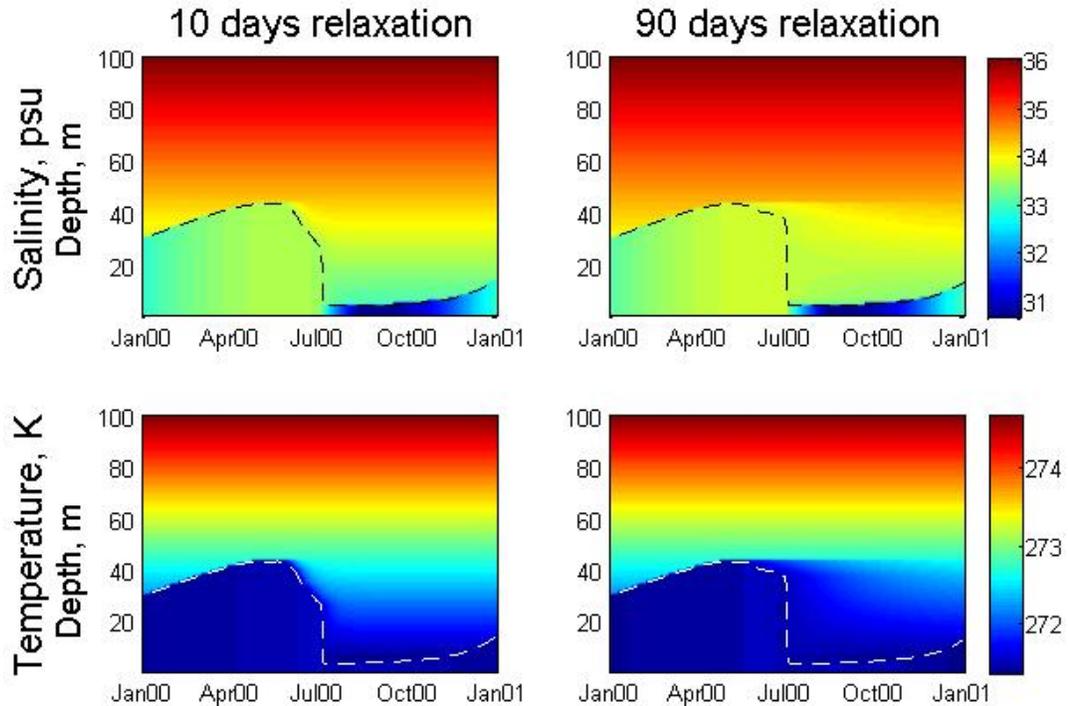
Figure 4.29: Temperature (K) and salinity (psu) profiles throughout the ocean for one year using a relaxation time of 10 days (left) and 90 days (right.) The mixed layer depth (m) is superimposed with a dashed line.

Figure 4.29 shows the salinity (upper) and temperature (lower) of the ocean waters over the course of 1 year using a relaxation of 10 days (left) and 90 days (right.) On top of these fields, we plot the mixed layer depth for the respective simulations as a black line. Once the mixed layer begins to shallow after its maximum, the properties of the ocean water at the depths it used to occupy begin to return to their prior values. As expected, this is seen to take significantly less time when we use a relaxation period of 10 days as opposed to 90 days, for which the ocean still sees lingering effects of the mixed layer maximum well into the autumn.
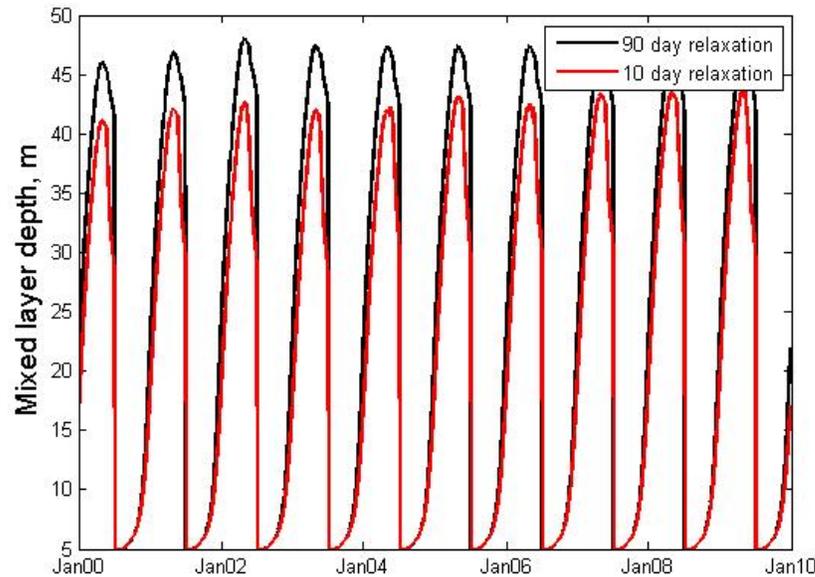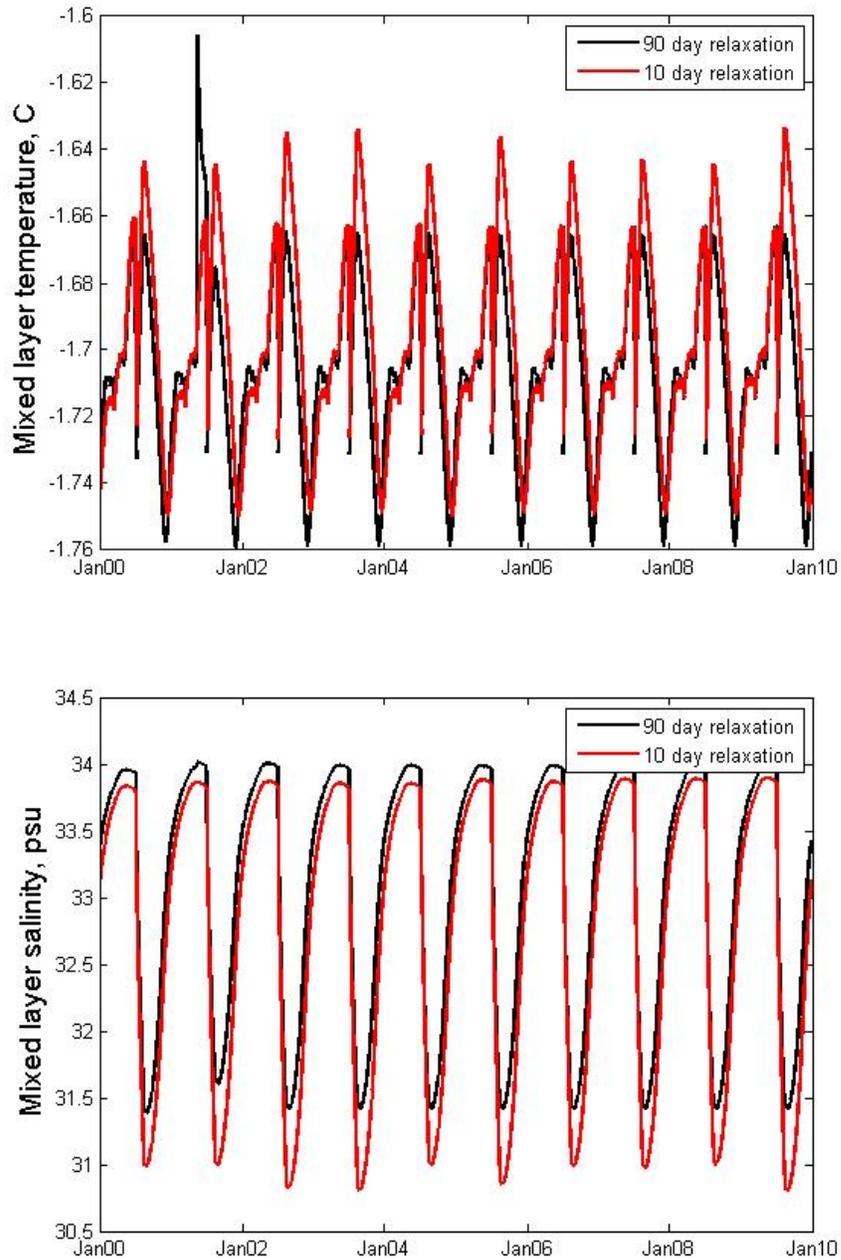
Figure 4.30

This has a knock-on effect on the mixed layer depth as it shallows in the summer. The stronger difference in buoyancy between the detraining mixed layer in the 10-day relaxation scenario forces it to shallow more rapidly in June compared to in the 90-day relaxation scenario, in which it is able to remain thicker until the harsh shallowing that affects both scenarios in early July. Just before this rapid shallowing, the difference in mixed layer depth between the two cases is around 10 m.

In Figure 4.30, we see that this translates into a persistently shallower mixed layer in the summer when we use a relaxation period of 10 days compared to 90 days. The mixed layer appears to be slightly warmer on average in the prior case, since a similar amount of heat is warming a smaller volume of water, and less saline, due to the entrainment of the less salty water left in the wake of the mixed layer maximum during the autumn.

The area fraction of sea ice is a little higher when using the shorter relaxation period (see Figure 4.31 and, after an initial gain during the spin-up period, the sea ice thickness in this scenario decreases in average thickness to a mean lower than that of the longer relaxation period's sea ice. It is difficult to attribute this to any one factor, since the differences between the mixed layers' temperature and salinity will have conflicting effects on

the thickness of the sea ice. Overall, the sensitivity of the area fraction to the relaxation rate is smaller than the changes introduced by switching between the slab and under-ice melt pond cases.
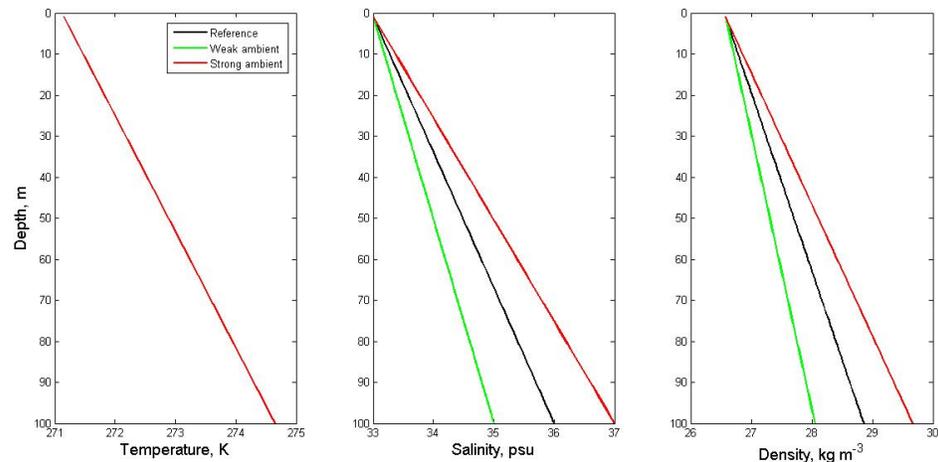

Figure 4.30: Mixed layer depth (m), temperature (C) and salinity (psu) for relaxation times of 10 days (blue) and 90 days (black.)
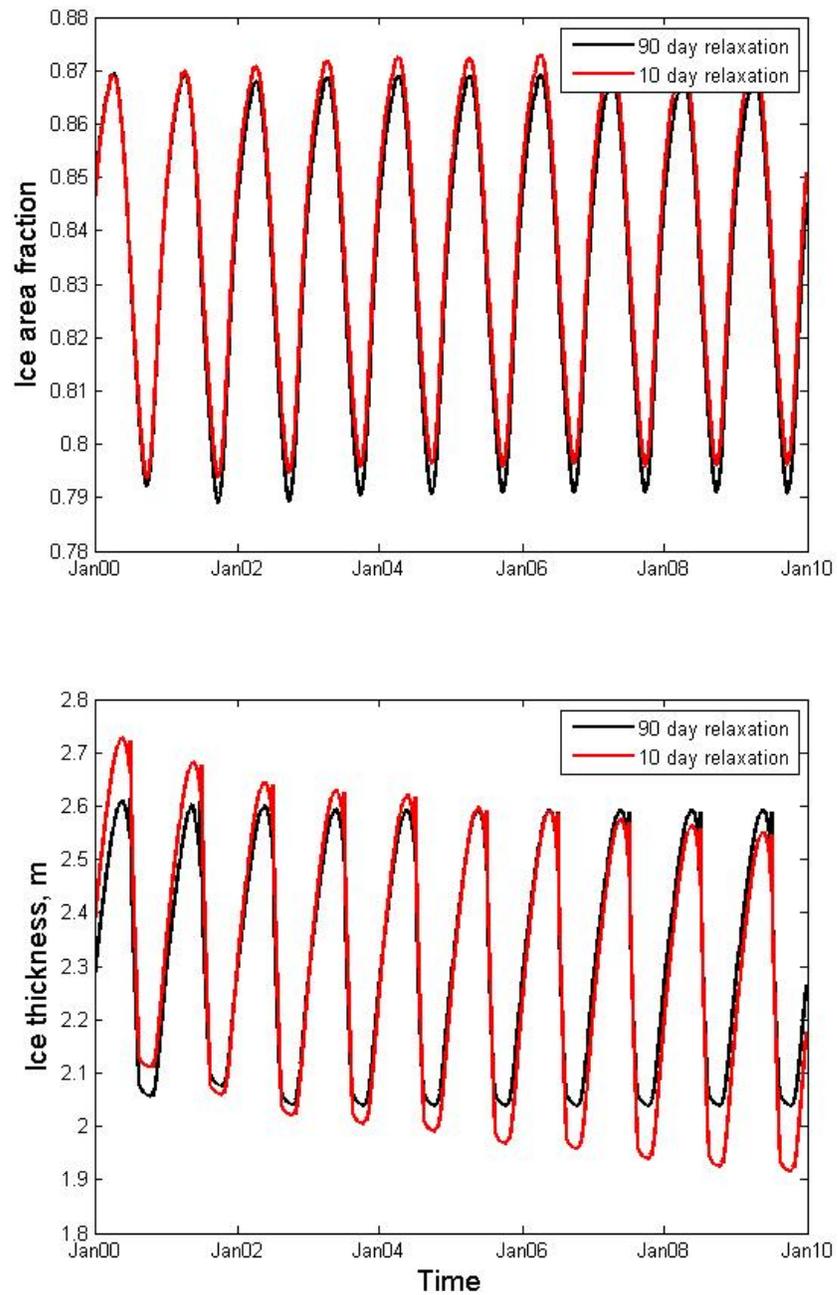
Figure 4.31: Sea ice area fraction and thickness (m) for relaxation times of 10 days (blue) and 90 days (black.)

4.3.5.3   Ocean ambient profiles

Changing the relaxation time altered the time that the ocean required to return to the ambient values, and had a significant effect on the mixed layer properties. Here, we vary the ambient profiles of temperature and salinity in the ocean instead, to investigate the impact that a weaker or stronger density profile has. For the 'weak' ambient scenario, we lower the deep ocean salinity, and for the 'strong' ambient scenario, we raise it. We keep the temperature profile the same for each simulation. The resulting profiles, along with the reference case's ambient profiles and the resulting density profiles, are shown in Figure 4.32.

Figure 4.32: Ambient ocean temperature (K) and salinity (psu) profiles, and the resulting ambient density profiles, for the reference case, the 'weak' case, and the 'strong' case.

We expect to see a reduction in mixed layer depth for stronger ambient profiles. Figure 4.33 shows that this is indeed the case; the strong ambient scenario sees a mixed layer that is roughly 5 to 10 m shallower at the maximum point. The reference case lies between weak and strong ambient scenarios, although it follows the prior more closely than the latter.

Plotting the density through the ocean water together with the mixed layer highlights that there is indeed a distinct difference in the density of the water below the mixed layer in each case, with the highest density in the strong ambient case and the lowest density in the weak ambient case. This limits entrainment more and less strongly respectively.
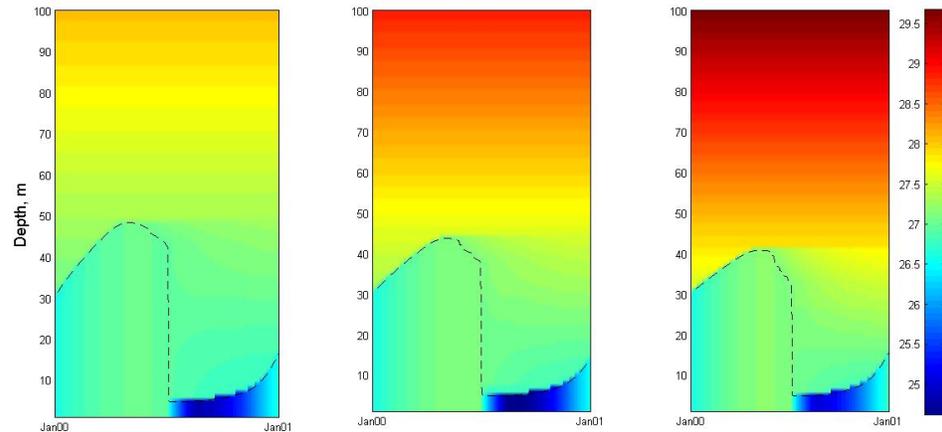
Figure 4.33: Ocean water density (kg m^{-3}) with depth over one year for the weak, reference, and strong cases. The corresponding mixed layer depth (m) is superimposed.
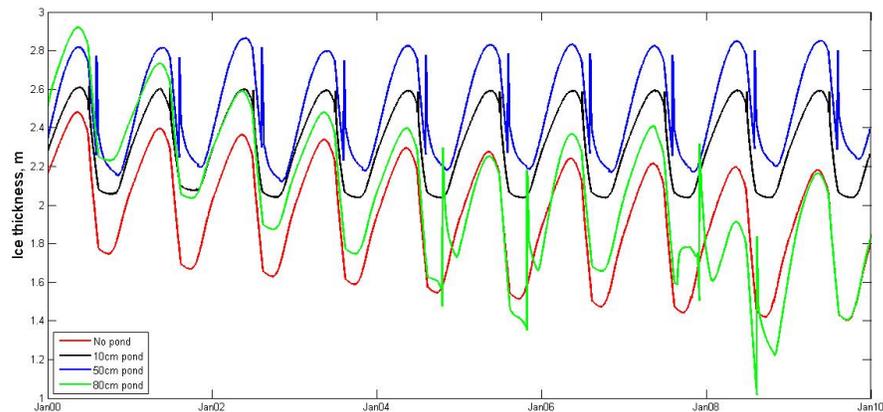
4.3.5.4 Pond depth

We changed the critical under-ice melt pond depth at which the false bottom is assumed to be present from 10 cm to deeper values of 50 cm and 80 cm, which are more representative of the typical under-ice melt pond depths described in Hanson [1965] and Martin and Kauffman [1974]. In this subsection, we present the first year of the simulation as well as the results of the ten year period after the spin-up period, to clearly show both the short-term differences between the scenarios and any compound differences in the long-term trends.

In the first year (Figure 4.34 Subfigure (a)), we see that it takes longer for the under-ice melt pond to reach the critical depth when it's set to 50 cm compared to 10 cm, delaying the switch to Stage 2 of the simulation, and also of the transfer of the under-ice melt pond's fresh water to the ocean. No false bottom forms in the 80 cm pond case, and it instead follows the same path as the slab case. In Subfigure (b), we see that the deep pond depth of 50 cm yields the thickest sea ice on average, and the no-pond scenario yields the lowest average ice thickness, with critical 10 cm pond depth lying between the two. For a critical pond depth of 80 cm, the pattern seems to break down. It appears that it is consistently difficult to meet the critical pond depth in this last simulation.
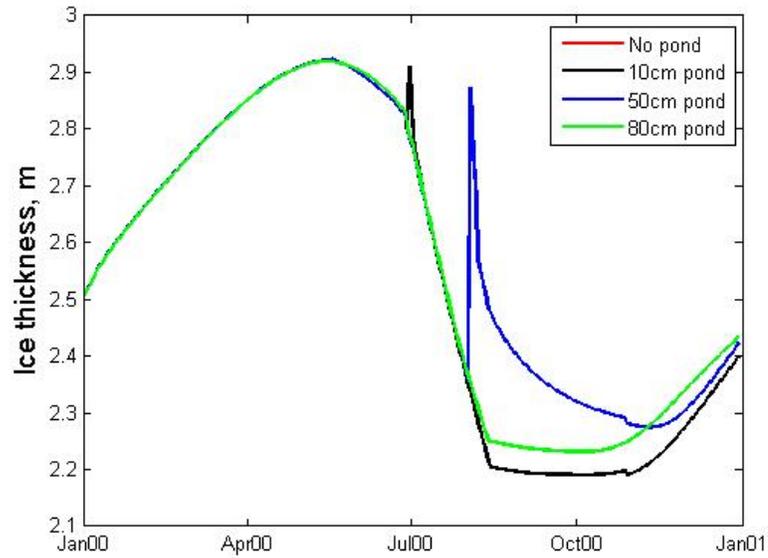
(a)

(b)

Figure 4.34: Sea ice thickness (m) for one spin-up year (a) and for ten years, after a spin up period of three years (b), for critical pond depths of 10, 50, and 80 cm, as well as for a slab of sea ice ('No pond'). Note that the 80 cm pond depth case lies directly on top of the slab case in the first year as the 80 cm pond criteria is not met and the ice continues as a slab only.)

This is confirmed by looking at the under-ice melt pond depths achieved for each critical value, as shown in Figure 4.35. The magenta line shows the critical pond depths for each subplot, representing 10 cm, 50 cm, and 80 cm values from top to bottom, alongside

the achieved under-ice melt pond depth for each corresponding simulation. While the fresh water layer consistently attains the critical depth for the 10 cm and 50 cm values, it is very rare that 80 cm of fresh water accumulates. This means that the majority of years are effectively run with the slab model, pushing it onto the lower ice-thickness track. We see that deep fresh water layers have formed, with thicknesses well into the 60s and 70s of cms, and have been present for significantly longer than the 12 days needed to form a false bottom in Chapter 1. Setting the critical pond depth too high can not only delay the formation of a false bottom from a more realistic time, but can also overlook the presence of false bottoms entirely. We therefore omit the 80 cm pond depth from the rest of this section's analysis.
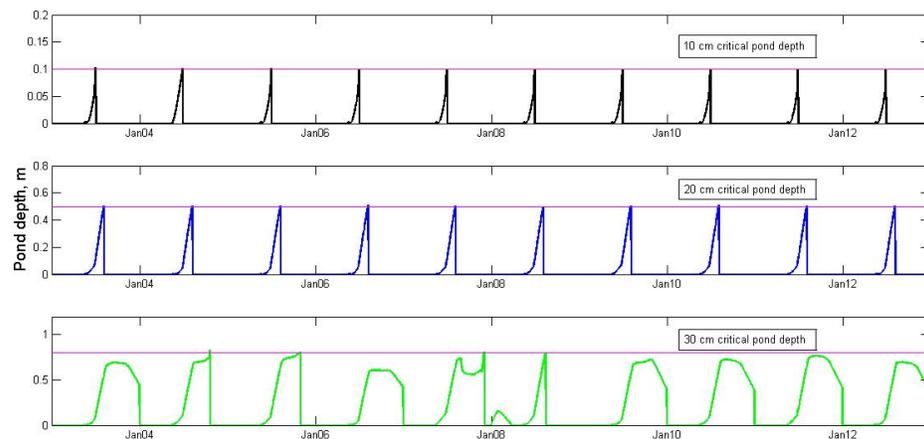
Figure 4.35: Fresh water layer depth (m) before a false bottom forms for ten years, after a spin up period of three years, for critical pond depths of 10, 50, and 80 cm, as well as for a slab of sea ice.

Figure 4.35 also shows an expected delay in the formation of the false bottom and the beginning of the refreezing/ablation process at the base of the sea ice. In Chapter 3, we began the analysis at the start of September. The results here suggest that this is representative of deeper pond depths, but is a realistic start time for the evolution of false bottoms. We see false bottoms forming between July and September, and even later in the year for the strictest critical depth condition, consistent with the field observations of Hanson [1965].

Examining the difference in thickness, the mixed layer depth is significantly shallower at its winter maximum for the deep critical pond depth of 50 cm (25-30 m) than

both the no-pond scenario (50-55 m) and the 10 cm pond scenario (45 m) (see Figure 4.36, Subfigure (b)). The higher critical pond depth leads to a strong delay in the reduction of the mixed layer depth. It reduces from its spring-time values of 30s and 40s of metres to a summer minimum of 5 m, which can be clearly seen in Subfigure (a) of Figure 4.36. This difference in mixed layer depth could be due to the delayed release of a greater amount of fresh water in the 50 cm critical pond depth case. We look at the mixed layer salinty next to confirm this.
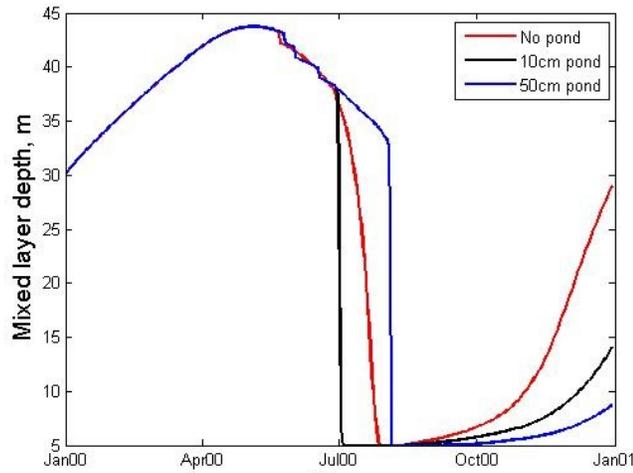
(a)

(b)

Figure 4.36: Mixed layer depth (m) for (a) one year with no spin-up period and (b) ten years, after a spin up period of three years, for critical pond depths of 10, 50, and 80 cm, as well as for a slab of sea ice.

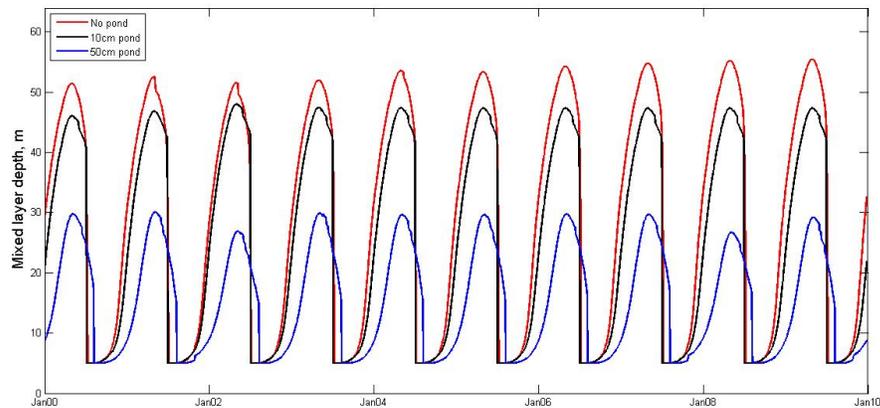The mixed layer salinity is indeed lowest for this deep pond simulation, reaching a summer minimum of around 29.5 psu as opposed to roughly 31.5 for the other two simulations (see Figure 4.37 Subfigure (b).) This matches the shallower mixed layer depth in this deep-pond scenario. The salinity also reaches a peak around 0.5 psu less than the other two simulations. In Subfigure (a), we clearly see the delayed ablation while the false bottom forms in the deep-pond scenario and the strong subsequent freshening of the mixed layer.
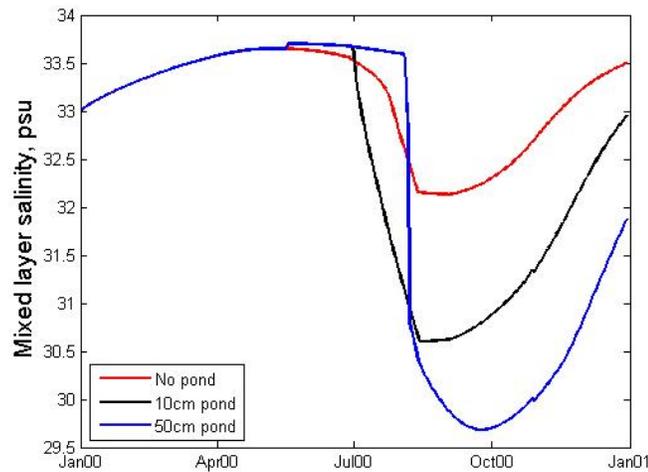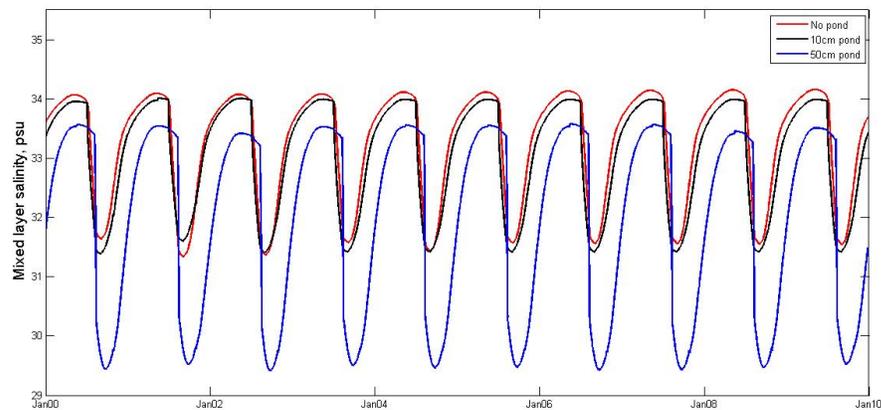

(a)

(b)

Figure 4.37: Mixed layer salinity (psu) for (a) one year with no spin-up period and (b) ten years, after a spin up period of three years, for critical pond depths of 10, 50, and 80 cm, as well as for a slab of sea ice.
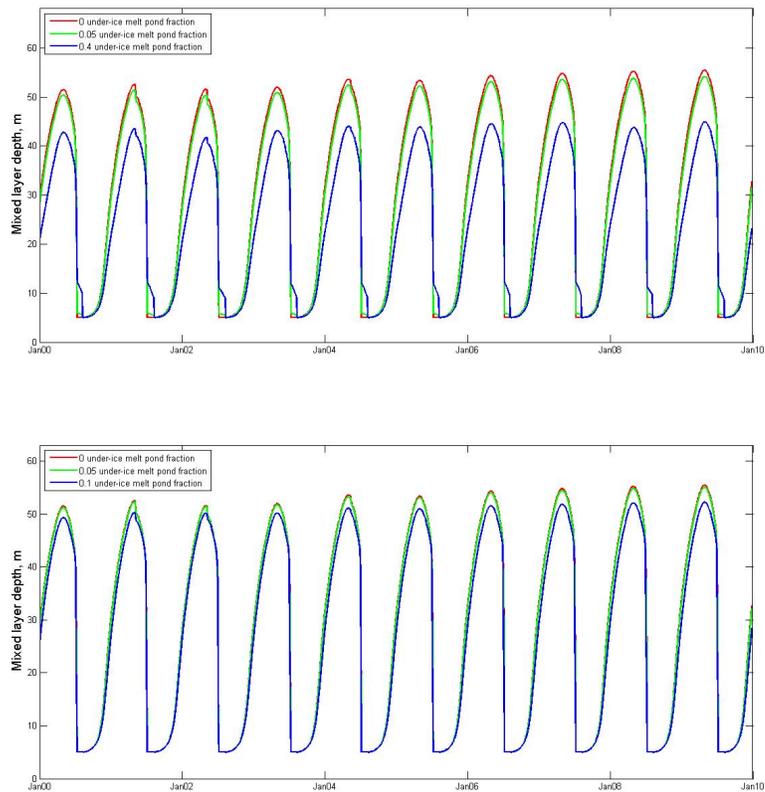
Figure 4.38: Estimated mixed layer depths (m) for an under-ice melt pond fraction of 0, 0.05, and 0.4 for (upper) 50 cm deep under-ice melt ponds and (lower) 10 cm deep under-ice melt ponds.

The mixed layer depth appears to be strongly sensitive to the pond depth, and areas of deep under-ice melt ponds could significantly shallow the mixed layer and reduce its salinity. Linearly combining the mixed layer properties of the no-pond and 50 cm critical pond depth simulations according to under-ice melt pond fraction gives a rough upper estimate of the magnitude of this difference. In Figure 4.38 (upper), we see mixed layer depths for under-ice melt pond fractions of 0 (red), 0.05 (green), and 0.4 (blue), corresponding to a no-pond control scenario, and the lower and upper-bounds of under-ice melt pond fraction suggested by the literature. The area between the green and blue time series therefore represents the depths that the mixed layer could take when under-ice melt ponds are taken into account. For a high fraction of 0.4, the mixed layer could be almost 10 m shallower than if no under-ice melt ponds were present. Even selecting the reference case's critical pond depth of 10 cm, we see that the mixed layer is several

metres shallower in the under-ice melt pond case (see Figure 4.38 (lower).

4.3.5.5   Under-ice melt pond salinity

In this section, we test the model's response to an increase in the under-ice melt pond's salinity from 5 psu (reference case) to 15 psu. We saw previously, during the sensitivity studies of Chapter 3, that increasing the under-ice melt pond's salinity causes it to persist for longer and, therefore, increase the thickness of the sea ice further. We now investigate the effect that this has on the interaction between the sea ice and the mixed layer.
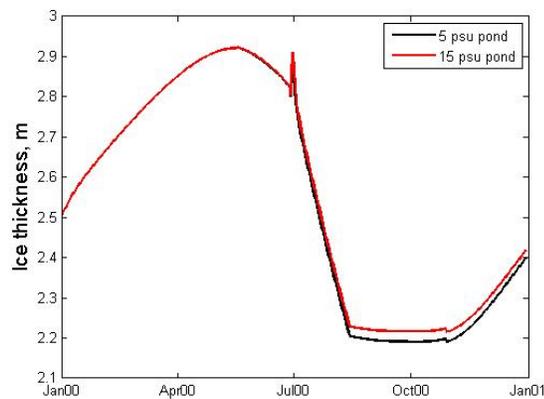
(a)
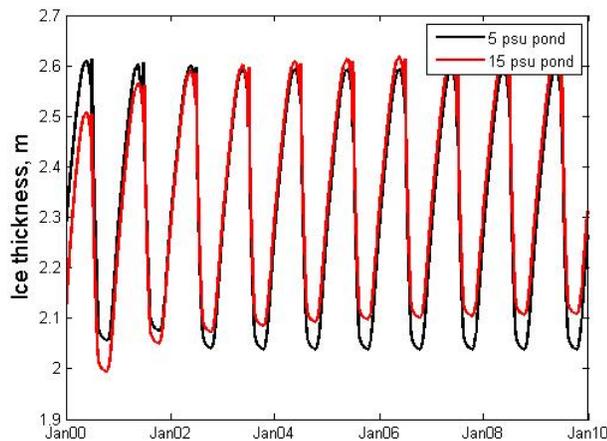
(b)

Figure 4.39: Sea ice thickness (m) for (a) one year with no spin-up period and (b) ten years, after a spin up period of three years, for initial under-ice melt pond salinities of 5 and 15 psu.
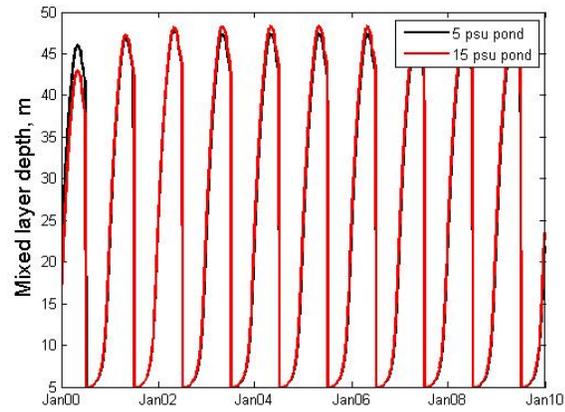
(a)
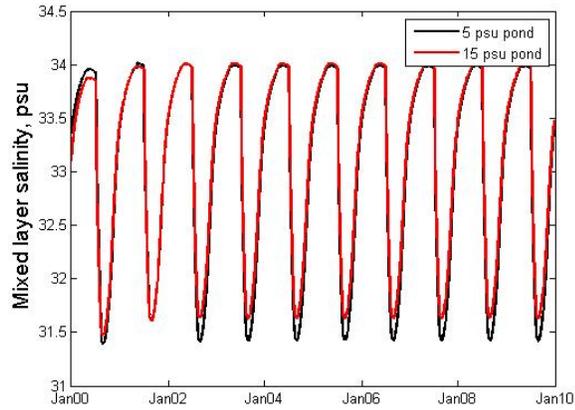
(b)
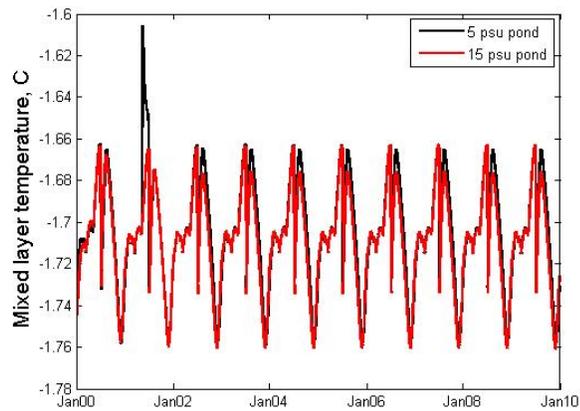
(c)

Figure 4.40: Mixed layer depth (m) for (a) one year with no spin-up period and (b) ten years, after a spin up period of three years, for initial under-ice melt pond salinities of 5 and 15 psu.

In Figure 4.39, we see that the ice is marginally thicker in the salty-pond case during the first year once the false bottom has migrated upwards; while the two cases behave in very similar ways, the basal ablation of the sea ice slows at a slightly higher thickness in the saltier pond case. It is generally thicker in the ten-year time series following the spin-up period. During the spin-up period, the ice has apparently thinned more in the 15 psu case than in the 5 psu case, but it steadily becomes thicker again during the primary ten-year period, eventually overtaking the 5 psu case sea ice in both the winter maximum and the summer minimum. The largest difference is at the latter of the two extremes, when the 15 psu case's sea ice is about 7 cm thicker than that of the 5 psu case.

Since this difference occurs at the summer minimum, it has little affect on the mixed layer depth, since it is at its minimum allowed value anyway. This does, however, make the 15 psu scenario's mixed layer around 0.2 psu saltier during the summer, though. Very little difference is seen in the mixed layer temperature.

Despite this relatively large difference in pond salinities, the two scenarios behave very similarly in the coupled model. The saltier pond leads to marginally thicker ice and a correspondingly saltier mixed layer. There is a strong seasonal shallowing at the point of largest difference, minimising any extra entrainment due to the increase in density of the mixed layer due to the additional salt.

4.3.5.6   Sea ice thickness

When testing the sensitivity of the model to the thickness of the sea ice, we ran the simulations for one year only, since the use of a long spin-up period would negate many of the effects. While we do not expect long-term effects from starting the simulation with different thicknesses of sea ice, it could have a short-term impact as it did in Chapter 3.

We test initial sea ice thicknesses of 1 m to 2.5 m in 0.5 m increments. The ice thicknesses over the course of the year are shown in Figure 4.41. By the end of the year, the difference between them is already lessening. The reference simulation, starting at 2.5 m of sea ice, loses around 10 cm of ice by the end of the year, while the three simulations initialised with thinner slabs of sea ice all increase in thickness by the end of the simulation. The thinner the sea ice at the start of the simulation, the more it grows; the 1 m of sea ice grows by around 60 cm.
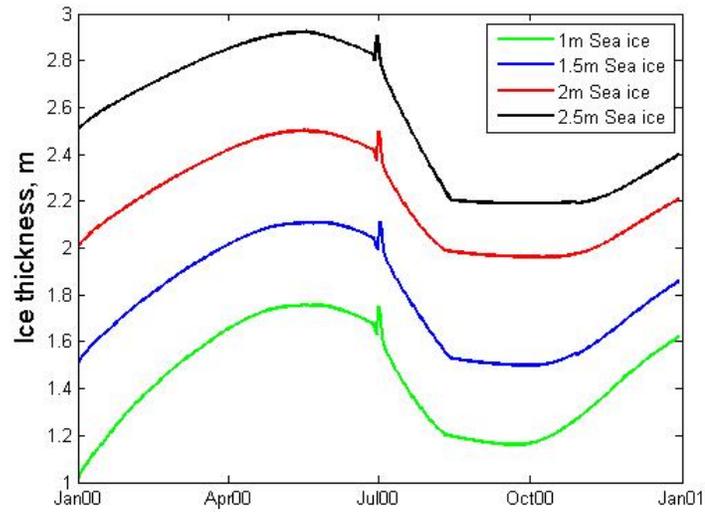
Figure 4.41: Sea ice thickness (m) over one year for initial sea ice thicknesses of 1, 1.5, 2, and 2.5 m.
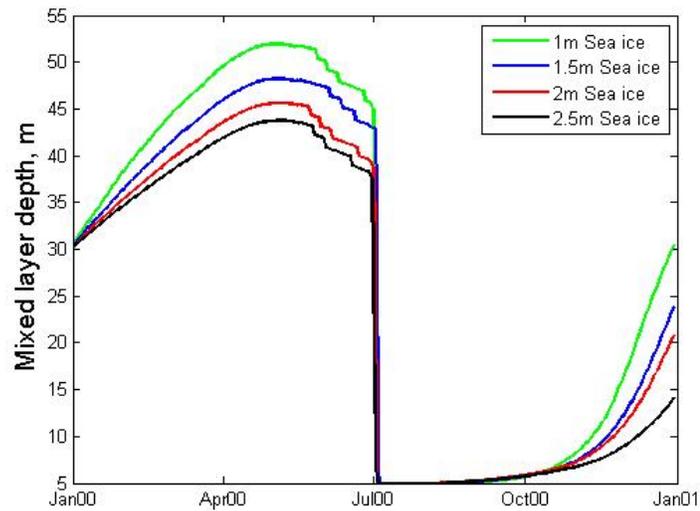
Figure 4.42: Mixed layer depth (m) over one year for initial sea ice thicknesses of 1, 1.5, 2, and 2.5 m.

The mixed layer is significantly deeper for the thinner the sea ice cases, which is consistent with the difference in the evolutions of the sea ice between the different thickness cases (see Figure 4.42.) In the thinner sea ice cases, less fresh water is released during

the summer melting and more salt is rejected during the larger amount of freezing in the winter. This difference in mixed layer salinity is apparent in Figure 4.43. There is some slight overlap at the summer minimum in salinity before returning to the typical pattern.
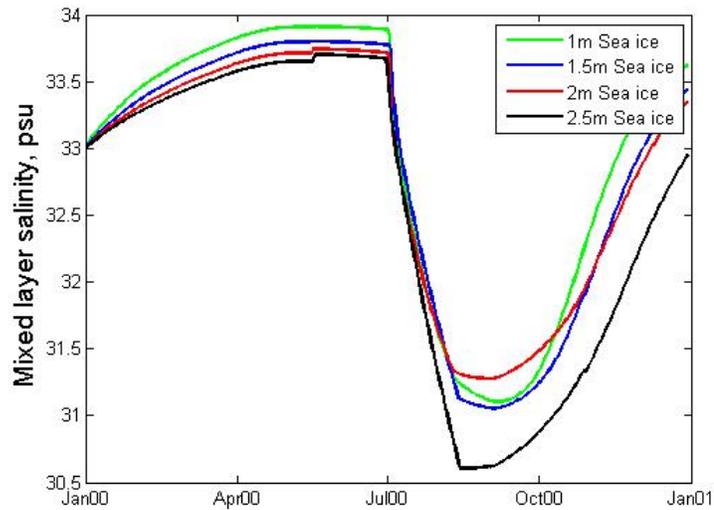
Figure 4.43: Mixed layer salinity (psu) over one year for initial sea ice thicknesses of 1, 1.5, 2, and 2.5 m.
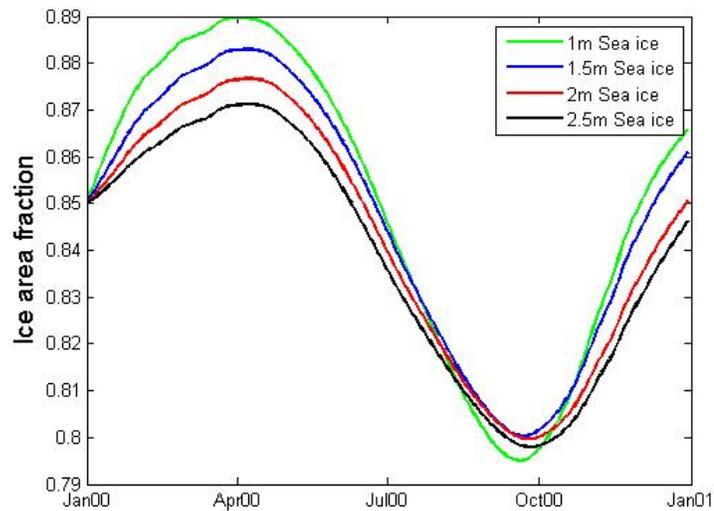
Figure 4.44: Sea ice area fraction over one year for initial sea ice thicknesses of 1, 1.5, 2, and 2.5 m.

The reason for this deviation from the trend in mixed layer salinity decreasing with initial sea ice thickness is shown by looking at the sea ice area fractions for the four simulations. The pattern in the sea ice area matches the change in salinity in this summer period, indicating a stronger seasonal cycle in the lateral growth and melt of the thinner ice case. The differences in lateral melt and freezing between the cases are clearly reflected in the mixed layer salinity.

4.3.5.7   Surface melt ponds
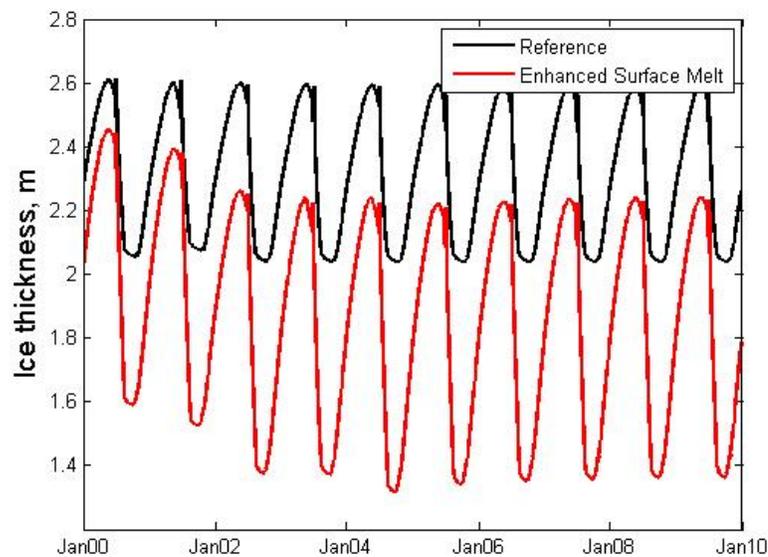
Figure 4.45: Sea ice thickness (m) over one year for the reference case and the enhanced surface melt case.

So far, we have not modelled surface melt ponds, only choosing to drain any surface melt through the ice either into the mixed layer or the fresh water layer depending on the scenario. We chose not to include a complex surface melt pond model in order to be able to more clearly distinguish the impact of the under-ice melt pond on its surroundings but, among other effects, the presence of a surface melt pond would affect the surface albedo. This could significantly increase the amount of summer melt. We lower the surface albedo to 0.4 if surface melt is occurring to simulate this, chosen as an upper estimate from Hanesiak et al. [2001].
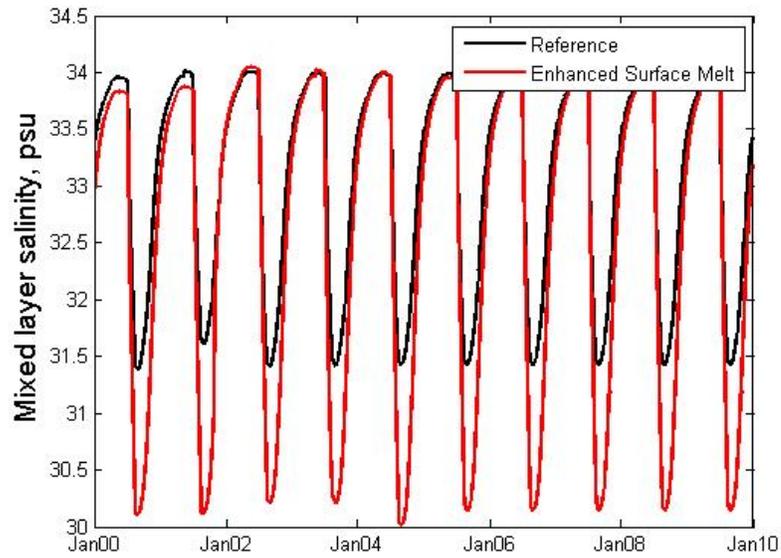
Figure 4.46: Mixed layer salinity (psu) over one year for the reference case and the enhanced surface melt case.
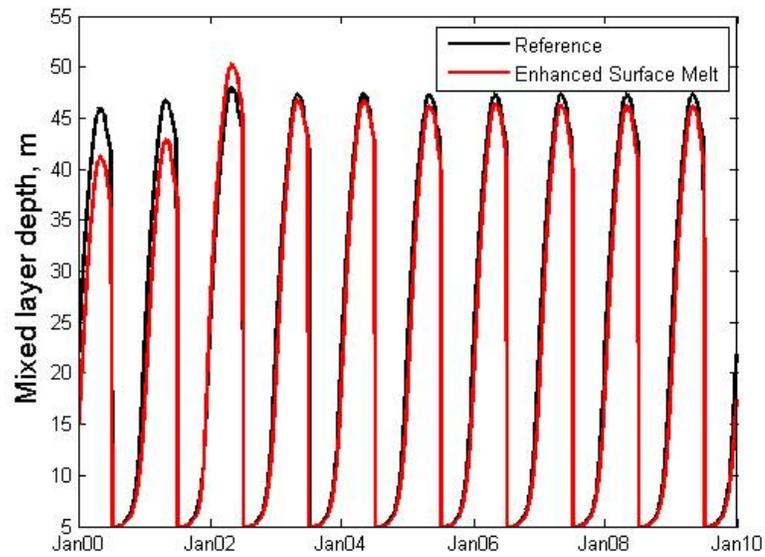
Figure 4.47: Mixed layer depth (m) over one year for the reference case and the enhanced surface melt case.

In Figure 4.45, we see that the sea ice indeed decreases in thickness to a much lower steady state in the enhanced surface melt case. This corresponds to a much lower sum-

mer salinity due to the relatively high release of fresh water in the melt season, as shown in Figure 4.46.

Since the majority of the difference occurs in the summer melt season when the mixed layer is already at its minimum allowed depth, we do not see a very stark difference in mixed layer depth (see Figure 4.47.) During the rest of the year, the mixed layer is slightly shallower in the enhanced surface melt case, as expected. The reduction in ice thickness is also compensated for slightly by enhanced lateral growth of the sea ice. In Figure 4.48, we see that the fresher mixed layer allows for a higher ice concentration in the enhanced melting case.
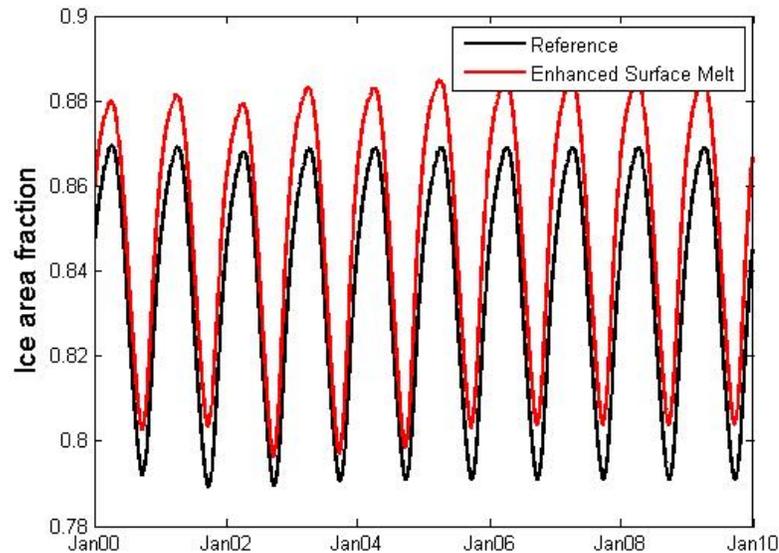
Figure 4.48: Ice area fraction over one year for the reference case and the enhanced surface melt case.

4.4 Conclusions

We have developed a coupled sea ice-ocean model including the formation of an under-ice melt pond, with a parameterisation of the formation of a false bottom associated with it. The model recreates typical patterns in sea ice and mixed layer properties, including seasonal cycles in the ice thickness and area, and the mixed layer depth, salinity, and temperature. Ice growth/ablation increases/decreases mixed layer salinity, and the

mixed layer depth responds as expected to input of salt and heat. Given appropriate choice of critical under-ice melt pond depth before we assume that the false bottom has formed, an under-ice melt pond forms each melt season, and the model is able to attain pond depths that match well with observed values.

Our results using this model suggest that under-ice melt ponds are important to the mass balance of the sea ice, leading to sea ice tens of centimetres thicker compared to the sea ice slab model. More so, key properties of the oceanic mixed layer beneath under-ice melt ponds appear to be strongly influenced by the evolution of these fresh-water layers. The migration of a false bottom upwards rapidly transfers stored fresh water to the mixed layer, significantly freshening and shallowing it. If a significant fraction of the sea ice is underlain by under-ice melt ponds, the mixed layer could up to around 10 m shallower due to the evolution of associated false bottoms. This makes the phenomena of consequence to the ocean below them, as well as to the sea ice above.

This is largely due to the rate of transfer of fresh water to the mixed layer. The storage of melt water beneath the ice temporarily increases the mixed layer depth compared with the gradual conveyance of fresh water into the mixed layer throughout the melt season, but the subsequent migration of the false bottom upwards rapidly transfers fresh water to the ocean leading to a sharp, stronger freshening and shallowing of the mixed layer beyond the cumulative effect of a gradual fresh water drainage.

Having tested the model's sensitivity to a number of parameters, we see that it is particularly reactive to changes in the background values of ocean temperature and salinity via different choices of ambient profiles and relaxation times. Shorter relaxation times or stronger ambient density profiles lead to shallower mixed layers. Within the limits of the reasonable critical pond depths, this coupled model confirms our previous conclusion that deeper under-ice melt ponds increase the average ice thickness. As well as this, the mixed layer appears to become shallower with increasing pond depth, due to the associated increasingly large release of fresh water in a short period of time. We see a smaller difference in the sea ice and mixed layer properties when we increase the under-ice melt pond salinity. The mixed layer appears to be slightly more saline when we use a high under-ice melt pond salinity, and therefore marginally deeper in the winter.

Chapter 5

Conclusions

Sea ice is important to our climate due to its effect on the planet's albedo, its moderation of heat, mass and momentum fluxes between the ocean and atmosphere, and its impact on the thermohaline forcing of the ocean. In this thesis, we have investigated thermodynamic evolution of sea ice and its interaction with the upper ocean using a range of models. In particular, we have focussed on under ice melt ponds and false bottoms with the specific aim to

1. investigate the impact of under-ice melt ponds and false bottoms on the mass balance of the sea ice;

2. investigate the impact of under-ice melt ponds and false bottoms on the thermohaline interaction between the sea ice and the mixed layer; and

3. assess whether these phenomena warrant including in the sea ice models, such as the sea ice components of climate models.

In this final chapter, we summarise our work and make an assessment to address the aims above. We will also identify areas that our work could be improved upon in the future.

5.1   False bottom formation

We first looked at the formation of the false bottom ice sheets that appear at the interface between the under-ice melt ponds and the ocean below. We simulated the horizontal growth of ice crystals at this interface to estimate the length of time needed for a false bottom to form. We used Matlab's built in `pdepe` routine to solve the nonlinear diffusion equation for the nondimensionalised salinity field and then used a finite difference scheme to find the change in width of the ice crystal with depth. Our model suggests

that a false bottom will be formed after around 12 days, assuming that it freezes with a high solid fraction.

Our resulting crystal profile matches that observed in the cold tank of Martin and Kauffman [1974], as well as the general shape of the profile that was calculated by them. The timescale of the lateral growth stage in our model is also very similar to that observed in the cold room experiment. The gap between the ice crystals was bridged in 12 days for a given solid fraction of 0.98, comparable with the experimental value 14 days. Time for the initial convection, vertical crystal growth, and the consolidation of the ice crystals into a solid false bottom ice sheet is not accounted for in our model, and we are assuming that our chosen crystal separation of 5 cm is representative of the average crystal separation, possibly accounting for this small difference.

The main difference between our model and that of Martin and Kauffman [1974] is that we solve the full nonlinear system for salt diffusion, whereas Martin and Kauffman [1974] linearise the nonlinear diffusion equation and solve for an approximation of the full nonlinear system. Comparing our results to theirs, we see that the two models match well in terms of shape. Our solution for crystal profile using the nonlinear system grows slightly more quickly at the maximum width, and slightly less quickly above and below it. This means that it forms a false bottom more quickly, and possibly that the resulting false bottom is thinner, for the nonlinear model. When we apply the same techniques to solve the linearised system, then our results match very closely.

5.2   Under-ice melt pond and false bottom evolution

In order to determine the effect of under-ice melt ponds on the mass balance of the sea ice, we created a one-dimensional thermodynamic model of a slab of sea ice sitting above an under-ice melt pond with a false bottom. We assumed that the false bottom was fully formed and allowed the ice-water boundaries to evolve according to Stefan conditions. We solved the mushy layer equations for two-phase media for temperature in the sea ice and false bottom layers using Matlab's `pdepe` routine.

We were able to successfully replicate the evolution of a false bottom in the field study of Hanson [1965], in which a false bottom migrated upwards through an 80 cm deep under-ice melt pond. The boundary positions of the false bottom and the base of

the sea ice followed similar trajectories in their diagram and our simulation over a 30 day period. We then carried out sensitivity studies, comparing the outputs of our under-ice melt pond simulations to those of a model of an identical slab of sea ice without an under-ice melt pond. We found that under-ice melt ponds and false bottoms insulate the sea ice from the ocean below, leading to thicker ice compared to the slab case simulations. As well as this, we found that false bottoms either freeze through the entire under-ice melt pond or ablate before they are able to do so. There has been a lack of observations of the full evolution of false bottoms, and most of the literature observes only that they migrate upwards through the pond and thicken over time, so it is interesting to note these two possible final outcomes.

Our sensitivity studies indicate that thinner parent sea ice gains less ice as a result of the presence of an under-ice melt pond compared to thicker parent sea ice, due to the more rapid freezing of the pond and a therefore shorter period in which the sea ice is insulated from below, and relatively faster growth of the slab case sea ice in the absence of the pond. The gain in ice thickness as a result of the presence of an under-ice melt pond also increases with its salinity, as it prolongs the evolution of the under-ice melt pond.

Under some simplifying assumptions, our results suggest that the presence of under-ice melt ponds could lead to an increase in sea ice volume of between 0.3 and 3.2%. This is not significantly high, though their effect could be locally significant, for example to certain regions where the phenomenon appears fairly common, such as the seasonal marginal ice zone. This work also neglected the interaction between the sea ice (or false bottom) and the ocean, and did not take into account the formation of the under-ice melt ponds and false bottoms, nor any cumulative effect should they form year after year. We addressed these issues in the following chapter of the thesis.

5.3   Under-ice melt ponds and the mixed layer

To investigate the impact of under-ice melt ponds and false bottoms on the thermohaline interaction between the sea ice and the mixed layer, we coupled our under-ice melt pond model to a simplified, zero-dimensional model of the oceanic mixed layer. We implemented a Kraus-Turner-type mixed layer model, after Petty et al. [2013], in which the

temperature and salinity of the oceanic mixed layer influence the basal ablation/growth of the sea ice. In return, any melting of the sea ice or salt rejected during freezing changed the salinity, temperature and depth of the mixed layer, and the thickness of the sea ice influenced the amount of solar radiation reaching the mixed layer. In this section, we also considered lateral melt/freezing of the sea ice via a sea ice area fraction. As well as the effects of salt rejection/freshening during lateral ice growth/melt, the horizontal extent of the sea ice affected the amount of fresh precipitation able to reach the ocean.

In Chapter 4, we considered all stages of the evolution of false bottoms and under-ice melt ponds. We started each simulation with a slab of ice, and assume that 80% of any surface melt goes to forming an under-ice melt pond. Using our results from Chapter 2, we assumed that once this pond had reached a certain critical depth and had had non-zero depth for at least 12 days, then a false bottom forms with solid fraction 0.98. We then used the model of Chapter 3 to simulate the evolution of the formed false bottom, under-ice melt pond, and sea ice, and switched to the slab model again once the false bottom had either reached the base of the sea ice or ablated. If it ablated, the fresher water of the under-ice melt pond was released into the mixed layer. If the initial criteria to form an under-ice melt pond was not met then that year was instead run with the slab model.

We were able to recreate typical seasonal patterns in properties of both the sea ice and the mixed layer, with higher ice thickness and area fraction in the winter and a corresponding deeper, cooler, more saline mixed layer. We found that the addition of the mixed layer model increased the difference in ice thickness between the slab and the under-ice melt pond scenarios, meaning that our previous measure of the impact of under-ice melt ponds on the mass balance of the sea ice was an under-estimate. In our multi-year reference simulation, the sea ice was around 40 cm thicker at the end of the 10 year period in the under-ice melt pond case compared to the slab case: a significant increase in sea ice thickness. The evolution of under-ice melt ponds tended to transfer the large amount of stored fresh water to the ocean over a relatively short period of time, strongly freshening the mixed layer. This lead to a mixed layer roughly 10 m shallower in the winter period. This is a large percentage difference (roughly 20% shallower) given that the mixed layer winter maximum depth was of the order of 50 m in the slab case.

By changing the critical pond depth required for the formation of the false bottom,

we were able to replicate under-ice melt ponds of up to 80 cm, like those observed in Hanson [1965]. We found that raising this critical pond depth increased the gain in sea ice thickness up until the point that the value becomes too large for the under-ice melt ponds to consistently form each year (i.e. 80 cm). In these cases, it is assumed that no false bottom forms and instead the year is simulated with the slab model instead. Scaling with potential under-ice melt pond fractions, these results suggested that for a pond initially 50 cm deep, we estimate the oceanic mixed layer to be 10 m shallower across the Arctic compared with simulations that ignore the presence of under-ice melt ponds.

5.4 Limitations of our models

Our sea ice model currently does not support the formation of a snow layer at the top of the sea ice. In Chapter 4, we incorporate precipitation directly into the mixed layer should it fall onto exposed ocean. However, we do nothing with the precipitation falling onto the sea ice. In reality, there may be some lateral run-off into the ocean and accumulation on the surface of the sea ice. Even considering this, the freshening effect of precipitation was relatively small in our study, and so this is unlikely to impact our results in a significant way. It could, however, lead to an interesting study on the effect that under-ice melt ponds have on the transport of pollutants through the sea ice and the location of their eventual release, as suggested by Eicken [1994].

When determining whether or not a false bottom is able to form, we checked first whether the fresh water layer had reached its critical depth and secondly whether fresh water has been present beneath the sea ice for at least 12 days, the length of time that we found necessary for a false bottom to form in Chapter 1. This worked well for shallower pond depths, but broke down when we tested the higher critical depth of 80 cm. In this case, the fresh water layer regularly maintained depths of greater than 70 cm for more than 12 days, but because the critical depth condition was not met it was assumed that no false bottom formed. It would therefore be desirable to employ a more comprehensive false bottom formation condition to take into account situations such as this. This does not affect our results except for the one 80 cm critical depth case discussed here, but would need to be addressed in any future studies looking at ponds deeper than 50 cm.

The further development of the model to more fully account for any surface melt pond on the sea ice at the top of the domain and its drainage through the sea ice could also improve the model. In Chapter 4, we included an enhanced albedo when surface melting was occurring, as a stand-in for a full surface melt pond model, but a full thermodynamic model of a refreezing surface melt pond would alter the temperature profile within the sea ice and, therefore, any ablation or growth at the base of the sea ice, as Flocco et al. [2015] showed. This could strengthen our results, in that it could increase the length of time that the under-ice melt pond persists and insulates the sea ice, and could lead to less basal growth in the slab case.

While our model accounts for the effect of salt rejection within the under-ice melt pond, the surface melt pond model of Flocco et al. [2015] was sensitive to the inclusion of solutal boundary layers at the ice-pond interfaces to deal with this continuous input of salt into the surface melt pond. These layers are less than millimetres thick, and so are not resolved by our standard diffusion model. Although unlikely to lead to a considerable qualitative change in our key results, this could increase the longevity of under-ice melt ponds in our model, as well as the final state of the false bottom in borderline cases.

Similarly, we do not account for the presence of ice crystals within the under-ice melt pond. We did not model the nucleation of the thin crystals observed on the base of the sea ice, nor their subsequent vertical growth downwards to the interface between the fresh water and the ocean. Divers have noted that these crystals account for around 10% of the interior volume of under-ice melt ponds, and they could change convection and the transfer of heat within the under-ice melt pond. They are also not considered in the evolution of the false bottom, which they formed and are presumably still connected to. Accounting for these crystals more fully could have a small effect on heat fluxes within the pond and false bottom formation time, but is negligible compared to the other mechanisms at work in our system.

In Chapter 4, we assume that no mixing between the under-ice melt pond and the ocean occurs while the false bottom is forming. In order for under-ice melt ponds to form, there needs to be little mixing with the ocean so that the fresh water can accumulate. This appears to usually be due to the presence of physical barriers to mixing, such as a hollow beneath the sea ice [Martin and Kauffman, 1974]. These often form beneath surface ponds due to the lower albedo of these patches of ice. The formation of false

bottoms also requires at most low levels of mixing, so that there remains significant temperature and salinity gradients between the under-ice melt pond and the ocean. Since these phenomena have been observed in the field, we know that the no/low-mixing scenario must be possible. It is therefore a reasonable assumption that no mixing occurs during in this period in our model, else a false bottom would not form.

We used a constant wind speed in our simulations, so as to rule out the impact of individual strong or low wind events on mixed layer depth. However, in reality wind velocity would have an effect on not only the mixed layer depth but also the transfer of heat between the ocean and the sea ice. Since there is little seasonality in the wind strength in the Arctic, then this is unlikely to affect the impact of under-ice melt ponds. However, other applications of the model, for example, case studies during extreme weather events such as that considered by [Notz et al., 2003], it may become important.

Finally, we do not take into account the lateral freezing of the under-ice melt pond, only the vertical. By assuming horizontal homogeneity, we assume a fixed sea ice thickness and under-ice melt pond depth across the breadth of the domain. In reality, if the fresh water is collecting in hollows in the topography of the base of the sea ice, then some lateral freezing at the edges of the concavity is likely to occur. This could reduce the amount of time taken for the under-ice melt pond to freeze, and could also change the final state of the false bottom in borderline cases.

5.5 Required measurements

Further observations are required in order to more accurately gauge the impact of under-ice melt ponds on the sea ice and its thermohaline interaction with the oceanic mixed layer, to more thoroughly validate our results, and to parameterise these effects for use in more complex sea ice models, such as the Los Alamos National Laboratory sea ice model. Firstly, measurements of the fraction of the base of the sea ice that is under-lain by under-ice melt ponds and, secondly, of the depths of under-ice melt ponds would be useful in determining the magnitude of the increase in ice volume and the shallowing of the mixed layer due to the presence of under-ice melt ponds. Measurements of mixed layer properties at sites where under-ice melt ponds are prevalent would also be useful for model validation. Our results indicate a rapid freshening and shallowing of the

mixed layer below an under-ice melt pond during the upwards migration of its false bottom. A strikingly similar incident was noted during the AIDJEX experiment Notz et al. [2003]: a sudden freshening of the ocean water below established under-ice melt ponds was noted following the sudden ablation of their false bottoms. A reversal of the direction of the heat flux between the ice and the ocean was also noted, comparable to the jump that we see in our model's results when the mixed layer suddenly shallows. Additional systematic measurements of false bottom thickness, under-ice melt pond depth and oceanic mixed layer properties during this process could lend further confidence to our theory that under-ice melt ponds have a significant impact on the Arctic ocean mixed layer depth and salinity

Previous observations taken during the Surface Heat Budget of the Arctic Ocean (SHEBA) revealed a lot about the formation and evolution of surface melt ponds and the mass balance of the sea ice and provided a lot of data that has assisted and verified modelling efforts. However, these data were taken in the years 1997-98, and Arctic conditions have changed significantly since then.

The upcoming Multidisciplinary drifting Observatory for the Study of Arctic Climate (MOSAIC) project involves the drift of the RV Polarstern across the central Arctic during 2019-20, taking measurements year-round. The project will provide new atmospheric, sea ice, and marine observations useful for monitoring the Arctic climate, as well as for forcing and validating modelling efforts. Of particular relevance to this thesis, mass and fresh-water balances of the sea ice will be monitored. The topography of the base of the sea ice will be observed by an Remotely Operated Vehicle just below the ice-ocean interface, which will also examine the thermohaline structure in the uppermost levels of the ocean. This could result in the collection of key data, such as under-ice melt pond prevalence and depth, that may further our understanding of the formation and evolution of under-ice melt ponds, just as SHEBA did for surface melt ponds. Up-to-date atmospheric measurements will provide contemporary surface forcings that we could use as input for our model, and daily marine measurements including temperature and salinity will help us to validate our estimate of the impact of under-ice melt ponds on the interaction between the sea ice and the water below. The outcome of the MOSAIC project could allow us to more accurately estimate the impact that under-ice melt ponds have on the sea ice and the oceanic mixed layer.

5.6   The importance of under-ice melt ponds

Our simulations with a sea ice-mixed layer model show that under-ice melt ponds appear to have a significant impact on the mass balance of the sea ice, causing it to be tens of centimeters thicker in our coupled sea ice-mixed layer model. In turn, their evolution transfers a significant amount of fresh water into the mixed layer in a relatively short period of time, freshening and shallowing it.

Depending on factors such as the depth of the under-ice melt ponds and how large a fraction of the base of the sea ice that they cover, their evolution could also lead to significantly shallower mixed layer depths than beneath a slab of sea ice with no such ponds. We linearly combined the outputs of the slab simulations and the under-ice melt pond simulations for the reference case and for the 50 cm critical fresh water depth case in order to estimate the impact that a certain fraction of under-ice melt ponds could have on the mixed layer depth. In the most upper extreme case that we tested (50 cm critical fresh water depth, 0.4 under-ice melt pond fraction), this analysis implies that the mixed layer could be up to 10 m shallower due to the presence of under-ice melt ponds. This is primarily because the migration of false bottoms upwards is also associated with a rapid freshening of the mixed layer.

These results suggest that under-ice melt ponds could have a significant effect on their surroundings in the Arctic, warranting further investigation and inclusion in the sea ice component of climate models. A parameterisation of this subgrid-scale process would be a useful improvement to a sea ice model such as the Los Alamos National Laboratory sea ice model. Further observations of under-ice melt ponds are desirable, particularly of their depths and the fraction of the base of the sea ice that they cover.

Appendix A

Model structure

A.1   Model summary

Coupled sea ice-ocean mixed layer model summary:

1. Set up model: load the required forcings, assign values to the required parameters, set initial conditions on variables

2. For each year, run the three-stage sea ice-mixed layer model. After the first year, use the output from the previous year to initialise the next one. In each timestep:

   (a) Calculate the temperature profile with in the sea ice (Stage 1, 2, and 3) as well as the under-ice melt pond and false bottom (Stage 2)

   (b) Calculate the growth/ablation at the boundaries and update the boundary positions accordingly

   (c) Find the new under-ice melt pond salinity and the corresponding **liquidus** temperatures at the pond-ice interfaces (Stage 2)

   (d) If surface melt takes place, add 80% of its volume to a fresh water layer beneath the sea ice and subtract any basal growth from this layer (Stage 1)

   (e) Solve an energy balance for the temperature at the surface of the sea ice

   (f) Calculate the new mixed layer depth, temperature, and salinity

   (g) Find the liquidus temperature at the interface between the base of the sea ice and the ocean (Stage 1, 2, and 3) or the fresh water layer (Stage 1)

   (h) Feed results back to main workspace

3. Save results and plot figures

The interactions between the functions are illustrated in Figure A.1.
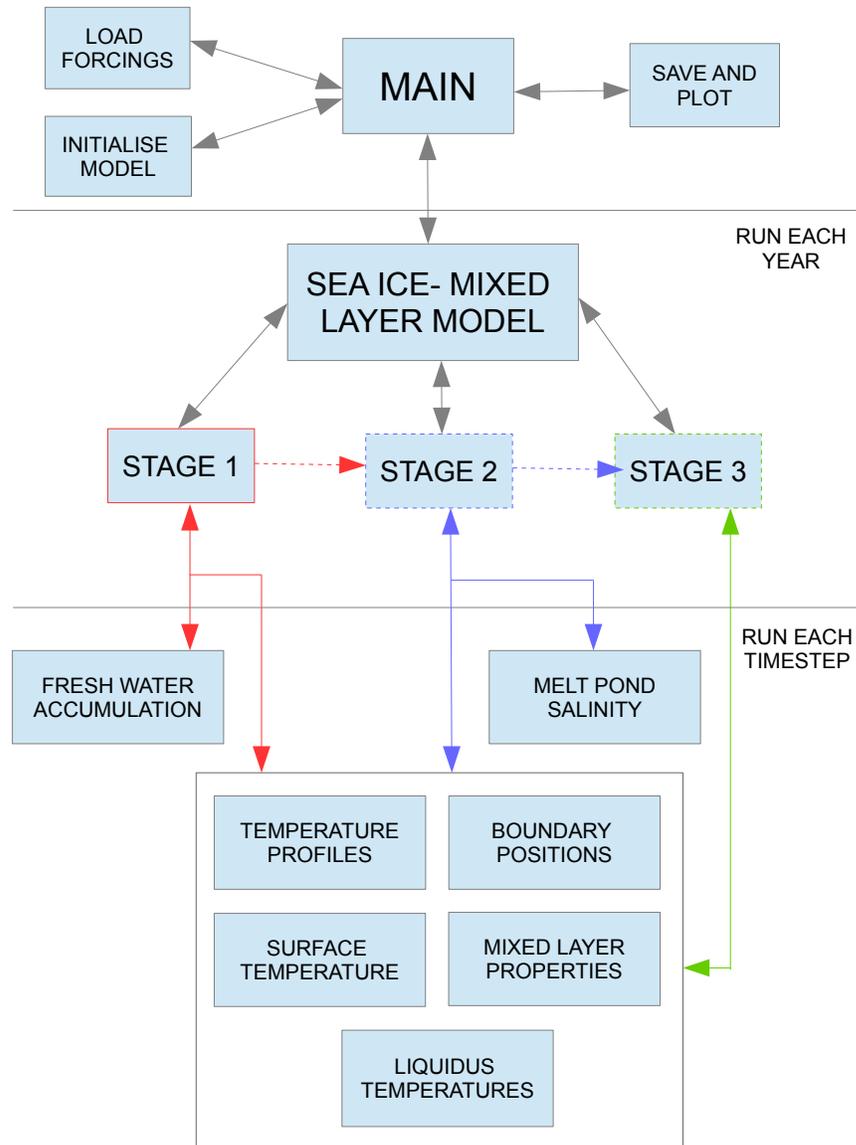
Figure A.1: A schematic showing the interactions between the functions used in the coupled sea ice-mixed layer model. Dashed lines represent optional paths that require certain conditions to be met in order to progress along them.

A.2   Model section descriptions

Boundary positions Solve Stefan conditions for the change in any ice-water boundary positions and update the boundary positions using finite difference schemes.

Fresh water accumulation Add 80% of any surface melt to the depth of a fresh water layer beneath the sea ice and subtract any basal ice growth.

Initialise model Assign values to necessary parameters and set initial conditions.

Liquidus temperature Find the liquidus temperature at the interface between the base of the sea ice and the mixed layer salinity or the fresh water layer if it is present.

Load forcings Import atmospheric forcings.

Main Set up and run the model for the required time interval.

Melt pond salinity Calculate the salinity of the under-ice melt pond and the resulting liquidus temperatures at the pond-ice interfaces.

Mixed layer properties Calculate the powers into the mixed layer and the resulting entrainment rate according to the predictor-corrector approach outlined in Chapter 4. Update the mixed layer depth, temperature, and salinity.

Sea ice-mixed layer model Run the coupled sea ice-mixed layer model for one year, split into the three potential stages defined in Chapter 4.

Stage 1 Run the model for a slab of sea ice with melt water accumulation beneath the sea ice. If the false bottom formation condition is met, move onto Stage 2. Otherwise, run the year with a slab of sea ice and no melt water accumulation.

Stage 2 Run the model for sea ice above an under-ice melt pond and false bottom. If the under-ice melt pond frozen/false bottom ablated condition is met, move onto Stage 3.

Stage 3 Continue running the model with the remaining slab of sea ice from the end of Stage 2. Once the end of year condition is met, output results to main workspace.

Surface temperature Solve the energy balance at the surface of the sea ice for the surface temperature.

Temperature profiles Calculate the temperature within each sea ice grid cell, as well as those of the under-ice melt pond and false bottom if in Stage 2.

Appendix A

Notation and values

A.1   Chapter 2

Notation	Value
a	5 cm
κ	1.4×10^3 cal cm^{-1}s^{-1}C^{-1}
D	7.5×10^{-6} cm^{2}s^{-1}
m	5.3×10^{-20} C
s_1	8.5 ‰
α_1	1.9×10^3
α_2	5.3×10^{-3}
α_3	1

A.2   Chapter 3

Notation	Value
D_m	1.2×10^{-11} m^{2}s^{-1}
$\rho = \frac{\rho_i}{\rho_b}$	1.09
Γ	0.0514 K ppt^{-1}
κ	1×10^{-2} m^{2}s^{-1}
D_{turb}	1×10^{-2} m^{2}s^{-1}
ι	0.4
ϵ	0.99
σ	5.67×10^{-8} J K^{-4}m^{-2}s^{-1}
ρ_{air}	1.3 kg m^{-3}
c_{air}	1004 J kg^{-1}K^{-1}
C_t	1.1×10^{-3}
$\mathcal{L}_v$	3.014×10^{8} J m^{-3}

A.3 Chapter 4

Notation	Value
c_m	0.03 m s^{-1}
c_1	0.8
c_2	0.8
g	9.81 m s^{-2}
α	$5.82 \times 10^{-5} \text{ K}^{-1}$
β	8×10^{-4}
	10
c_{d_i}	0.0013
c_{d_w}	0.001
ρ_a	1.275 kg m^{-3}
ρ_w	1026 kg m^{-3}
u_a	3 m s^{-1}
c_w	$4190 \text{ J kg}^{-1}\text{K}^{-1}$
α_i	0.6
α_w	0.06
ι_i	0.7
ι_w	0.45
k_w	0.1 m^{-1}
k_i	1.5 m^{-1}
$\mathcal{L}$	334000 J kg^{-1}
R_B	0.4
ρ_i	917 kg m^{-3}
c_h	0.006

Bibliography

D. Alexandrov and I. Nizovtseva. To the theory of underwater ice evolution, or nonlinear dynamics of false bottoms. *International Journal of Heat and Mass Transfer*, 51(21):5204–5208, 2008.

V. Alexeev, P. L. Langen, and J. R. Bates. Polar amplification of surface warming on an aquaplanet in ghost forcing experiments without sea ice feedbacks. *Climate Dynamics*, 24(7-8):655–666, 2005.

R. B. Alley, P. U. Clark, P. Huybrechts, and I. Joughin. Ice-sheet and sea-level changes. *Science*, 310(5747):456–460, 2005.

K. R. Arrigo, D. K. Perovich, R. S. Pickart, Z. W. Brown, G. L. Van Dijken, K. E. Lowry, M. M. Mills, M. A. Palmer, W. M. Balch, F. Bahr, et al. Massive phytoplankton blooms under Arctic sea ice. *Science*, 336(6087):1408–1408, 2012.

E. Bailey, D. Feltham, and P. Sammonds. A model for the consolidation of rafted sea ice. *Journal of Geophysical Research: Oceans*, 115(C4), 2010.

F. Berkes and D. Jolly. Adapting to climate change: social-ecological resilience in a Canadian western Arctic community. *Conservation ecology*, 5(2):18, 2002.

W.-J. Cai, L. Chen, B. Chen, Z. Gao, S. H. Lee, J. Chen, D. Pierrot, K. Sullivan, Y. Wang, X. Hu, et al. Decrease in the CO_2 uptake capacity in an ice-free Arctic Ocean basin. *Science*, 329(5991):556–559, 2010.

G. Castellani, C. Lüpkes, S. Hendricks, and R. Gerdes. Variability of Arctic sea-ice topography and its impact on the atmospheric surface drag. *Journal of Geophysical Research: Oceans*, 119(10):6743–6762, 2014.

J. C. Comiso. Large decadal decline of the Arctic multiyear ice cover. *Journal of Climate*, 25(4):1176–1193, 2012.

D. P. Dee, S. Uppala, A. Simmons, P. Berrisford, P. Poli, S. Kobayashi, U. Andrae, M. Balmaseda, G. Balsamo, P. Bauer, et al. The ERA-Interim reanalysis: Configuration and performance of the data assimilation system. *Quarterly Journal of the Royal Meteorological Society*, 137(656):553–597, 2011.

T. L. Delworth, A. J. Broccoli, A. Rosati, R. J. Stouffer, V. Balaji, J. A. Beesley, W. F. Cooke, K. W. Dixon, J. Dunne, K. Dunne, et al. GFDL's CM2 global coupled climate models. Part I: Formulation and simulation characteristics. *Journal of Climate*, 19(5):643–674, 2006.

R. E. Dickinson, G. A. Meehl, and W. M. Washington. Ice-albedo feedback in a CO2-doubling simulation. *Climatic Change*, 10(3):241–248, 1987.

E. E. Ebert and J. A. Curry. An intermediate one-dimensional thermodynamic sea ice model for investigating ice-atmosphere interactions. *Journal of Geophysical Research: Oceans*, 98(C6):10085–10109, 1993.

H. Eicken. Structure of under-ice melt ponds in the central Arctic and their effect on, the sea-ice cover. *Limnology and oceanography*, 39(3):682–693, 1994.

H. Eicken, H. Krouse, D. Kadko, and D. Perovich. Tracer studies of pathways and rates of meltwater transport through Arctic summer sea ice. *Journal of Geophysical Research: Oceans*, 107(C10):SHE–22, 2002.

H. Eicken, T. Grenfell, D. Perovich, J. Richter-Menge, and K. Frey. Hydraulic controls of summer Arctic pack ice albedo. *Journal of Geophysical Research: Oceans*, 109(C8), 2004.

D. Feltham, N. Untersteiner, J. Wettlaufer, and M. Worster. Sea ice is a mushy layer. *Geophysical Research Letters*, 33(14), 2006.

F. Fetterer and N. Untersteiner. Observations of melt ponds on Arctic sea ice. *Journal of Geophysical Research: Oceans*, 103(C11):24821–24835, 1998.

D. Flocco, D. L. Feltham, E. Bailey, and D. Schroeder. The refreezing of melt ponds on Arctic sea ice. *Journal of Geophysical Research: Oceans*, 120(2):647–659, 2015.

J. D. Ford, B. Smit, and J. Wandel. Vulnerability to climate change in the Arctic: a case study from Arctic Bay, Canada. *Global Environmental Change*, 16(2):145–160, 2006.

D. L. Gautier, K. J. Bird, R. R. Charpentier, A. Grantz, D. W. Houseknecht, T. R. Klett, T. E. Moore, J. K. Pitman, C. J. Schenk, J. H. Schuenemeyer, et al. Assessment of undiscovered oil and gas in the Arctic. *Science*, 324(5931):1175–1179, 2009.

K. A. Giles, S. W. Laxon, A. L. Ridout, D. J. Wingham, and S. Bacon. Western Arctic Ocean freshwater storage increased by wind-driven spin-up of the Beaufort Gyre. *Nature Geoscience*, 5(3):194–197, 2012.

J. Hanesiak, D. Barber, R. De Abreu, and J. Yackel. Local and regional albedo observations of Arctic first-year sea ice during melt ponding. *Journal of Geophysical Research: Oceans*, 106(C1):1005–1016, 2001.

J. Hansen, R. Ruedy, M. Sato, and K. Lo. Global surface temperature change. *Reviews of Geophysics*, 48(4), 2010.

A. M. Hanson. Studies of the mass budget of Arctic pack-ice floes. *Journal of Glaciology*, 5(41):701–709, 1965.

M. M. Holland, C. M. Bitz, and B. Tremblay. Future abrupt reductions in the summer Arctic sea ice. *Geophysical research letters*, 33(23), 2006.

V. Holten, C. Bertrand, M. Anisimov, and J. Sengers. Thermodynamics of supercooled water. *The Journal of chemical physics*, 136(9):094507, 2012.

E. C. Hunke, W. H. Lipscomb, and A. K. Turner. Sea-ice models for climate study: retrospective and new directions. *Journal of Glaciology*, 56(200):1162–1172, 2010a.

E. C. Hunke, W. H. Lipscomb, and A. K. Turner. Sea-ice models for climate study: retrospective and new directions. *Journal of Glaciology*, 56(200):1162–1172, 2010b.

E. C. Hunke, W. H. Lipscomb, A. K. Turner, N. Jeffery, and S. Elliott. CICE: the Los Alamos sea ice model documentation and software users manual Version 4.1 LA-CC-06-012. *T-3 Fluid Dynamics Group, Los Alamos National Laboratory*, 675, 2010c.

T. C. Johns, R. E. Carnell, J. F. Crossley, J. M. Gregory, J. F. Mitchell, C. A. Senior, S. F. Tett, and R. A. Wood. The second Hadley Centre coupled ocean-atmosphere GCM: model description, spinup and validation. *Climate dynamics*, 13(2):103–134, 1997.

E. Kalnay, M. Kanamitsu, R. Kistler, W. Collins, D. Deaven, L. Gandin, M. Iredell, S. Saha, G. White, J. Woollen, et al. The NCEP/NCAR 40-year reanalysis project. *Bulletin of the American meteorological Society*, 77(3):437–471, 1996.

L. H. Kantha and G. L. Mellor. A two-dimensional coupled ice-ocean model of the Bering Sea marginal ice zone. *Journal of Geophysical Research: Oceans*, 94(C8):10921–10935, 1989.

E. B. Kraus and J. S. Turner. A one-dimensional model of the seasonal thermocline II. The general theory and its consequences. *Tellus*, 19(1):98–106, 1967.

R. Kwok and D. Rothrock. Decline in Arctic sea ice thickness from submarine and ICESat records: 1958–2008. *Geophysical Research Letters*, 36(15), 2009.

S. W. Laxon, K. A. Giles, A. L. Ridout, D. J. Wingham, R. Willatt, R. Cullen, R. Kwok, A. Schweiger, J. Zhang, C. Haas, et al. CryoSat-2 estimates of Arctic sea ice thickness and volume. *Geophysical Research Letters*, 40(4):732–737, 2013.

S. Lee. A theory for polar amplification from a general circulation perspective. *Asia-Pac. J. Atmos. Sci*, 50:31–43, 2014.

W. K. Li, F. A. McLaughlin, C. Lovejoy, and E. C. Carmack. Smallest algae thrive as the Arctic Ocean freshens. *Science*, 326(5952):539–539, 2009.

M. Lüthje, D. Feltham, P. Taylor, and M. Worster. Modeling the summertime evolution of sea-ice melt ponds. *Journal of Geophysical Research: Oceans*, 111(C2), 2006.

S. Manabe and R. T. Wetherald. The effects of doubling the CO2 concentration on the climate of a general circulation model. *Journal of the Atmospheric Sciences*, 32(1):3–15, 1975.

S. Martin and P. Kauffman. The evolution of under-ice melt ponds, or double diffusion at the freezing point. *Journal of Fluid Mechanics*, 64(3):507–528, 1974.

T. Martin, M. Tsamados, D. Schroeder, and D. L. Feltham. The impact of variable sea ice roughness on changes in Arctic Ocean surface stress: A model study. *Journal of Geophysical Research: Oceans*, 121(3):1931–1952, 2016.

Mathworks. `http://uk.mathworks.com/help/matlab/ref/pdepe.html`. Online, accessed 27-September-2017.

G. A. Maykut and N. Untersteiner. Some results from a time-dependent thermodynamic model of sea ice. *Journal of Geophysical Research*, 76(6):1550–1575, 1971.

W. N. Meier, J. Stroeve, and F. Fetterer. Whither Arctic sea ice? A clear signal of decline regionally, seasonally and extending beyond the satellite record. *Annals of Glaciology*, 46(1):428–434, 2007.

N. Melia, K. Haines, and E. Hawkins. Sea ice decline and 21st century trans-Arctic shipping routes. *Geophysical Research Letters*, 43(18):9720–9728, 2016.

NASA. National Aeronautics and Space Administration Earth Observatory. `https://earthobservatory.nasa.gov/IOTD/view.php?id=51335`. Online, accessed 05-October-2017.

D. Notz and M. G. Worster. A one-dimensional enthalpy model of sea ice. *Annals of Glaciology*, 44:123–128, 2006.

D. Notz, M. G. McPhee, M. G. Worster, G. A. Maykut, K. H. Schlünzen, and H. Eicken. Impact of underwater-ice evolution on Arctic summer sea ice. *Journal of Geophysical Research: Oceans*, 108(C7), 2003.

NSIDC. National Snow and Ice Data Center. `https://nsidc.org/`. Online, accessed 25-September-2017.

C. Peralta-Ferriz and R. A. Woodgate. Seasonal and interannual variability of pan-Arctic surface mixed layer properties from 1979 to 2012 from hydrographic data, and the dominance of stratification for multiyear mixed layer depth shoaling. *Progress in Oceanography*, 134:19–53, 2015.

D. Perovich, T. Grenfell, B. Light, and P. Hobbs. Seasonal evolution of the albedo of multiyear Arctic sea ice. *Journal of Geophysical Research: Oceans*, 107(C10), 2002.

D. K. Perovich, E. Andreas, J. Curry, H. Eiken, C. Fairall, T. Grenfell, P. Guest, J. Intrieri, D. Kadko, R. Lindsay, et al. SHEBA: The surface heat budget of the Arctic Ocean. *EOS, Transactions, American Geophysical Union*, 80:481–486, 1999.

D. K. Perovich, T. C. Grenfell, J. A. Richter-Menge, B. Light, W. B. Tucker, and H. Eicken. Thin and thinner: Sea ice mass balance measurements during SHEBA. *Journal of Geophysical Research: Oceans*, 108(C3), 2003.

A. A. Petty, D. L. Feltham, and P. R. Holland. Impact of atmospheric forcing on Antarctic continental shelf water masses. *Journal of Physical Oceanography*, 43(5):920–940, 2013.

A. A. Petty, P. R. Holland, and D. L. Feltham. Sea ice and the ocean mixed layer over the Antarctic shelf seas. *The Cryosphere*, 8(2):761, 2014.

S. Pfirman, H. Eicken, D. Bauch, and W. Weeks. The potential transport of pollutants by Arctic sea ice. *Science of the Total Environment*, 159(2):129–146, 1995.

C. Polashenski, K. M. Golden, D. K. Perovich, E. Skyllingstad, A. Arnsten, C. Stwertka, and N. Wright. Percolation blockage: A process that enables melt pond formation on first year Arctic sea ice. *Journal of Geophysical Research: Oceans*, 122(1):413–440, 2017.

L. Rainville and R. A. Woodgate. Observations of internal wave generation in the seasonally ice-free Arctic. *Geophysical Research Letters*, 36(23), 2009.

D. A. Randall, R. A. Wood, S. Bony, R. Colman, T. Fichefet, J. Fyfe, V. Kattsov, A. Pitman, J. Shukla, J. Srinivasan, et al. Climate models and their evaluation. In *Climate change 2007: The physical science basis. Contribution of Working Group I to the Fourth Assessment Report of the IPCC (FAR)*, pages 589–662. Cambridge University Press, 2007.

R. Ricker, S. Hendricks, V. Helm, H. Skourup, and M. Davidson. Sensitivity of CryoSat-2 Arctic sea-ice freeboard and thickness on radar-waveform interpretation. *The Cryosphere*, 8(4):1607–1622, 2014.

A. Rösel, L. Kaleschke, and G. Birnbaum. Melt ponds on Arctic sea ice determined from MODIS satellite data using an artificial neural network. *The Cryosphere*, 6(2):431, 2012.

D. Rothrock, D. Percival, and M. Wensnahan. The decline in Arctic sea-ice thickness: Separating the spatial, annual, and interannual variability in a quarter century of submarine data. *Journal of Geophysical Research: Oceans*, 113(C5), 2008.

S. Rysgaard, J. Bendtsen, B. Delille, G. S. Dieckmann, R. N. Glud, H. Kennedy, J. Mortensen, S. Papadimitriou, D. N. Thomas, and J.-L. TISON. Sea ice contribution to the air–sea CO2 exchange in the Arctic and Southern Oceans. *Tellus B*, 63(5): 823–830, 2011.

C. L. Sabine, R. A. Feely, N. Gruber, R. M. Key, K. Lee, J. L. Bullister, R. Wanninkhof, C. Wong, D. W. Wallace, B. Tilbrook, et al. The oceanic sink for anthropogenic CO2. *science*, 305(5682):367–371, 2004.

R. W. Schmitt. Double diffusion in oceanography. *Annual Review of Fluid Mechanics*, 26 (1):255–285, 1994.

A. Schweiger, R. Lindsay, J. Zhang, M. Steele, H. Stern, and R. Kwok. Uncertainty in modeled Arctic sea ice volume. *Journal of Geophysical Research: Oceans*, 116(C8), 2011.

A. J. Semtner Jr. A model for the thermodynamic growth of sea ice in numerical investigations of climate. *Journal of Physical Oceanography*, 6(3):379–389, 1976.

M. C. Serreze, M. M. Holland, and J. Stroeve. Perspectives on the Arctic's shrinking sea-ice cover. *science*, 315(5818):1533–1536, 2007.

R. D. Skeel and M. Berzins. A method for the spatial discretization of parabolic equations in one space variable. *SIAM journal on scientific and statistical computing*, 11(1):1–32, 1990.

E. D. Skyllingstad, C. A. Paulson, and D. K. Perovich. Simulation of melt pond evolution on level ice. *Journal of Geophysical Research: Oceans*, 114(C12), 2009.

M. Steele and T. Boyd. Retreat of the cold halocline layer in the Arctic Ocean. *Journal of Geophysical Research: Oceans*, 103(C5):10419–10435, 1998.

M. Steele, J. H. Morison, and N. Untersteiner. The partition of air-ice-ocean momentum exchange as a function of ice concentration, floe size, and draft. *Journal of Geophysical Research: Oceans*, 94(C9):12739–12750, 1989.

M. E. Stern. The salt-fountain and thermohaline convection. *Tellus*, 12(2):172–175, 1960.

I. Stirling and C. L. Parkinson. Possible effects of climate warming on selected populations of polar bears (Ursus maritimus) in the Canadian Arctic. *Arctic*, pages 261–275, 2006.

J. C. Stroeve, M. C. Serreze, M. M. Holland, J. E. Kay, J. Malanik, and A. P. Barrett. The Arctics rapidly shrinking sea ice cover: a research synthesis. *Climatic Change*, 110(3): 1005–1027, 2012.

P. Taylor and D. Feltham. A model of melt pond evolution on sea ice. *Journal of Geophysical Research: Oceans*, 109(C12), 2004.

P. C. Taylor, M. Cai, A. Hu, J. Meehl, W. Washington, and G. J. Zhang. A decomposition of feedback contributions to polar warming amplification. *Journal of Climate*, 26(18): 7023–7043, 2013.

A. K. Turner and E. C. Hunke. Impacts of a mushy-layer thermodynamic approach in global sea-ice simulations using the CICE sea-ice model. *Journal of Geophysical Research: Oceans*, 120(2):1253–1275, 2015.

C. T. Tynan and D. P. DeMaster. Observations and predictions of Arctic climatic change: potential effects on marine mammals. *Arctic*, pages 308–322, 1997.

N. Untersteiner. On the mass and heat budget of Arctic sea ice. *Archiv für Meteorologie, Geophysik und Bioklimatologie, Serie A*, 12(2):151–182, 1961.

N. Untersteiner and F. I. Badgley. Preliminary results of thermal budget studies on Arctic pack ice during summer and autumn. *Arctic sea ice, Publ*, 598:85–92, 1958.

T. Uttal, J. A. Curry, M. G. McPhee, D. K. Perovich, R. E. Moritz, J. A. Maslanik, P. S. Guest, H. L. Stern, J. A. Moore, R. Turenne, et al. Surface heat budget of the Arctic Ocean. *Bulletin of the American Meteorological Society*, 83(2):255–276, 2002.

P. Wadhams. The underside of Arctic sea ice imaged by sidescan sonar. *Nature*, 333 (6169):161–164, 1988.

X. Wang, J. Key, R. Kwok, and J. Zhang. Comparison of Arctic sea ice thickness from satellites, aircraft, and PIOMAS data. *Remote Sensing*, 8(9):713, 2016.

J. Wettlaufer, M. G. Worster, and H. E. Huppert. The phase evolution of young sea ice. *Geophysical research letters*, 24(10):1251–1254, 1997.

M. G. Worster. Natural convection in a mushy layer. *Journal of fluid mechanics*, 224:335–359, 1991.

M. G. Worster. Convection in mushy layers. *Annual Review of Fluid Mechanics*, 29(1): 91–122, 1997.

J. Zhang and D. Rothrock. Modeling global sea ice with a thickness and enthalpy distribution model in generalized curvilinear coordinates. *Monthly Weather Review*, 131(5): 845–861, 2003.